

## 13. SITE 1220<sup>1</sup>

Shipboard Scientific Party<sup>2</sup>

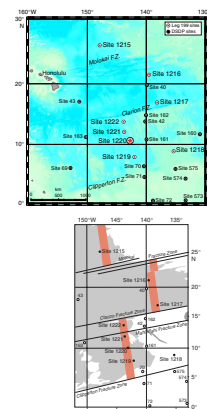
### BACKGROUND AND OBJECTIVES

Site 1220 (10°10.600'N, 142°45.503'W; 5218 meters below sea level (mbsl); Fig. F1) forms a southerly component of the 56-Ma transect drilled during Leg 199. It is situated about midway between the Clipper-ton and Clarion Fracture Zones in typical abyssal hill topography. On the basis of regional magnetic anomalies, we anticipated basement age at Site 1220 to be equivalent to Chron C25n (~56 Ma; Cande et al., 1989), slightly older than at Site 1219. At the outset of drilling at Site 1220, our estimate for total sediment depth was ~225 meters below sea-floor (mbsf) (Fig. F2).

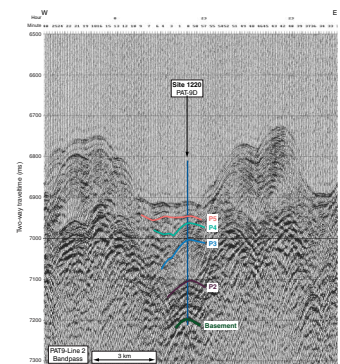
Based upon a fixed hotspot model (Gripp and Gordon, 1990, for 0- to 5-Ma Pacific hotspot rotation pole; Engebretson et al., 1985, for older poles), Site 1220 should have been located ~3° south of the equator at 56 Ma and in an equatorial position at 40 Ma. Thus, Site 1220 should have been situated underneath the South Equatorial Current in the early Eocene. A nearby piston core (EW9709-13PC) taken during the site survey cruise recovered >16 m of red clay, with the base of the core dated as middle–early Miocene on the basis of radiolarian biostratigraphy (Lyle, 2000).

Site 1220 will be used to study equatorial ocean circulation from the late Paleocene through the late Eocene during the early Cenozoic thermal maximum. Sediment records from this site will help to define the calcite compensation depth (CCD) and lysocline during the Paleocene–Eocene and Eocene–Oligocene transitions. In this and other respects, Site 1220 will act as an interesting analog to Site 1218. Both sites are thought to have been located on the equator at ~40 Ma, but the older crustal age anticipated at Site 1220 dictates a greater paleowater depth than for contemporaneous sediments accumulating at Site 1218.

F1. Site location map, p. 32.



F2. Seismic reflection profile, p. 33.



<sup>1</sup>Examples of how to reference the whole or part of this volume.  
<sup>2</sup>Shipboard Scientific Party addresses.

## SUMMARY

Site 1220 (10°10.601'N, 142°45.491'W) forms a southerly component of the 56-Ma transect to be drilled during Leg 199. It is situated halfway between the Clipperton and Clarion Fracture Zones at a water depth of 5218 mbsl in typical abyssal hill topography. On the basis of regional magnetic anomalies, we anticipated basement age at Site 1220 to be equivalent to Anomaly An25n (~56 Ma) (Cande et al., 1989), slightly older than at Site 1219.

Based upon a fixed hotspot model (Gripp and Gordon, 1990, for the 0- to 5-Ma Pacific hotspot rotation pole; Engebretson et al., 1985, for older poles) Site 1220 should have been located ~3°S of the equator at 56 Ma and in an equatorial position at 40 Ma. Thus, Site 1220 should have been situated beneath the South Equatorial Current in the early Eocene. Site 1220 data will be used as a deeper analog to Site 1218. Both sites are thought to have been located in an equatorial position at ~40 Ma, but Site 1220 was ~400 m deeper at this time.

Three holes were drilled at Site 1220. Hole 1220A was terminated when an advanced piston corer (APC) core jammed in the bottom-hole assembly (BHA) at ~100 mbsf, but basement was reached in Holes 1220B and 1220C at ~200 mbsf. Cores from Site 1220 overlap and form a continuous sedimentary sequence down to ~144 meters composite depth (mcd) (base of Core 199-1220B-10H). The sedimentary sequence recovered at the site is divided into five major sedimentary units. The uppermost unit (~0–19 mbsf) consists of very dark grayish brown clay with zeolites and is underlain by a lower Miocene–Oligocene Unit II (~19–40 mbsf) of radiolarian and nannofossil oozes with varying clay content. The underlying Oligocene radiolarian and nannofossil oozes of Unit III (~40–70 mbsf) are notable by the presence of a significant (~15%–45%) diatom component toward the base. Unit IV (~70–185 mbsf) consists of upper Eocene radiolarian oozes with clay and middle–lower Eocene chert with clayey radiolarian ooze. These sediments are underlain by a lower Eocene–upper Paleocene unit (~185–200 mbsf) of partially dolomitized nannofossil ooze, radiolarian nannofossil ooze, radiolarian ooze, calcareous chalk, and black clay atop an aphanitic to fine-grained phaneritic basalt.

Paleomagnetic data from Site 1220 gave excellent results and a reliable record of geomagnetic reversals from the early–middle Eocene to the early Miocene. The composite depth record from Holes 1220A, 1220B, and 1220C shows a remarkable match of the cores between the different holes. In fact, the virtual geomagnetic pole (VGP) latitude changes were used as a basis to help fit the cores to the mcd depth scale. Correlation of the magnetic stratigraphy at Site 1220 to the geomagnetic polarity timescale (GPTS) shows a record that spans from the top of Chron C21n to Subchron C6An.1n (~20.5–46.3 Ma).

Biostratigraphic results indicate that we recovered a nearly complete sequence of lower Miocene–lower Eocene radiolarian zones at Site 1220, interrupted only by a poorly recovered chert sequence from the uppermost lower Eocene and the lowermost middle Eocene. Calcareous fossils are generally poorly preserved or absent through much of the sequence. Calcareous nannofossils are sufficiently well preserved in the lowermost Miocene and Oligocene to provide a basic zonation. Planktonic foraminifers are almost entirely absent above the lower Eocene, but dissolution-resistant species allow the lower/upper Oligocene boundary to be approximated. Both planktonic foraminifers and calcar-

eous nannofossils provide a detailed zonation of a condensed sequence of lower Eocene nannofossil oozes and chert in the basal 10 m of Site 1220. The extinction of Paleocene benthic foraminifers, the appearance of the nannofossil genus *Rhomboaster*, the extinction of the nannofossil genus *Fasciculithus*, and the presence of “excursion fauna” of planktonic foraminifers provide a detailed biostratigraphy of the Paleocene/Eocene (P/E) boundary in Unit V. The nannofossil events occur 0.8–1.4 m above the extinction of Paleocene benthic foraminifers. The excursion fauna of planktonic foraminifers is present in sediments below the level of the benthic foraminifer extinction in sediments immediately overlying basalt. Thus, none of these events are precisely synchronous with the benthic foraminifer extinction, the marker we used for the P/E boundary, at this site.

Interstitial pore water profiles from Site 1220 are very similar to the profiles of all other Leg 199 sites except Site 1219 and primarily reflect minor organic matter degradation, the dissolution of biogenic silica, and minor alteration of underlying basalt. The bulk geochemistry of the sediments from Site 1220 reflects the shifts in lithology between sediments dominated by silica and carbonate.

Physical properties of the sediments also primarily reflect lithology. The carbonate sediments are higher in density, lower in porosity, and lower in magnetic susceptibility (MS) than the clay or radiolarian ooze lithologies. The radiolarian-rich sediments of Units II and IV are marked by high porosities, which average 88% and 85%, respectively. The radiolarian oozes maintain their porosity despite burial. The Eocene radiolarian oozes have the highest *P*-wave velocities of the unconsolidated sediment lithologies.

## **Highlights**

### **Magnetic Reversal Stratigraphy**

The clean record of magnetic reversal history from Site 1220 (for the entire APC-cored sediment section; 0–150 mbsf) spans the lower Miocene to the lower–middle Eocene (Subchron C6An.1n to the top of Chron C21; 20.05–46.3 Ma). This record is remarkable for a tropical site and will provide invaluable time control for calibration of radiolarian biostratigraphy. Because there are cyclic variations in radiolarian content of the Site 1220 Eocene section, presumably driven by orbital forcing of insolation, this record could be highly important for orbital tuning of the GPTS from the middle Eocene through the early Miocene.

### **Eocene/Oligocene Boundary**

A combination of magnetostratigraphy and nannofossil biostratigraphy indicates that we recovered a further Eocene/Oligocene (E/O) boundary at Site 1220 (~70 mbsf). Shore-based work on this section, together with those recovered at Sites 1217, 1218, and 1219, will allow us to improve existing constraints on the links between global cooling, Antarctic ice sheet growth, and a deepening CCD across this important paleoceanographic boundary.

### **P/E Boundary**

In Hole 1220B just above basement basalt, we recovered a lithologically striking interval of calcareous chalk and clay (199–200 mbsf).

Based on biostratigraphic data, this sequence represents the P/E boundary. Layers of calcareous chalk and clay display a large range in composition and color downcore. Alternating intervals of white and very pale brown calcareous chalk are present between 198.9 and 199.4 mbsf and contain a minor amount (5%–10%) of poorly preserved nannofossils. White layers are present between 199.15 and 199.23 mbsf and contain 15%–30% planktonic foraminifers. The sediments below this interval consist of faintly banded dark yellowish brown calcareous chalk but are barren of microfossils. Dolomite (up to 10%) and clay (10%–35%) are also present in this lithology. Below 199.50 mbsf is a 4-cm-thick layer of very dark brown (7.5YR 2.5/3) calcareous chalk underlain by a black clay. Major components of both sediments are dolomite, iron manganese oxides, and clay. Volcanic glass is present as a minor component. Dolomite content decreases over the interval from 199.52 to 199.54 mbsf, and no calcareous or siliceous fossils were observed in corresponding smear slides. Directly beneath the black clay is a 4.5-cm-thick interval of yellowish red calcareous chalk. In this interval is a 1-cm-thick brownish yellow layer of calcareous chalk. Sediments in the yellowish red layers are weakly laminated and contain clay, dolomite, calcite, and a minor percentage of nannofossils. Iron manganese oxides and opaque minerals are minor components. The brownish yellow chalk layer contains clay, dolomite, iron manganese oxides, volcanic glass, and abundant small mottles. Nannofossils are rare in these layers.

The base of the sedimentary section contains a 9-cm-thick interval of brownish yellow clayey calcareous chalk (199.59–199.68 mbsf) with thin black laminations. Dolomite comprises up to 10% of these sediments. Zeolites and nannofossils are also present as minor components. Iron manganese oxides are rare. Laminations contain clay, iron manganese oxides, dolomite, zeolites, and small amounts of volcanic ash and are barren of calcareous fossils.

## **OPERATIONS**

### **Transit to Site 1220 (PAT-9D)**

The 149-nmi voyage to proposed Site PAT-9D was accomplished in 13.3 hr at an average speed of 11.2 kt. At 1800 hr on 28 November, 2001, the vessel slowed to 5 kt, and a short 3.5-kHz survey was made from east to west across the site. Upon conclusion of the 1-hr survey, the vessel came about and returned to site as the thrusters were lowered and the dynamic positioning system (DPS) was activated. The Global Positioning System receiver interface to the DPS was employed to situate the vessel over the coordinates of the new location by 1915 hr. A beacon was deployed at 2006 hr. The corrected precision depth recorder (PDR) depth was 5234.4 meters below rig floor (mbrf).

### **Hole 1220A**

After the drill string was deployed to a depth of 5215 mbrf, the driller lowered the bit until the heave compensator appeared to activate, suggesting contact with a firm seafloor. The contact was at a bit depth of ~5233 mbrf. Hole 1220A was spudded with the APC at 0500 hr on 29 November with the bit at 5229.0 mbrf. The seafloor depth that was indicated by the recovery of the initial core was 5229.1 mbrf. This depth was 5.3 m shallower than the PDR depth. Piston coring advanced rou-

tinely to 95.0 mbsf (Cores 1H through 10H) with excellent recovery (Table T1). Cores were oriented starting with Core 3H.

During the process of obtaining Core 11H, the overshot shear pin parted and the Tensor tool was recovered without the core barrel. The Tensor tool was set aside, and a second wireline trip with the sinker bars was made to retrieve the core barrel. Upon retrieval, the core barrel was momentarily stuck but quickly came free and was recovered. Core 12H was taken in the customary manner with a full bleed-off of pressure, indicating a full stroke. The sinker bars and Tensor tool were retrieved by the wireline but without the core barrel. The Tensor tool was laid down, and the wireline jars were deployed to recover the core barrel. The core barrel could not be released by alternately applying overpull and upward impacts with the wireline jars. The effort was given up after 45 min, the overshot shear pin was intentionally parted, and the wireline was recovered. The drill string was then retrieved, and the hole was terminated.

APC operations in Hole 1220A resulted in 114.0 m cored with 118.7 m recovered (average recovery 104.1%).

### **Hole 1220B**

After the BHA was redeployed, the vessel was offset 20 m west of Hole 1220A in preparation for the spudding of Hole 1220B. The drill string was deployed to a depth of 5215.5 mbrf, and Hole 1220B was spudded at 2215 hr on 30 November. After the bit was drilled to 34.0 mbsf, APC operations were initiated and the hole was deepened to 152.0 mbsf. The interval from 62.5 to 64.5 mbsf was drilled to maintain an appropriate stratigraphic overlap with Hole 1220A. The cored interval was 116.0 m with 126.8 m recovered (109.3% recovery). All piston cores were oriented. The Adara temperature tool was deployed at 53.0 mbsf (Core 2H), 83.5 mbsf (5H), and 102.5 mbsf (7H). The developmental methane tool was deployed and appeared to have successfully obtained data.

Hole 1220B was deepened from 152.0 to 202.0 mbsf with extended core barrel (XCB) coring (Table T1) and penetrated basaltic basement with the last core (Core 20X). XCB operations deepened the hole 50.0 m and recovered 17.8 m of sediment (35.6% recovery). The total recovery for the hole was 144.7 m, representing 87.1% of the cored interval.

Hole 1220B was terminated when the bit cleared the seafloor at 1530 hr on 2 December. The vessel was then offset 20 m west of Hole 1220B.

### **Hole 1220C**

Hole 1220C was spudded at 1600 hr on 2 December. After the bit was drilled to 25.0 mbsf, one piston core was obtained spanning the Oligocene/Miocene (O/M) boundary (25.0–34.5 mbsf). The hole was then drilled from 34.5 to 60.0 mbsf, where continuous piston coring was initiated, and the hole was advanced to 145.5 mbsf. The APC-cored interval was 95.0 m with 98.0 m recovered (103.2% recovery) (Table T1). All APC cores were oriented. Hole 1220C was deepened from 145.5 to 204.1 mbsf with XCB coring operations. Basaltic basement was reached with the last core (Core 17X). The XCB-cored interval was 58.6 m with 18.13 m recovered (30.9%). The total recovery for the hole was 153.6 m, representing 75.6% of the cored interval (Table T1).

Following the end of coring operations in Hole 1220C, the drill string was pulled to the deck, the beacon was retrieved, and the drilling

equipment, hydrophones, and thrusters were secured. The vessel departed location at 0930 hr on 4 December.

## LITHOSTRATIGRAPHY

Drilling at Site 1220 recovered a 200.3-m section of pelagic sediments overlying seafloor basalt. The upper 25 m is lower Miocene clay and radiolarian ooze, underlain by 45.6 m of Oligocene nannofossil and radiolarian ooze and 129 m of Eocene radiolarian ooze with alternations of nannofossil ooze, clay, and chert. A 25-cm-thick upper Paleocene chalk section was recovered above basement.

The sedimentary sequence at Site 1220 has been divided into six major lithologic units and subunits (Fig. F3). Lithologic descriptions for 0 to 114.0 mbsf are primarily based on sediments from Hole 1220A. Below 114.0 mbsf, descriptions are based on the sequence recovered in Holes 1220B and 1220C.

### Unit I

Interval: 199-1220A-1H-1, 0 cm, through 3H-1, 11 cm  
Depth: 0.0–19.1 mbsf (Hole 1220A)  
Age: early Miocene  
Lithology: clay and clay with zeolites

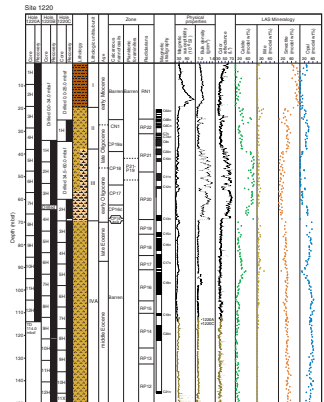
Unit I consists of very dark grayish brown (10YR 4/2) clay with zeolites grading to a dark brown (10YR 3/3) clay. Zeolites are a significant component (10%–15%) in the upper 14.9 m (Sections 199-1220A-2H-1 through 2H-4, 93 cm). Mottles are common in the uppermost 9.5 m of Unit I and rare between 9.5 and 19.4 mbsf (Sections 199-1220A-1H-CC through 2H-CC). Iron oxides and manganese nodules are present in minor to trace amounts below 18.2 mbsf (Section 199-1220A-2H-6, 130 cm).

### Unit II

Intervals: 199-1220A-3H-1, 11 cm, through 4H-6, 110 cm; 199-1220B-1H-1, 0 cm, through 1H-4, 55 cm; and 199-1220C-1H-1, 0 cm, through 1H-CC, 26 cm  
Depths: 19.1–37.2 mbsf (Hole 1220A); 34.0–39.0 mbsf (Hole 1220B); and 25.0–34.5 mbsf (Hole 1220C)  
Age: early Miocene to Oligocene  
Lithology: radiolarian ooze with clay, nannofossil radiolarian ooze with clay, and nannofossil ooze with clay and radiolarians

The dominant lithology in Unit II is very dark brown (7.5YR 2.5/3) to dark yellowish brown (10YR 3/4) radiolarian ooze. Thin alternations of yellowish brown (10YR 6/4) nannofossil radiolarian ooze are present between 24 and 27 mbsf (interval 199-1220A-3H-4, 55 cm, through 3H-6, 85 cm). Contacts between the lithologies are gradational and mottled. Brownish yellow (10YR 6/6) mottles are common to abundant in both lithologies.

F3. Lithologic summary, p. 34.



### **Unit III**

Intervals: 199-1220A-4H-6, 110 cm, through 8H-2, 115 cm; 199-1220B-1H-4, 55 cm, to 4H-6, 81 cm; and 199-1220C-2H-1 through 3H-2, 16 cm

Depths: 37.2–69.2 mbsf (Hole 1220A); 39.0–71.4 mbsf (Hole 1220B); and 60.0–71.2 mbsf (Hole 1220C)

Age: Oligocene

Lithology: nannofossil ooze, radiolarian ooze with clay and radiolarians, and nannofossil diatom ooze

Unit III consists of pale brown (10YR 8/3) to yellowish brown (10YR 5/4) nannofossil ooze. Between 37.2 and 56.9 mbsf (interval 199-1220A-4H-6, 123 cm, through 6H-7, 40 cm), the nannofossil ooze alternates with decimeter-scale intervals of dark brown (10YR 3/3) radiolarian ooze and light yellowish brown (10YR 6/4) nannofossil diatom ooze. The thickness of the nannofossil ooze layers increases downcore, and color grades to very pale brown (10YR 8/2). Contacts between lithologies are gradational and are obscured by bioturbation.

Clay content (based on smear slide descriptions) ranges from <5% in nannofossil ooze to 15%–20% in radiolarian ooze. Diatoms are absent in the upper portion of Unit III but increase from 15% to 45% downcore in the lowermost 6 m of the unit.

### **Unit IV**

Intervals: 199-1220A- 8H-2, 115 cm, through 12H-CC; 199-1220B-4H-6, 81 cm, through 17X-CC; and 199-1220C-3H-2, 16 cm, through 14X-CC

Depths: 69.2–114.0 mbsf base of hole (Hole 1220A); 71.4–187.9 mbsf (Hole 1220B); and 71.2–183.5 mbsf (Hole 1220C)

Age: late to early Eocene

Lithology: radiolarian ooze with clay, clayey radiolarian ooze, clay with radiolarians, and chert

Unit IV is divided into two subunits, based on the presence or absence of chert. Subunit IVA consists of radiolarian ooze with varying clay content, and Subunit IVB is composed of chert and clayey radiolarian ooze.

#### **Subunit IVA**

Intervals: 199-1220A-8H-2, 115 cm, through 12H-CC; 199-1220B-4H-6, 81 cm, through 13X-CC; and 199-1220C-3H-2, 16 cm, through 11X-CC

Depths: 69.2–114.0 mbsf base of hole (Hole 1220A); 71.4–159.2 mbsf (Hole 1220B); and 71.2–155.1 mbsf (Hole 1220C)

Age: late to middle Eocene

Lithology: radiolarian ooze with clay, clayey radiolarian ooze, and clay with radiolarians

The dominant lithology in Subunit IVA is radiolarian ooze with clay. Color ranges from dark yellowish brown (10YR 3/4) to dark brown (10YR 3/3). Yellow (10YR 7/6) and pale brown (10YR 6/3) mottles are common. Diatom abundance is generally very low but occasionally increases to 35% in minor lithologies from smear slide estimates.

An interval of clay with radiolarians is present near the base of Subunit IVA (Hole 1220B: 144.2–152.0 mbsf). The thickness of this clay is probably exaggerated in Hole 1220B by sediment flow-in associated with coring a 5-cm-thick claystone interval (intervals 199-1220B-13H-1, 75–80 cm, and 199-1220C-11X-2, 89–94 cm).

**Subunit IVB**

Intervals: 199-1220B-14X-1, 0 cm, through 17X-CC; and Section 199-1220C-12X, 0 cm, through 14X-CC  
 Depths: 159.2–187.9 mbsf (Hole 1220B) and 155.1–183.5 mbsf (Hole 1220C)  
 Age: middle to early Eocene  
 Lithology: chert and clayey radiolarian ooze

Subunit IVB consists of chert and clayey radiolarian ooze. The chert and surrounding sediment were poorly recovered. Chert occurs as black (N1) fragments broken by the drilling process. Clayey radiolarian ooze ranges from strong brown (7.5YR 4/6) to yellowish brown (10YR 5/6). Decimeter-scale alternations of clay and radiolarian ooze with iron oxides are present between 173.9 and 183.5 mbsf (Sections 199-1220B-16X-4, 25 cm, through 16X-CC and 199-1220C-14X-1, 0 cm, through 14X-CC). Yellowish brown (10YR 5/4) mottles are common throughout this subunit. A layer of volcanic ash is present near 171.5 mbsf (interval 199-1220B-16X-2, 88–92 cm).

**Unit V**

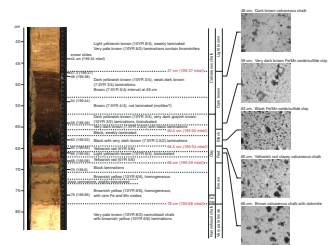
Intervals: 199-1220B-18X-1, 0 cm, through 20X-CC, 12 cm; and 199-1220C-16X-1, 0 cm, through 16X-CC  
 Depths: 187.9–200.0 mbsf (Hole 1220B) and 193.0–197.4 mbsf (Hole 1220C)  
 Age: early Eocene to late Paleocene  
 Lithology: nannofossil ooze, radiolarian nannofossil ooze, radiolarian ooze, calcareous chalk, and clay

Unit V primarily consists of light yellowish brown (10YR 6/4) to very pale brown (10YR 7/4) nannofossil ooze and radiolarian nannofossil ooze. Dark yellowish brown (10YR 4/6, 10YR 3/6) radiolarian ooze is present between 190.42 and 190.8 mbsf (interval 199-1220B-18X-3, 20–58 cm). Very pale brown (10YR 7/2) mottles are common. Authigenic dolomite crystals constitute a significant proportion of the nannofossil ooze (10%–35%).

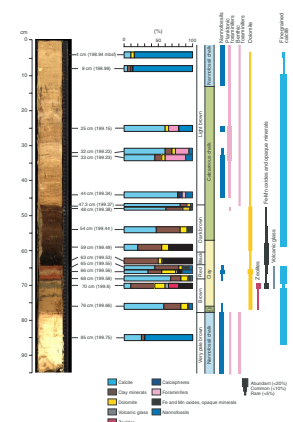
**P/E Sediments**

Between 198.9 and 199.7 mbsf (interval 199-1220B-20X-2, 4–85 cm), there is an interval of calcareous chalk and clay. Based on biostratigraphic data (see “**Biostratigraphy**,” p. 10), this sequence represents the P/E boundary. The P/E boundary was only recovered in Hole 1220B. Layers of calcareous chalk and clay display a large range in composition and color downcore (Figs. F4, F5). Alternating intervals of white and very pale brown (10YR 8/3) calcareous chalk are present between 198.9 and 199.4 mbsf (interval 199-1220B-20X-2, 10–48 cm) and contain a minor amount (5%–10%) of poorly preserved nannofossils. White layers are present between 199.15 and 199.23 mbsf (interval 199-1220B-

**F4.** Lithologic and color changes across the P/E boundary sequence, p. 36.



**F5.** Compositional changes across the P/E boundary sequence, p. 37.



20X-2, 25–33 cm) and contain 15%–30% planktonic foraminifers. The sediments below this interval consist of faintly banded, dark yellowish brown (10YR 3/4) calcareous chalk but are barren of microfossils (interval 199-1220B-20X-2, 48–60 cm). Dolomite (up to 10%) and clay (10%–35%) also are present in this lithology.

Below 199.50 mbsf (Section 199-1220B-20X-2, 60 cm), is a 4-cm-thick layer of very dark brown (7.5YR 2.5/3) calcareous chalk underlain by a black (10YR 2/1) clay. Major components of both sediments are dolomite, iron manganese oxides, clay, and possibly sulfides. Volcanic ash is present as a minor component. Dolomite content decreases from 199.52 to 199.54 mbsf, and no calcareous or siliceous fossils were observed in smear slides.

Directly beneath the black clay, there is a 4.5-cm-thick interval of yellowish red (5YR 5/6) calcareous chalk (interval 199-1220B-20X-2, 64–69 cm; 199.54–199.59 mbsf). Within this interval is a 1-cm-thick brownish yellow (10YR 6/6) layer of calcareous chalk. Sediments within the yellowish red layers are weakly laminated and contain clay, dolomite, calcite, and a minor percentage of nannofossils. Iron manganese oxides and opaque minerals are minor components. The brownish yellow chalk layer contains clay, dolomite, iron manganese oxides, volcanic glass, and abundant small mottles. Nannofossils are rare in these layers.

The base of the sedimentary section contains a 9-cm-thick interval of brownish yellow (10YR 6/6) clayey calcareous chalk (interval 199-1220B-20X-2, 69–78 cm; 199.59–199.68 mbsf) with thin black (10YR 2/1) laminations. Dolomite comprises up to 10% of the sediment. Zeolites and nannofossils also are present as minor components. Iron manganese oxides are rare. Laminations contain clay, iron manganese oxides, dolomite, zeolites, and small amounts of volcanic ash and are barren of calcareous fossils.

## **Unit VI**

Intervals: 199-1220B-20X-CC, 14–18 cm, and 199-1220C-17X-1, 0–69 cm

Depths: 202.0 mbsf (Hole 1220B) and 197.4–204.1 mbsf (Hole 1220C)

Age: late Paleocene

Lithology: basalt

Basaltic fragments containing aphanitic to fine-grained phaneritic texture were recovered at the base of Holes 1220B and 1220C. Thin glassy rinds are present on some of the pieces. Exterior surfaces are moderately altered from weathering processes. Interior surfaces show common oxidation of some of the minerals. Numerous calcite veins ranging from 1 to 5 mm in thickness are found in several of the pieces from Hole 1220C.

## **Discussion/Summary**

At Site 1220, Paleocene seafloor basalt is overlain by 200.3 m of pelagic sediments that are divided into five lithologic units. Although sediments here are dominated by siliceous ooze, the sequence can be correlated roughly with the more calcareous Units I–V at Sites 1218 and 1219.

The Paleocene–lower Eocene sequence is carbonate rich. The P/E boundary section (Hole 1220B: 199.37–199.68 mbsf) consists of calcareous chalk and black clay and differs in lithology and color from the dark brown nannofossil clay of similar age at Site 1215.

The Eocene section in Hole 1220C is 129 m thick and contains brown to dark brown radiolarian ooze with varying amounts of clay and nannofossils. The E/O boundary is marked by a transition from dark brown radiolarian ooze below to pale brown nannofossil ooze above. This contact is not sharp, probably because of mixing by bioturbation. A transition from siliceous sedimentation during the Eocene to carbonate deposition during the Oligocene is also observed in sediments from several other sites in the region (e.g., Sites 1218 and 1219, and Deep Sea Drilling Project Sites 161 and 162) and probably reflects a deepening of the CCD (van Andel et al., 1975).

Lower Oligocene sediments consist mainly of pale brown nannofossil ooze. The upper Oligocene section contains alternations of dark yellowish brown radiolarian ooze, and the O/M boundary is represented in Core 199-1220A-3H. Sediments from the lower Miocene are dominated by dark brown radiolarian ooze and show a relatively sharp transition to clay and clay with zeolites in the lower Miocene just above the O/M boundary. Sediments younger than the early Miocene were not recovered at this site.

## **BIOSTRATIGRAPHY**

At Site 1220, we recovered a 202-m-thick sequence of lower Miocene–uppermost Paleocene radiolarian oozes, chert, and nannofossil ooze. A nearly complete sequence of lower Miocene–lower Eocene radiolarian zones was identified and was interrupted only by a poorly recovered chert sequence in the uppermost lower Eocene and the lowermost middle Eocene. Calcareous fossils are generally poorly preserved or absent through much of the sequence. Calcareous nannofossils are sufficiently well preserved in the lowermost Miocene and Oligocene to provide a basic zonation. Planktonic foraminifers are almost entirely absent above the lower Eocene, but dissolution-resistant species allow the upper/lower Oligocene boundary to be approximated. Both planktonic foraminifers and calcareous nannofossils provide a detailed zonation of a condensed sequence of lower Eocene nannofossil oozes and chert in the basal 10 m of Site 1220. The extinction of Paleocene benthic foraminifers, the appearance of the nannofossil genus *Rhomboaster*, the extinction of the nannofossil genus *Fasciculithus*, and the presence of excursion fauna of planktonic foraminifers provide a detailed biostratigraphy of the P/E boundary in Core 199-1220B-20X. The nannofossil events occur 0.8–1.4 m above the extinction of Paleocene benthic foraminifers. The excursion fauna of planktonic foraminifers is present in sediments below the level of the benthic foraminifer extinction and immediately overlying basalt. Thus, none of these events are precisely synchronous with the benthic foraminifer extinction at this site.

### **Calcareous Nannofossils**

Samples from Holes 1220A and 1220B were analyzed for the biostratigraphic subdivision of the sedimentary succession. Depth posi-

tions and age estimates of biostratigraphic marker events are shown in Table T2.

Cores 199-1220A-1H and 2H are barren of calcareous nannofossils (Fig. F6). Poorly preserved lowermost Miocene nannofossils are observed in samples from Core 199-1220A-3H, in which assemblages are made up by solution-resistant taxa such as discoasters (*Discoaster calculosus* and *Discoaster deflandrei* gr.), abundant specimens of *Triquetrorhabdulus* spp. (*Triquetrorhabdulus carinatus* and *Triquetrorhabdulus milowii*), and *Sphenolithus moriformis*. Placoliths are mostly dissolved. Assemblages with similar preservation features are present also in Core 199-1220A-4H. In Sample 199-1220A-4H-CC, abundant *Ciclycargolithus abisectus* was recorded. The first downhole occurrence of a moderately preserved nannofossil assemblage is observed in Core 199-1220A-5H, which contains Oligocene nannofossils. The base of *Sphenolithus ciperensis* was recorded in Sample 199-1220A-5H-1, 60 cm, defining the boundary between Subzone CP19a and Zone CP18 (NP24/NP23). The interval corresponding to Zone CP18 (upper part of NP23) is characterized by a diversified assemblage of small Oligocene sphenoliths including *Sphenolithus distentus*, *Sphenolithus predistentus*, *Sphenolithus tribulosus*, and *Sphenolithus celsus*. In the lower part of Core 199-1220A-5H, the upper range of *Sphenolithus pseudoradians* is recorded, and its disappearance was located in Sample 199-1220A-5H-5, 45 cm. The boundary between Zones CP18 and CP17 is placed between Samples 199-1220A-6H-3, 100 cm, and 6H-4, 80 cm (in Hole 1220B between Samples 199-1220B-3H-1, 60 cm, and 3H-1, 90 cm) and corresponds to the appearance of *S. distentus*, which occurs just above an interval with abundant *S. moriformis*. In the interval from Core 199-1220A-7H to the upper part of Core 8H (Core 4H in Hole 1220B), nannofossil assemblages show variable states of preservation from moderate to poor, representing Subzones CP16c (NP22) and CP16a+b (NP21).

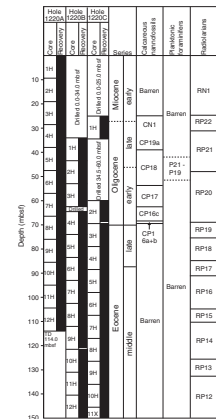
A barren interval begins within Subzone CP16a+b (NP21) in the lowermost Oligocene between Samples 199-1220A-8H-2, 126 cm, and 8H-2, 135 cm. The next downhole occurrence of nannofossils is observed in Sample 199-1220B-18X-1, 20 cm, containing a lower Eocene CP9b/NP11 assemblage, including abundant *Tribrachiatus orthostylus*, common *Discoaster diastypus*, and few to rare *Discoaster falcatus* and *Discoaster multiradiatus*.

The base of Subzone CP9a (NP10) falls in the gap between Cores 199-1220B-19X and 20X (Fig. F6). Sample 199-1220B-20X-1, 5 cm, represents chalk scraped from a piece of chert, containing a poorly preserved lowermost Eocene assemblage belonging to Subzone CP8b (upper NP9), although similar in composition to the next lower sample (Sample 199-1220B-20X-1, 20 cm) taken from the chalk sequence lying immediately below the chert layer. The uppermost chalk in Core 199-1220B-20X contains *Chiasmolithus bidens*, *Chiasmolithus consuetus*, *D. multiradiatus*, *Ellipsolithus distichus*, *Toweius ?crassus*, *Toweius eminens*, *Toweius pertusus*, and *Rhomboaster* spp.

The genus *Fasciculithus* shows a distinct extinction occurring over a 25-cm interval between Samples 199-220B-20X-1, 90 cm, and 20X-1, 115 cm. The genus *Rhomboaster*, which is normally poorly preserved because of calcite recrystallization, shows a similarly distinct first occurrence over a 26-cm interval between Samples 199-1220B-20X-1, 125 cm, and 20X-2, 1 cm. The crossover in abundance between these two genera appears to be an event that is easier to recognize than the first or last occurrence of members of these genera, respectively, and occurs between Samples 199-1220B-20X-1, 105 cm, and 20X-1, 115 cm. The fas-

T2. Distribution of calcareous nannofossil datums, p. 70.

F6. Biostratigraphic zonation, p. 38.



iculiths are abundant (10–15 specimens per field of view at 1000× magnification) just below their extinction level and includes species such as *Fasciculithus alanii*, *Fasciculithus bobii*, *Fasciculithus involutus*, *Fasciculithus richardii*, *Fasciculithus schaubii*, and *Fasciculithus tympaniformis*. In contrast to the diversity among the fasciculiths, rhomboasters are characterized by a low diversity in the lower part of their range, probably only consisting of a single species, *Rhomboaster cuspis*. Subsequently, specimens with extended corners (long armed) appear. The evolution and problematic taxonomic status of the *Rhomboaster/Tribrachiatus* lineage was discussed at length by Romein (1979) and more recently by Bybell and Self-Trail (1995, 1997) and Aubry (1996).

The *Rhomboaster/Fasciculithus* first/last occurrence events occur 0.77–1.38 m above the base of a multicolored interval in Section 199-1220B-20X-2 (see “Unit V,” p. 8, in “Lithostratigraphy”). The base of this interval holds the P/E boundary Benthic Extinction Event (BEE). The *Rhomboaster/Fasciculithus* events are present above the P/E boundary but exactly when they occurred in the earliest Eocene remains uncertain.

Calcareous nannofossils were studied in each color band above the BEE (in interval 199-1220B-20X-2, 0–78.5 cm). Sample levels and total abundance are listed below: all centimeter levels refer to depth in Section 199-1220B-20X-2. For a detailed description of color and lithology, see “Unit V,” p. 8, in “Lithostratigraphy.”

- 1 cm = light yellow-brown calcareous silt: abundant nannofossils, with a marked improvement in preservation compared to the underlying sediments. The taxonomic composition is similar to the 85-cm level, including complete specimens of *Thoracosphaera* spp. This group of calcareous dinoflagellates flourished for a short time interval in low and middle latitudes immediately following the demise of oceanic micro- and nanoplankton at the Cretaceous/Tertiary boundary (e.g., Romein, 1977; Thierstein and Okada, 1979; Perch-Nielsen, 1981; Monechi, 1985). The abundance of *Thoracosphaera* spp., in a short interval immediately overlying the P/E boundary sediments from Hole 1220B, probably reflects a change of critical boundary condition(s) in surface waters, allowing this opportunistic group to rapidly expand and thrive for a brief period of time.
- 46 cm = light yellow-brown calcareous silt: few nannofossils and poor preservation. The taxonomic composition is similar to the 85-cm level.
- 55 cm = brown clay: barren of calcareous nannofossils.
- 62 cm = black manganese-rich layer: rare nannofossils and poor preservation. The taxonomic composition is similar to the 85-cm level and includes *Heliolithus ?floris*.
- 65 cm = yellowish red (upper “pink” layer): barren of calcareous nannofossils.
- 66.5 cm = light yellowish brown clay between the upper and lower “pink” layers: barren of calcareous nannofossils.
- 68 cm = light yellowish red (lower “pink” layer): rare but diverse nannofossil assemblage, the taxonomic composition is similar to the 85-cm level, plus *Zygodiscus* spp.

75 cm = brownish yellow structureless clay: barren of calcareous nannofossils.

85 cm = very pale brown nannofossil chalk, abundant nannofossils showing poor preservation: *C. bidens*, *Coccolithus pelagicus*, *Discoaster mohleri*, *D. multiradiatus*, *Discoaster nobilis*, *F. involutus*, *F. richardii*, *F. schaubii*, *F. tympaniformis*, *Prinsius bisulcus*, *Sphenolithus primus*, *Thoracosphaera* spp., *T. eminens*, *T. pertusus*, and abundant fragments of shield rims including those from *Campylosphaera* and *Ericsonia*. Sample 199-1220B-20X-CC holds a virtually identical assemblage. The entire Core 199-1220B-20X belongs to Zone CP8 (NP9).

### Planktonic Foraminifers

The Eocene–Oligocene radiolarian-rich sediments, which comprise much of the sequence recovered at Site 1220, are largely barren of planktonic foraminifers. However, diverse and moderately well-preserved assemblages of planktonic foraminifers are present in the condensed (~10 m) P/E boundary carbonate sequence overlying basement in Hole 1220B. These assemblages include the distinctive P/E “excursion taxa,” which can be used to approximate the P/E boundary (Kelly et al., 1996, 1998). The presence of upper Paleocene–lower Eocene species is recorded in Table T3.

The red clay and radiolarian ooze of Cores 199-1220A-1H through 4H (Units I and II) is barren of planktonic foraminifers, apart from the occasional appearance of thick-walled dissolution-resistant forms. Cores 199-1220A-5H and 6H, which also have a nannofossil ooze component, contain rare and poorly preserved specimens of *Subbotina euapertura* and *Subbotina utilisindex*, in addition to *Paragloborotalia opima opima* and *Paragloborotalia opima nana*. *P. opima opima* is present in Samples 199-1220A-5H-3, 60–65 cm, to 6H-4, 40–44 cm, and indicates the presence of Oligocene strata between 30.6 and 27.1 Ma (upper Zone P19 to P21). Cores 199-1220A-7H through 12H are barren of planktonic foraminifers. Core 199-1220B-9H is approximately depth-correlative with Core 199-1220A-12H. The interval between Cores 199-1220B-9H through 17X is composed mainly of radiolarian ooze and is barren of planktonic foraminifers. Visual observations of Cores 199-1220B-9H to 17H indicated an absence of carbonate sediment; therefore, we confined our sampling to core catchers in this interval.

The carbonate content increases dramatically in lithostratigraphic Unit III, and planktonic foraminifers are present from Core 199-1220B-18X to the base of the hole. Preservation is poor near the top of the chalk but improves downhole. Core 18X contains rare and poorly preserved specimens of *Acarinina coalingensis* and *Acarinina soldadoensis*, which broadly indicate a late Paleocene–early Eocene age. Sample 199-1220B-19X-1, 77–79 cm, contains *Morozovella marginodentata*, *Morozovella aequa*, *Acarinina quetra*, *Subbotina triangularis*, and *Globanomalina psuedoimitata* as well as *A. coalingensis* and *A. soldadoensis*. Sample 199-1220B-19X-CC shows slightly better preservation and, in addition to the species listed above, contains *Morozovella subbotinae*, *Subbotina patagonica*, *Acarinina berggreni*, and *Igorina lodoensis*. We assign these samples to Zone P6 based on the absence of the Zone P5 marker, *Morozovella velascoensis*, and the Zone P7 marker, *Morozovella aragonensis*.

The last occurrence of *Morozovella acuta* occurs between Samples 199-1220B-20X-1, 59–66 cm, and 20X-2, 0–4 cm (198.90–198.45 mbsf; 216.70–217.61 mcd), and is used to approximate the P5/P6 zonal

---

T3. Distribution of late Paleocene–early Eocene planktonic foraminifers, p. 71.

---

boundary. The numerical age estimate for this datum is listed as 54.7 Ma by Berggren et al. (1995). However, Berggren et al. (1995) also say that this event occurs “midway between the -17 (54.4 Ma) and +19 (54.0 Ma) ash beds in Hole 550” (see table 8 in Berggren et al., 1995), which implies that the disappearance of *M. acuta* occurs at 54.2 Ma.

A set of small-volume (~0.5–1.0 cm<sup>3</sup>) samples was examined from the P/E boundary interval in order to document the presence of planktonic foraminifers without resorting to destructive sampling. These samples were derived from surface scrapings through Sections 199-1220B-20X-1 and 20X-2, and each spans an interval of 7.5 cm. Samples from Section 199-1220B-20X-1 contain mainly undifferentiated and poorly preserved planktonic foraminiferal assemblages, including the species *M. subbotinae*, *A. coalingensis*, *A. soldadoensis*, *Acarinina nitida*, *S. patagonica*, and occasional *Morozovella apantesma*. We assign these samples to Zones P5 and P6.

The P/E boundary is approximated in Core 199-1220B-20X by the presence of excursion taxa, which are present above and below the interval of dramatic color change (interval 199-1220B-20X-2, 48–78 cm). The excursion species include rare to abundant *Acarinina africana*, few to trace numbers of *Acarinina sibaiyaensis*, and occasional specimens of *Morozovella allisonensis*. Specimens of *A. africana* frequently display very lobate peripheries and approach a clavate chamber shape. Extreme morphotypes of *A. sibaiyaensis* with more than six chambers in the last whorl are rare, but examples with five or six loosely coiled chambers that display the low rate of chamber enlargement typical of this species are relatively common. Likewise, extreme forms of *M. allisonensis* with biconvex shells are very rare, but specimens with strongly recurved sutures and weakly developed keels similar to specimens figured by Kelly et al. (1996, 1998) are typical of examples found at Site 1220. In addition to the excursion taxa, we found a number of unusual morozovellids with only three chambers in the last whorl and the tendency to develop nontrochospiral shells. These specimens may represent aberrant forms of *M. acuta* or *Morozovella parva*. Also present in samples from adjacent to the P/E boundary are the species *Globanomalina planoconica* and *Globanomalina ovalis*, along with an unidentified compressed variety of *Chiloguembelina* and a very low trochosprial form that we refer to as *Pseudohastigerina* sp.

Benthic foraminifers suggest that the P/E boundary should be placed at the base of the series of multicolored yellow, pink, black, and brown beds, near 78 cm in Section 199-1220B-20X-2. The presence of excursion fauna such as *M. allisonensis*, *A. africana*, and *A. sibaiyaensis* below this level in Section 199-1220B-20X-2 suggests that these species evolved prior to the P/E boundary and only became abundant at other localities in the Pacific (Ocean Drilling Program [ODP] Site 865; Kelly et al., 1996), Atlantic (ODP Site 1051; Norris and Röhl, 1999), and Tethys (Egypt and Spain) (Kelly et al., 1998) during the episode of global warming associated with the P/E boundary. Unfortunately, the oldest Hole 1220B sediments that immediately overlie basalt contain all three species in the excursion fauna; therefore, we are unable to determine the evolutionary first appearance of these species using this site.

A persistent but rare member of P/E boundary planktonic foraminifer assemblages is a clavate species that we identify as *Parasubbotina paleocenica*. These specimens are mostly small (<250 µm) and have three to five fingerlike chambers that are flattened slightly when seen in edge view. The aperture is a subsymmetrical equatorial high-arched slit bordered by a distinctive lip. Whole specimens are present between Sam-

ples 199-1220B-20X-CC and 20X-2, 13–20 cm. Prior to Leg 199, *P. paleocenica*, originally described as *Clavatorella paleocenica* (see Coxall et al., in press, for discussion), has been reported only from its Paleocene type locality in Senegal, West Africa (e.g. De Klasz and De Klasz, 1986, 1988).

### Benthic Foraminifers

Benthic foraminiferal assemblages fall into two categories at this site, with clearly differentiated stratigraphic ranges. Calcareous assemblages occurred in lower Miocene, Oligocene, and lower Eocene–uppermost Paleocene sediment. The benthic foraminiferal assemblages from the Miocene and Eocene intervals consist of agglutinated foraminifers (Samples 199-1220A-2H-CC and 8H-CC and 199-1220B-4H-CC and 9H-CC through 13H-CC). Calcareous foraminifers are moderately well preserved in Samples 199-1220A-3H-CC and 4H-CC. The preservation of Oligocene calcareous foraminifers is good. However, upper Eocene and lower Paleocene foraminifers are poorly preserved, and many specimens show signs of calcite overgrowth on the test surface. Agglutinated assemblages are also poorly preserved and show low species diversity. All tube-shaped forms, such as *Rhizammina* and *Martinottiella*, are fragmented. Samples 199-1220A-1H-CC, 9H-CC, and 10H-CC and 199-1220B-5H-CC, 6H-CC, 8H-CC, 16X-CC, and 17X-CC are barren. The distribution of benthic foraminifers is reported in Table T4.

Lower Miocene and Oligocene foraminiferal assemblages are characterized by diversified species of the genera *Globocassidulina*, *Cibicidoides*, *Gyroidinoides*, and stilostomellids. Large tests of foraminiferal species such as *Cibicidoides mundulus*, *Cibicidoides grimsdalei*, *Cibicidoides praemundulus*, *Cibicidoides havanensis*, *Oridorsalis umbonatus*, and *Siphonodosaria abyssorum* are consistently present in Sections 199-1220A-3H-CC through 7H-CC. Calcareous assemblages in Sections 3H-CC through 7H-CC co-occur with deep-sea agglutinated species such as *Rhizammina* sp., *Thalmanammmina* sp., *Martinottiella communis*, *Ammovertellina* sp., *Cribrostomoides* spp., *Recurvoides* sp., and *Ammodiscus* sp. These agglutinated taxa, together with the calcareous taxa such as *C. mundulus*, *C. havanensis*, and *C. grimsdalei*, suggest lower bathyal and lower abyssal paleodepths.

Middle–upper Eocene benthic foraminiferal assemblages are poorly preserved and include only the elongate tests of *Rhizammina* sp. These depauperate agglutinated assemblages appear to indicate lower bathyal paleodepths.

Lower Eocene foraminiferal assemblages are recognized in Samples 199-1220B-18X-CC; 19X-1, 77–79 cm; 19X-CC; and 20X-2, 1.5–3.5 cm. The most common benthic foraminifers are *Abyssamina quadrata*, *A. poagi*, *Anomalinoidea praeacuta*, *Aragonina aragonensis*, *Nonion havanensis*, *O. umbonatus*, and *Nuttallides truempyi*. Of these species, the three species, *A. quadrata*, *A. poagi*, and *N. truempyi*, are extremely abundant and their total relative abundances account for 41% of Sample 199-1220B-18X-CC; 51% of Sample 199-1220B-19X-1, 77–79 cm; 33% of Sample 199-1220B-19X-CC; and 48% of Sample 199-1220B-20X-2, 1.5–3.5 cm. Other lower Eocene species are characterized by specimens that are unusually small for these taxa.

Sample 199-1220B-20X-CC contains some of the Velasco-type benthic assemblages, such as *Gavelinella beccariiformis*, *Lenticulina whitei*, *Neoflabellina semireticulata*, *Aragonina velascoensis*, *Pullenia coryelli*, *Gyroidinoides globosus*, *Gyroidinoides quadratus*, and *Neoeponides*

---

T4. Distribution of benthic foraminifers, p. 72.

---

*hillebrandti*. However, preservation of these species is poor, and the tests are overgrown with calcite crystals.

### P/E Boundary

Using glass microscope slides, 12 samples were scraped from the surface of Section 199-1220B-20X-2 and analyzed to constrain the P/E boundary. Benthic foraminifers showed dramatic changes throughout these samples. Benthic foraminifers are extremely rare in Samples 199-1220B-20X-2, 13–20 cm; 20X-2, 28–35 cm; and 20X-2, 35–43 cm, where taxa such as *N. truempyi*, *O. umbonatus*, and *Praebulimina* sp. are characterized by their small size. The foraminifers are also very thin walled. In contrast, planktonic foraminifers are very abundant and constitute a planktonic foraminiferal ooze (Fig. F7). Based on qualitative estimations, the ratio of planktonic to benthic foraminifers in these samples is ~100 to 1. Both benthic and planktonic foraminifers decrease in abundance downcore, and fragmented planktonic foraminiferal tests increase adjacent to the multicolored beds near the P/E boundary. *N. truempyi*, *O. umbonatus*, and *Praebulimina* sp. are very poorly preserved and show secondary calcite overgrowths on test surfaces in Sample 199-1220B-20X-2, 42–50 cm. Both benthic and planktonic foraminifers are absent from Samples 199-1220B-20X-2, 50–57 cm; 20X-2, 57–64.5 cm; and 20X-2, 65–72 cm. These intervals show the most marked color changes in this core and are associated with well-developed dolomite crystals. Sample 199-1220B-20X-2, 74–78 cm, includes poorly preserved *N. truempyi*, *O. umbonatus*, *Bulimina tuxpamensis*, *Gaudryina pyramidata*, and *Praebulimina* sp., all of which are heavily recrystallized. Planktonic foraminifers are rare in this sample. Members of the Velasco-type assemblage such as *G. beccariiiformis*, *Neoflabellina semicribrata*, and *L. whitei* are found in Samples 199-1220B-20X-2, 77.5–85 cm, and 20X-2, 88–95 cm. These samples contain abundant small (~160–190 μm) crystals of dolomite (Fig. F7), whose growth may account for the poor preservation of these species. Planktonic foraminifers are very rare in these samples. The stratigraphic distribution of benthic foraminifers in Section 199-1220B-20X-2 is shown in Figure F8.

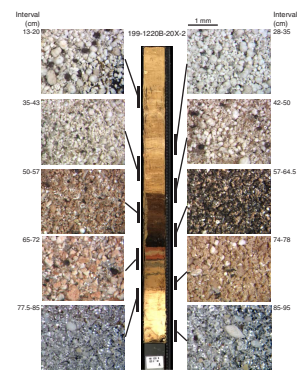
Based on the last occurrence of the taxa of the Velasco-type assemblage in Sample 199-1220B-20X-2, 77.5–85 cm, the P/E boundary is identified at a depth of 199.68 mbsf in this hole.

### Radiolarians

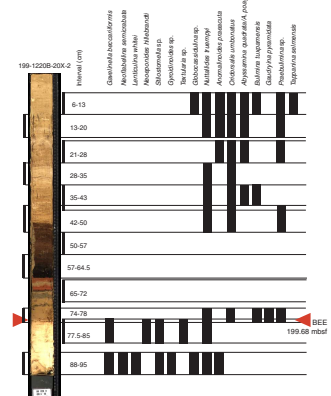
Abundant and well-preserved radiolarians are present in all recovered material except for the first two cores of Hole 1220A, which contained only trace amounts of poorly preserved nonage diagnostic forms. Radiolarian datum levels are reported in Table T5.

Samples 199-1220A-3H-2, 45–47 cm, and 3H-4, 45–47 cm, contain common but moderately well preserved species indicative of the lowermost Miocene Zone RN1. The boundary between Zones RN1 and RP22, as defined by the first appearance of *Cyrtocapsella tetrapera*, lies between Samples 199-1220A-3H-4, 45–47 cm, and 3H-5, 45–47 cm. As was the case at Sites 1218 and 1219, this is underlain by a relatively short upper Oligocene sequence (Zone RP22), an expanded upper Oligocene sequence (Zone RP21), and the single lower Oligocene Zone RP20. The boundary between Zones RP22 and RP21 lies between Samples 199-1220A-4H-2, 45–47 cm, and 4H-3, 45–47 cm. The boundary between Zones RP21 and RP20 lies between Samples 199-1220A-5H-CC and 6H-

F7. Photographs of the >63-μm fraction of washed sample from across the P/E boundary, p. 40.



F8. Stratigraphic distribution of benthic foraminifers, p. 41.



T5. Radiolarian first and last occurrences and zonal boundaries, p. 74.

1, 45–47 cm. This boundary was also documented in Hole 1220B between Samples 199-1220B-2H-4, 38–40 cm, and 2H-CC.

Material examined from Samples 199-1220A-4H-6, 45–47 cm, and 4H-CC (lower Zone RP21 and upper Zone RP20) shows considerable reworking of middle Eocene forms (e.g., *Dictyoprora mongolfieri*, *Calocyclus hispida*, *Podocyrctis [Lampterium] chalara*, *Podocyrctis [Lampterium] goetheana*, and *Thyrsoyrctis triacantha*) as does Samples 5H-CC and 6H-6, 45–47 cm. The lower part of Zone RP20 and uppermost Zone RP19 contain few to abundant diatoms in the >63- $\mu$ m fraction of Samples 199-1220A-7H-2, 45–47 cm, to 8H-4, 46–48 cm. The competitive influence of an expanded diatom flora, and probably cooler water temperatures, in this part of the stratigraphic column may account for the generally less diverse radiolarian fauna and hence a less detailed lower Oligocene biozonation. Similar influxes of diatoms were also noted at Sites 1218 and 1219 at about the same stratigraphic horizon. Zones RP21 and RP20 also include a rich orosphaerid population.

Zone RP19 crosses the E/O boundary with the division between Zones RP20 and RP19 lying between Samples 199-1220A-8H-2, 20–22 cm, and 8H-3, 46–48 cm, and Samples 199-1220B-3H-CC and 4H-CC. The boundary between the upper Eocene Zones RP19 and RP18 lies between Samples 199-1220A-8H-6, 46–48 cm, and 8H-7, 46–48 cm, and between Samples 199-1220B-4H-CC and 5H-CC. Zone RP17 was not sampled in Hole 1220B, but it must lie within Core 199-1220B-5H; in Hole 1220A, the boundary between Zones RP18 and RP17 lies between Samples 199-1220A-9H-6, 45–47 cm, and 9H-7, 45–47 cm.

The underlying middle Eocene sequence is uniformly rich in radiolarians, and all the middle Eocene radiolarian zones except RP10 can be recognized. The boundary between Zones RP17 and RP16, marked by the first occurrence of *Cryptocarpium azyx*, lies between Samples 199-1220A-10H-4, 45–47 cm, and 10H-5, 45–47 cm. Although *P. (L.) goetheana*, which marks the lower limit of Zone RP16, is scarce, the boundary between Zones RP16 and RP15 can be placed between Samples 199-1220A-11H-7, 45–47 cm, and 11H-CC and Samples 199-1220B-7H-CC and 8-CC. Zone RP14 is the lowermost Hole 1220A radiolarian zone, and its boundary with the overlying Zone RP15 is between Samples 199-1220A-12H-4, 45–47 cm, and 12H-5, 45–47 cm. In Hole 1220B, the boundary between Zones RP15 and RP14 lies between Samples 199-1220B-9H-1, 45–47 cm, and 9H-2, 45–47 cm. In Hole 1220B the boundary between Zones RP15 and RP14 lies between Samples 199-1220B-9H-1, 45–47 cm, and 9H-2, 45–47 cm.

Abundant and well-preserved radiolarians persist downhole in Hole 1220B to Zone RP11. The boundary between Zones RP14 and RP13 lies between Samples 199-1220B-10H-3, 45–47 cm, and 10H-4, 45–47 cm. The boundary between Zones RP13 and RP12 lies between Samples 199-1220B-11H-1, 45–47 cm, and 11H-2, 45–47 cm, and the boundary between Zones RP12 and RP11 lies between Samples 199-112B-12H-CC and 13H-1, 45–47 cm. The material recovered in Core 199-1220B-13H below Section 13H-3 showed characteristics of flow-in. Cores 199-1220B, 14X and 15X consist of chert fragments. Abundant and well-preserved radiolarians could again be recognized in Sample 199-1220B-16X-1, 100–102 cm, and can be placed in Zone RP8. This zone continues down to its boundary with Zone RP7 between Samples 199-1220B-17X-CC and 18X-2, 10–12 cm. No zonal assignment was possible for Sample 199-1220B-18X-CC or for subsequent cores, which are barren of radiolarians.

A similar sequence was found in the lower part of Hole 1220C. Sample 199-1220C-11H-3, 10–12 cm, belongs to either Zone RP11 or RP12, whereas Sample 199-1220C-11H-4, 10–12 cm, can definitely be placed in Zone RP11. Once more, only chert was recovered in Cores 199-1220C-12X and 13X. However, abundant and well-preserved radiolarians could again be identified in Samples 199-1220C-14X-3, 60–62 cm, and 14X-6, 60–62 cm, as belonging to Zone RP8. No radiolarians were found in subsequent cores.

## PALEOMAGNETISM

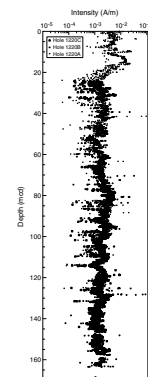
All APC cores from Holes 1220A, 1220B, and 1220C were measured on the shipboard pass-through cryogenic magnetometer. The natural remanent magnetization (NRM) was measured at 5-cm intervals in each core section, followed by three steps of alternating-field (AF) demagnetization up to a maximum peak field of 20 mT. As at previous sites, XCB cores were not measured with the exception of Core 199-1220B-20X, which had remarkably undisturbed sediment. In addition to core measurements, numerous discrete samples were taken from Hole 1220A to carry out more detailed progressive demagnetization. Only a few core sections from APC-cored intervals at Site 1220 were too disturbed to measure with the cryogenic magnetometer.

As in most of the siliceous sediments cored at previous sites, the NRM magnetization intensities were in the order of  $10^{-1}$  to  $10^{-2}$  A/m and decreased to  $\sim 10^{-3}$  A/m after partial AF demagnetization (Fig. F9). The drilling-induced overprint was mostly removed by AF demagnetization at 10 mT. Some magnetic directions did not reach a stable point at 20 mT and, despite a high grouping of antipodal directions, magnetization directions of most cores did not pass a reversal test, suggesting that the characteristic remanent magnetization has not been fully isolated in these samples. Further, shore-based stepwise demagnetization is required to isolate the primary magnetization in these sediments, particularly if a precise estimate of paleolatitudinal changes in the Paleogene is intended for Site 1220.

### Magnetic Polarity Stratigraphy

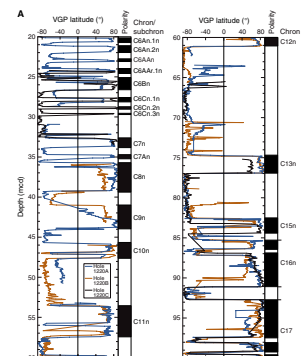
Site 1220 paleomagnetic data gave excellent results and a reliable record of geomagnetic reversals from the early Miocene to the early–middle Eocene. The splice of Holes 1220A, 1220B, and 1220C shows an excellent match. The VGP latitude changes were also used to splice the cores to the composite depth scale (Table T6; Fig. F10). Correlation of the obtained magnetic stratigraphy to the GPTS shows a record from Subchron C6An.1n to Chron C21n (Fig. F10). Hole 1220B is the deepest hole drilled at Site 1220, and the recovered section is correlatable to chrons from C21 (partially recovered at  $\sim 170$  mcd) to C8n, at  $\sim 38$  mcd. Holes 1220B and 1220C were designed to complement gaps in the Hole 1220A record, particularly in the top and middle parts of the section. Hole 1220C was particularly useful in anchoring Subchrons 6B and 6C to the GPTS, as a gap of  $\sim 3$  m exists between Cores 199-1220A-3H and 4H (see also “Composite Depths,” p. 19). Data retrieved from Hole 1220B reproduced and complemented results previously obtained in Hole 1220A. The composite magnetic stratigraphy for Site 1220 faithfully reproduces  $\sim 20$  m.y. of geomagnetic polarity history.

F9. Magnetization intensities after AF demagnetization, p. 42.



T6. Composite depths of geomagnetic reversals, p. 75.

F10. Composite magnetic stratigraphy, p. 43.



## COMPOSITE DEPTHS

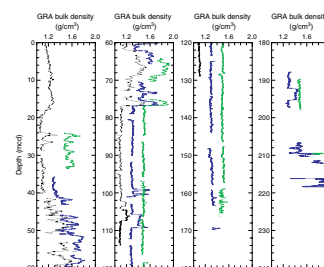
A composite section was constructed for the upper 144 mcd of Site 1220 using multisensor track (MST) and color reflectance data to determine depth offsets between cores from Holes 1220A, 1220B, and 1220C (Figs. F11, F12). In Hole 1220A, MS and color reflectance data were collected at 2-cm intervals and gamma ray attenuation (GRA) bulk density at 4-cm intervals down to Core 199-1220A-10H, below which GRA bulk density data were acquired at 2-cm intervals. GRA bulk density data were collected at 2-cm intervals throughout cores from Holes 1220B and 1220C. *P*-wave velocity data were collected at 2-cm intervals through Core 199-1220A-11H and from Cores 199-1220B-4H through 13H. No *P*-wave data were collected in the XCB portion of Hole 1220B or in any core of Hole 1220C. Minolta spectrophotometer data were collected in all three holes at 2-cm intervals. Readings from the natural gamma ray (NGR) instrument showed only background radiation levels below ~50 mbsf. This component from the MST assemblage was only run in Hole 1220A. Disturbed intervals, as determined by visual inspection of split cores, are listed in Table T7. Data from these intervals were removed prior to correlation work. Table T8 lists the offsets that were applied to cores from each hole to create a composite depth record.

Cores from Site 1220 overlap and form a continuous sedimentary sequence down to ~144 mcd (base of Core 199-1220B-10H) (Figs. F11, F12). Between 144 and 166 mcd, cores were placed into a composite depth framework, but a continuous section could not be constructed over this interval because gaps were aligned and it was not always possible to establish the true stratigraphic position of the cores. For example, Cores 199-1220B-11H and 199-1220C-10H can be correlated to each other but not to cores above or below. Figures F11 and F12 show that in this interval, between 148 and 158 mcd, the position of these cores is not constrained with respect to Hole 1220B or Hole 1220C or with respect to other intervals above or below in either hole.

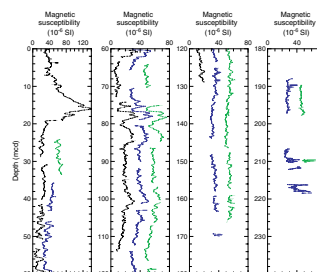
The first cores from Holes 1220B and 1220C recovered sediments from >34 and >25 mbsf, respectively, so there is no spliced record available for the interval covered by Cores 199-1220A-1H and 2H. However, this interval of predominantly radiolarian clay was recovered in the site survey piston Core EW9709-13PC (Lyle, 2000), and the bulk density and MS records between Site 1220 and the site survey core correlate well. The GRA bulk density record at Site 1220 (Fig. F11) shows several section-long intervals (~100 and 195 mcd, respectively) that have values offset from the background GRA record by 0.15 g/cm<sup>3</sup>. This offset does not correspond to any lithologic, physical, or geochemical change in the core and is an electronic artifact that occurred during data collection.

Following construction of the composite depth section for Site 1220, a single continuous spliced record was assembled for the aligned cores down to ~144 mcd by patching across cores to cover gaps with data primarily from Holes 1220A and 1220B above 95 mcd and Holes 1220B and 1220C below 95 mcd (Table T9; Fig. F13). Intervals having significant disturbance or distortion (see Table T7) were avoided. The lithology-dependent correlation or anticorrelation of MS and GRA bulk density measurements are illustrated in Figure F14. Intervals that are dominated by varying calcium carbonate (CaCO<sub>3</sub>) content show a clear cyclical signal as well as an anticorrelation between MS and GRA bulk density.

F11. GRA bulk density data plotted vs. composite depth, p. 45.



F12. Magnetic susceptibility data plotted vs. composite depth, p. 46.

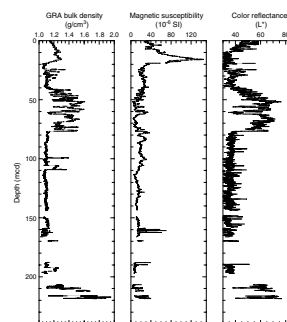


T7. Core disturbance intervals, p. 76.

T8. Composite depth offsets, p. 77.

T9. Splice tie points, p. 78.

F13. Spliced records of GRA bulk density, magnetic susceptibility, and color reflectance parameter, p. 47.



The Site 1220 splice can be used as a sampling guide to recover a continuous single sedimentary sequence down to 144 mcd. When utilizing this splice as a sampling guide, it is advisable to overlap a few decimeters from different holes when sampling in order to accommodate anticipated ongoing development of the depth scale. Stretching and compression of sedimentary features in aligned cores indicates distortion of the cored sequence. Because much of the distortion occurs within individual cores on depth scales of <9 m, it was not possible to align every feature in the MST and color reflectance records. However, at crossover points along the splice (Table T9), care was taken to align highly identifiable features from cores in each hole. Postcruise work will establish a detailed correlation between holes by establishing a revised meters composite depth scale that allows differential stretching and squeezing within cores, following Hagelberg et al. (1992).

## SEDIMENTATION AND ACCUMULATION RATES

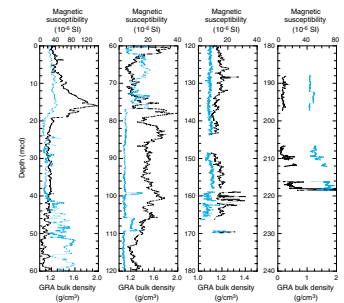
All the principal biostratigraphies, plus an extensive set of over 60 paleomagnetic reversals, are defined in Holes 1220A, 1220B, and 1220C (Tables T10, T11). Paleomagnetic reversals are used to calculate the average linear sedimentation rates (LSRs) for Site 1220 through most of the section. The first reliable paleomagnetic reversals are found in Core 199-1220A-3H, along with the youngest radiolarian events, and extend through the section recovered by APC methods. The age of the base of the hole is based on the identification of the BEE in Section 199-1220B-20X-2 (Table T11).

Calcareous nannofossils and radiolarians are present in the uppermost part of the fossiliferous section in the lower Miocene (Fig. F15). From the lower Miocene to the base of the Oligocene, both nannofossils and radiolarians were useful in establishing age control. In most of the Eocene, only radiolarians are present (Fig. F15), although both nannofossils and foraminifers are found in the chalks at the very base of the section of lithologic Unit IV.

Based on a simple linear interpolation from the sediment surface (assumed to be zero age) and the first identifiable paleomagnetic reversal (Tables T10, T11), the clays of lithologic Unit I (see “Lithostratigraphy,” p. 6) have an LSR near 1 m/m.y. Piston Core EW9709-13P (Lyle, 2000), taken in the survey area, can be correlated to the density records of Site 1220A (Fig. F16). By mapping the density record of the upper part of Hole 1220A (Tables T10, T11) onto the density record of piston Core EW9709-12P, we can determine the LSR of the piston core relative to the assumed constant sedimentation rate of Hole 1220A. This comparison indicates an interval of relatively rapid sedimentation in the piston core near 15 Ma (Figs. F16, F17). Above this interval, the LSR of the piston core is less than half that of Hole 1220A. Below the relative peak in LSR, the piston core has about the same accumulation rate as assumed for the upper part of Hole 1220A (Fig. F17).

The LSR at Site 1220 in the alternating siliceous and calcareous clays of lithologic Units II and III reaches ~5.5 m/m.y. in the Oligocene part of the section (Tables T10, T11; Fig. F15). This sedimentation rate continues through the E/O boundary into the upper Eocene with no significant change, despite the disappearance of carbonate from the Eocene sediments. A second maximum in LSR of ~8.3 m/m.y. is present in the silica-rich middle Eocene radiolarian ooze of lithologic Unit IV (Fig. F15). The LSR apparently drops slightly (to ~6.6 m/m.y.) near the top of

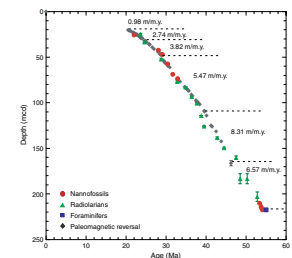
F14. Spliced records of GRA bulk density and magnetic susceptibility, p. 48.



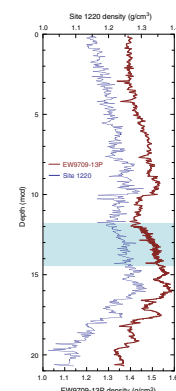
T10. Paleomagnetic events, p. 79.

T11. Nannofossils, foraminifers, and radiolarian events, p. 80.

F15. LSR and chronostratigraphic markers, p. 49.



F16. Density of Core EW9709-13P compared to density record of Hole 1220A, p. 50.



the lower Eocene with the appearance of the first significant chert layers.

LSR data may be combined with the dry bulk density (DBD) data (see “Physical Properties,” p. 24) (Table T16) to determine the bulk mass accumulation rates (MARs) of the sediments (Table T12). Sediment with an LSR of 1.0 cm/k.y. and a DBD of 1.0 g/cm<sup>3</sup> will have an MAR value of 1.0 g/cm<sup>2</sup>/k.y. The observed values are rarely this high, so we report the data as milligrams per square centimeter per thousand years (mg/cm<sup>2</sup>/k.y.).

MAR values are low in lithologic Unit I, generally <75 mg/cm<sup>2</sup>/k.y. (Fig. F18). Lithologic Unit II, dominated by siliceous ooze, accumulates at flux rates up to 100 mg/cm<sup>2</sup>/k.y. Maximum flux rates of 400–500 mg/cm<sup>2</sup>/k.y. occur in lithologic Unit III, the very light brown nannofossil ooze of early Oligocene age. Unit IV, dominated by radiolarian ooze and radiolarite, has much lower MARs of ~160 mg/cm<sup>2</sup>/k.y. in the upper portion to ~300 mg/cm<sup>2</sup>/k.y. in the period between ~40 and 46 Ma. The basal chalk of Unit V accumulated at rates of ~400–600 mg/cm<sup>2</sup>/k.y.

## GEOCHEMISTRY

### Interstitial Water Geochemistry

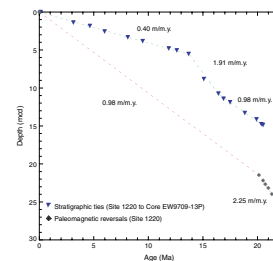
We collected interstitial waters from 11 samples from Site 1220 at intervals of approximately one sample every core for the first six cores and every third core thereafter (Table T13; Fig. F19). Eight samples from Hole 1220A, at depths ranging from 4.45 to 110.45 mbsf, and three samples from Hole 1220B, at depths ranging from 125.89 to 173.55 mbsf, together comprise the interstitial water profile for Site 1220. Chemical gradients in the interstitial waters at Site 1220 primarily reflect relatively limited organic matter diagenesis, dissolution of biogenic silica, little carbonate, and possibly diffusive influence of reactions in the underlying basalt.

Chlorinity, as measured by titration, increases with depth from 554 mM at 4.45 mbsf to a mid-depth maximum of 566 mM at 80.45 mbsf (Fig. F19). This pattern is very similar to the chlorinity pattern at Site 1219. The lower than average seawater value of interstitial water at shallow sediment depth (4.45 mbsf) at this site is consistent with the chlorinity of modern Pacific bottom waters (~542 mM). Sodium concentrations determined by charge balance were on average 2.4% lower than those measured by ion chromatograph and are consistent overall with the chlorinity values (Table T13). Sodium concentrations determined by charge balance are low (477mM, as compared to the average seawater value of 480 mM) at 4.45 mbsf and increase to a middepth maximum (487 mM) at 80.45 mbsf. Salinity, as measured by a handheld refractometer, varies slightly from 35.0 in the shallower part of the hole (4.45–51.95 mbsf) to 35.5 in the deeper part of the hole (80.45–173.55 mbsf).

Alkalinity generally decreases with depth from 4.45 to 173.55 mbsf. The pH varies between 7.14 at the seafloor (4.45 mbsf) to 7.39 at the bottom of the profile (173.55 mbsf). Like all other Leg 199 sites, sulfate concentrations are high (28.6 ± 1 mM) throughout the profile, indicating little oxidation of labile organic matter. Ammonium, a byproduct of organic matter degradation, is present in extremely low levels (≤5 μM).

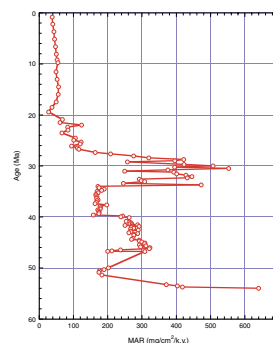
Dissolved silica concentrations increase with depth, from 556 μM at 4.45 mbsf to ~900 μM at 154.45 mbsf. These high interstitial water sil-

F17. Age vs. depth plots for Site 1220 and Core EW9709-13P, p. 51.



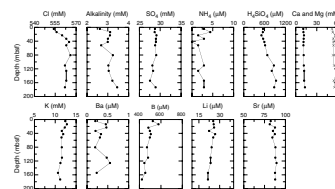
T12. Depths, ages, rates, and fluxes of sediments, p. 81.

F18. MARs of sediments, p. 52.



T13. Interstitial water data, p. 83.

F19. Interstitial water data, p. 53.



ica values are consistent with dissolution of biogenic silica throughout the sediment.

Calcium and magnesium concentrations are similar to those seen at all other Leg 199 sites except Site 1219. At Site 1220, calcium, magnesium, and potassium profiles show little evidence for exchange with basalt and subsequent diffusion. Calcium concentrations increase slightly downhole, from 10.7 mM (4.45 mbsf) to 13.1 mM (173.55 mbsf). Magnesium concentrations increase from 51.5 mM (4.45 mbsf) to 59.0 mM (125.89 mbsf) and then decrease to 55.0 mM in the deepest sample (173.55 mbsf). Potassium concentrations show only a small decrease with depth, from 12.4 mM (4.45 mbsf) to 10.6 mM (154.45 mbsf). Lithium pore water values are similar to that of seawater (27  $\mu$ M) at 4.45 mbsf and show a small decrease with depth, consistent with alteration with basalt and subsequent diffusion.

Strontium concentrations (82  $\mu$ M) are lower than seawater value (87  $\mu$ M) at the top of the hole but show a small increase to seawater value at 23 mbsf. Dissolved manganese was 27  $\mu$ M in the shallowest sample (4.45 mbsf) but was below detection limit for all other samples. Barium concentrations are low (<0.6  $\mu$ M) throughout the sediment column; the deepest sample at 173.55 mbsf in Hole 1220B was below detection limit (0.04  $\mu$ M). Manganese concentrations are below detection limit. Boron concentrations range from 423 to 505  $\mu$ M.

In summary, the pore water profiles from Site 1220 primarily reflect minor organic matter degradation, the dissolution of biogenic silica, and minor alteration of underlying basalt. Overall, the profiles from Site 1220 are very similar to the profiles of all other Leg 199 sites except Site 1219.

### Solid-Phase Geochemistry

We collected bulk-sediment samples adjacent to the interval sampled for physical properties in every other section (see “Physical Properties,” p. 24) at Site 1220, resulting in a sampling resolution of approximately three samples per core. The profile is composed of sediments from 2.24 to 112.73 mbsf for Hole 1220A and from 114.23 to 193.14 mbsf for Hole 1220B (depths in both mcd and mbsf are provided in Table T14 and Fig. F20). We also analyzed continuous scrapings (26 samples of 2–7 cm in width between 198.90 and 199.79 mbsf) from the P/E boundary core section (199-1220B-20X-2), resulting in the first ever shipboard analysis of bulk-sediment geochemistry across this paleoceanographically important interval.

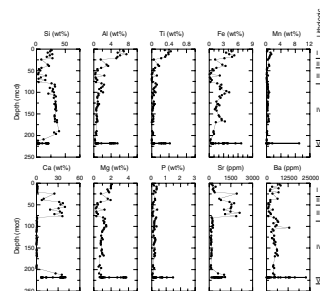
Bulk-sediment geochemistry primarily reflects the changing lithology of the sediments downhole from clay (Unit I) to radiolarian ooze (Unit II) to nannofossil ooze (Unit III) to radiolarian ooze (Unit IV) and, finally, to nannofossil chalk (Unit V) (Fig. F20). Trends in the P/E boundary section are discussed separately.

Silicon in Site 1220 sediments is <25 wt% in lithologic Units I–III (0–70 mcd) and increases to ~30 wt% in Unit VI (70–190 mcd). Silicon concentrations fall to <5 wt% in Unit V (Fig. F20). Aluminum and titanium concentrations are linearly related ( $R = 0.96$ ). Aluminum concentrations are high in the clay sediments (~6 wt%; Unit I) and low in the carbonate and siliceous sediments (generally <3 wt%; Units II–V). Titanium concentrations show the same pattern and are generally 0.30 wt% in Unit I and <0.05 wt% in Units II–V.

Iron, manganese, and magnesium contents show similar trends to each other (Fig. F20). All are generally highest in the clay sediments

T14. Bulk-sediment data, p. 84.

F20. Bulk-sediment data, p. 54.



(Unit I), decrease to a mid-depth minimum in Unit III at ~75 mcd, and then increase in Unit IV. Iron decreases from 4.5 to <1 wt% between 2.24 and 76.39 mcd then increases to a peak of 4.2 wt% at 100.06 mcd. Iron content then decreases to 0.30 wt% at 208.84 mcd and remains low throughout Unit V. Manganese concentrations are slightly elevated (up to 1.34 wt%) in Unit I (between 0 and 30 mcd) and subsequently decrease to <0.60 wt% throughout Unit V. Magnesium concentrations decrease from 2.10 wt% at the top of Unit I to 0.30 wt% at the bottom of Unit III and increase slightly to ~1.3 wt% in Units IV and V.

Calcium and strontium concentrations are highest in the more carbonate-rich lithologies (Units II, III, and V). Calcium concentrations are low in Units I and IV (<1 wt%) and high in Units III and V (as high as 40 wt%, although these values are out of the range of the standards) (see “**Geochemistry**,” p. 20, in the “Explanatory Notes” chapter). The variability in calcium (7–35 wt%) throughout Unit III reflects layers of alternating nannofossil ooze and radiolarian ooze in the sediment (see “**Unit III**,” p. 7, in “Lithostratigraphy”). Strontium concentrations are lowest (as low as 100 ppm) in Units I and IV and highest (as high as 2000 ppm) in the carbonate-rich lithologies (Units III and V).

Phosphorus and barium concentrations in Site 1220 sediments follow each other ( $R = 0.8$ ). Phosphorous concentrations are low (generally <0.5 wt%). Barium concentrations in Site 1220 sediments are variable (between 800 and 13,000 ppm).

CaCO<sub>3</sub> (in weight percent) was determined by coulometric methods for three samples per core from 2.24 to 211.85 mcd for Site 1220 (Table T15; Fig. F21). CaCO<sub>3</sub> is low (≤1 wt%) in clay-rich Unit 1, variable (~20–100 wt%) in Units II and III, low (<1 wt%) in siliceous Unit IV, and high (up to 87 wt%) in Unit V. CaCO<sub>3</sub> values calculated from inductively coupled plasma–atomic emission spectroscopy determined Ca data (in weight percent) and salt fraction data (in weight percent) yielded similar trends to calcium carbonate measured via the coulometer, although absolute values are generally lower for CaCO<sub>3</sub> <1 wt% and higher for CaCO<sub>3</sub> >1 wt% (see “**Geochemistry**,” p. 20, in the “Explanatory Notes” chapter).

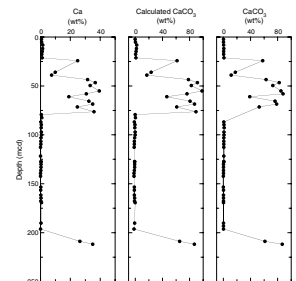
In summary, the bulk geochemistry of the sediments from Site 1220 reflect the shifts in lithology between sediments dominated by silica and carbonate.

### P/E Boundary

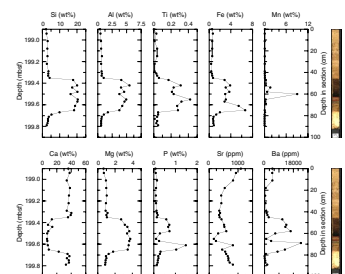
Significant changes in bulk geochemistry are seen across the P/E boundary (Table T14; Fig. F22). Continuous scrapings at intervals of 2–7 cm from Section 199-1220B-20X-2 (between 198.90 and 199.79 mbsf) were analyzed. The highest concentrations of Fe, Mn, Ca, Mg, Ba, and P for Site 1220 are present in this core section. Silicon, aluminum, and magnesium show similar trends of elevated concentrations (~20, 4, and 3.7 wt%, respectively) above their Unit V background concentrations between 47 and 77 cm in this section. Over the same interval, calcium shows the opposite trend (~6 wt% below its Unit V background concentration). Strontium generally decreases downsection to the dark brown lithology, has a distinct minima centered at 65–67 cm, and an isolated peak at 69–73 cm in the section. Strontium concentrations in the carbonate lithology at the base of the section generally increase downsection, away from the color change, possibly reflecting a decrease in the extent of carbonate recrystallization. Manganese concentrations are

T15. CaCO<sub>3</sub> and C<sub>org</sub> data, p. 86.

F21. CaCO<sub>3</sub> and Ca data, p. 55.



F22. Bulk-sediment data for the P/E boundary, p. 56.



low overall but show a single peak (9 wt%) at 60–63 cm, corresponding to the darkest sediments in the section. Iron concentrations increase to ~4 wt% at 47–54 cm and peak at 7 wt% at 75–77 cm in the section. Likewise, titanium concentrations increase to ~0.31 wt% at 52–54 cm and peak at 0.42 wt% at 65–67 cm in the section. Phosphorus and barium concentrations show similar trends, increasing between 45–47 cm and 58–60 cm, decreasing to a minima at 65–67 cm, and increasing to a maximum at 69–73 cm.

## PHYSICAL PROPERTIES

Physical properties at Site 1220 were measured on whole cores, split cores, and discrete samples. MST measurements (bulk density, MS, *P*-wave velocity, and NGR) and thermal conductivity comprised the whole-core measurements. Compressional wave velocity measurements on split cores and moisture and density (MAD) analyses on discrete core samples were made at a frequency of one per undisturbed section in Hole 1220A and in Hole 1220B, Cores 199-1220B-9H through 20X. Light absorption spectroscopy (LAS) analyses were performed on the MAD samples as well as an additional one sample per section (located ~50 cm from the MAD sample). Three in situ temperature measurements were obtained using the Adara tool in Hole 1220B.

### Density and Porosity

Two methods were used to evaluate the wet bulk density at Site 1220. GRA provided an estimate from whole cores. MAD samples are a second, independent measure of wet bulk density, along with providing DBD, grain density, water content, and porosity from discrete samples (Table T16). The MAD wet bulk densities are ~0.05 g/cm<sup>3</sup> greater than the GRA bulk density in the clay of lithologic Unit I (0–19.1 mbsf) (Fig. F23). In the radiolarian oozes of Units II (19.1–38.0 mbsf) and IV (70.6–182.5 mbsf), the discrete sample densities are consistently 0.10 g/cm<sup>3</sup> greater than the GRA density. The two density measures are more nearly equal in the nannofossil ooze of Unit III (38.0–70.6 mbsf) and the nannofossil chalk of Unit V (187.9–200.0 mbsf). The latter unit was drilled with the XCB, but the gaps between the sediment and core liner were minimal and the match between the data sets is good.

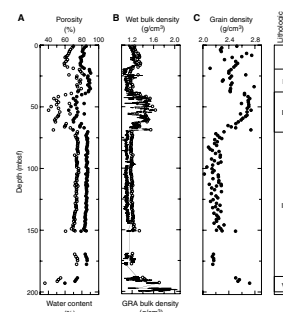
The P/E boundary section within Unit V (Section 199-1220B-20X-2) (see “P/E Sediments,” p. 8, in “Lithostratigraphy”) was well imaged by the GRA detector (Fig. F24). The boundary is marked by a change in density from 1.32 g/cm<sup>3</sup> in the dark colored, clay-rich sediment above the boundary to 1.77 g/cm<sup>3</sup> in the calcareous chalk below the boundary. The increase in metal oxides directly above the boundary is not great enough to substantially increase the bulk density (see “P/E Boundary,” p. 23, in “Geochemistry”).

In three short intervals (92.9–94.0, 95.6–99.9, and 173.6–176.4 mbsf), GRA densities are displaced to values 0.10 to 0.15 g/cm<sup>3</sup> greater than adjacent GRA densities. The offset is an electronic artifact. Crossplots of wet bulk density and DBD vs. interpolated GRA density (Fig. F25) show excellent correlation between the MAD and GRA data for sediments recovered with the APC and XCB.

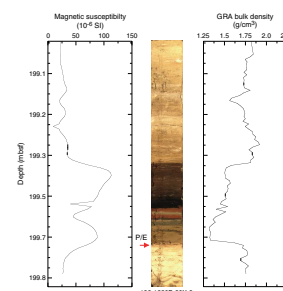
In Unit I, the clay increases in bulk density with depth as a result of compaction, from 1.25 g/cm<sup>3</sup> near the surface to 1.35 g/cm<sup>3</sup> at 16.25 mbsf. From 16.25 mbsf to the base of Unit I, density decreases as a re-

T16. Moisture and density measurements, p. 87.

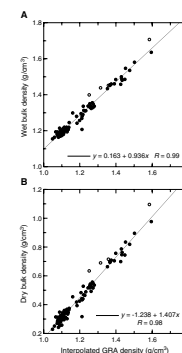
F23. MAD measurements, p. 57.



F24. Comparison of MS and GRA density at the P/E boundary, p. 58.



F25. Wet and dry bulk density plotted with GRA density, p. 59.



sult of the transition to the lower-density radiolarian oozes of Unit II. The average wet bulk density of Unit II is 1.19 g/cm<sup>3</sup>. The variable bulk density in Unit II (from 1.16 to 1.31 g/cm<sup>3</sup>) reflects the interbedding of clay and nannofossil ooze with radiolarian ooze. The wet bulk density of Unit III is higher, averaging 1.42 g/cm<sup>3</sup>, as a result of the predominance of nannofossil ooze in the unit. Radiolarian ooze and clay are interbedded with the nannofossil ooze in Unit III, resulting in a significant range in density, from 1.19 to 1.64 g/cm<sup>3</sup>. Unit IV is characterized by uniform wet bulk density. Excluding a stiff clay layer with a density of 1.34 g/cm<sup>3</sup> at 150.25 mbsf, density ranges only from 1.17 to 1.25 g/cm<sup>3</sup> for Unit IV. The expected increase in density with increasing overburden is minimal for the radiolarian ooze in Unit IV, most likely the result of an open fabric formed by interlocking radiolarians that resists particle rearrangement and collapse. For the sediments in Unit IV recovered with the APC (70.6–152.0 mbsf), wet bulk density increases at a rate of 0.027 g/cm<sup>3</sup> per 100-m depth. Wet bulk density increases sharply to 1.40 g/cm<sup>3</sup> at the boundary between Units IV and V. Within Unit V, density increases with depth, with a maximum of 1.71 g/cm<sup>3</sup> in the nannofossil chalk of Core 199-1220B-19X at 192.94 mbsf. Core 199-1220B-20X was not sampled, but a maximum bulk density of ~2.04 g/cm<sup>3</sup> was measured by the GRA device in Section 199-1220B-20X-2 at 198.55 mbsf.

Variation in grain density ( $\rho_s$ ) also corresponds well to the changes in lithology at Site 1220 (Fig. F23). The clays of Unit I display grain densities that range from 2.11 to 2.75 g/cm<sup>3</sup>. The range is typical of other pelagic clays at Leg 199 sites and is attributed to the range of densities in the mixture of smectite ( $\rho_s = 2.2\text{--}2.6$  g/cm<sup>3</sup>), zeolite ( $\rho_s = 2.1\text{--}2.6$  g/cm<sup>3</sup>), and calcite ( $\rho_s = 2.7$  g/cm<sup>3</sup>). Grain density is lower in Unit II, with most values clustered about 2.42 g/cm<sup>3</sup>, although the range in densities is from 2.30 to 2.78 g/cm<sup>3</sup>. Between the top of Unit III (38 mbsf) and 57 mbsf, grain density of the nannofossil ooze is ~2.70 g/cm<sup>3</sup>. Below 57 mbsf, grain density decreases steadily to the top of Unit IV. Grain density for the radiolarian ooze of Unit IV, excluding the stiff clay at 150.25 mbsf, averages 2.20 g/cm<sup>3</sup> and ranges from 2.03 to 2.50 g/cm<sup>3</sup>. The nannofossil chalk of Unit V is characterized by grain density that increases from 2.50 g/cm<sup>3</sup> at its top to 2.71 g/cm<sup>3</sup> at 192.94 mbsf.

Porosity and water content vary inversely with wet bulk density (Fig. F23). In Unit I, porosity decreases with depth as a result of clay compaction, from 85% near the seafloor to 80% at the base of the unit. The radiolarian-rich sediments of Units II and IV are marked by high porosities, which average 88% and 85%, respectively. A slight decrease in porosity with depth occurs in Unit IV. A wide range in porosity, from 64% to 87%, characterizes the alternating nannofossil ooze and radiolarian ooze in Unit III. The porosity of the bulk of the nannofossil ooze in this unit varies between 70% and 75%. Porosity is significantly lower in Unit V, ranging from 75% at the top of the nannofossil chalk to 60% at 192.94 mbsf.

MAD analyses were performed on three chert samples, two from Unit IV (Samples 199-1220B-15X-CC, 0–2 cm, and 17X-CC, 4–6 cm) and one from Unit V (Sample 199-1220B-19X-1, 0–2 cm) (Table T16). The average wet bulk density, grain density, and porosity for the Unit IV cherts are 2.11 g/cm<sup>3</sup>, 2.33 g/cm<sup>3</sup>, and 16.9%, respectively. The chert from Unit V is distinctly harder. Wet bulk density, grain density, and porosity for this rock are 2.52 g/cm<sup>3</sup>, 2.61 g/cm<sup>3</sup>, and 5.7%, respectively, indicating more complete conversion to quartz.

## LAS

LAS studies were conducted on sediments from Hole 1220A and Cores 199-1220B-9H through 19X at a frequency of two samples per undisturbed section (see [Vanden Berg and Jarrard](#), this volume, for a discussion of the LAS technique). Semiquantitative mineral concentrations were calculated from the collected spectra, assuming a four-component system: calcite, opal, smectite, and illite (Table [T17](#)). The results of the LAS analyses correlate well with the major lithologic boundaries (Fig. [F26](#)).

Lithologic Unit I is composed of smectite-rich (average = 84%) clay, with minor amounts of opal and calcite. The illite–smectite transition is not present in this section because of poor recovery of the water/sediment interface. Except for a few anomalous high values, illite concentrations for the most part are negligible at Site 1220, similar to all other sites. The radiolarian ooze of lithologic Unit II is marked by the expected decrease in clay (to an average of 40%) and increase in opal (from an average of 8% in Unit I to an average of 26% in Unit II). The high calcite samples (~70%) at 24 mbsf represent an interval of nannofossil ooze (see “[Unit II](#),” p. 6, in “[Lithostratigraphy](#)”).

Lithologic Unit III is composed of calcite-rich nannofossil ooze. Calcite concentrations increase from an average of 7.0% in Unit I and 29% in Unit II to an average of 73% in Unit III. Conversely, smectite concentrations drop to an average of 13% in Unit III and opal concentrations to an average of 11%. The radiolarian ooze of lithologic Unit IV contains an average of 48% opal, 37% smectite, and 12% calcite. Clay contents also increase downhole from concentrations of ~25% near the top of Unit IV to ~40% near the bottom of this unit. This downhole increase in LAS-calculated clay concentration matches the description for clay content of the Unit IV lithology (see “[Unit IV](#),” p. 7, in “[Lithostratigraphy](#)”). The stiff clay interval at 150.25 mbsf is distinctly different than adjacent sediments and is characterized by a smectite concentration of 76% and a negligible opal content. An increase in calcite (and subsequent decrease in opal) at 193 mbsf reflects the presence of nannofossil chalk in Unit V.

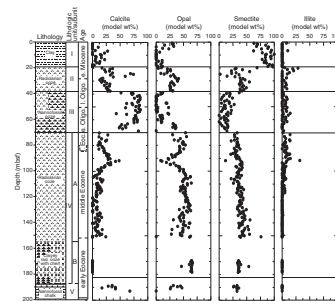
## Compressional Wave Velocity

Compressional wave velocity was measured by the *P*-wave logger (PWL) on all whole cores from Hole 1220A and Cores 199-1220B-1H through 16X. The insertion and contact probe systems were used to measure velocities on split cores from Hole 1220A and Cores 199-1220B-9H through 19X (Table [T18](#)). For Units I and III, the agreement between the PWL and split core velocities is good. The data sets diverge in the radiolarian ooze of Units II and IV. The split-core transverse velocities are ~15 m/s greater than PWL velocities in Unit II and 25 m/s greater than PWL velocities in Unit IV (Fig. [F27](#)). In Unit II, the PWL and split-core velocities follow the same trends; however, a consistent pattern of variation is lacking for the PWL and contact probe velocities in Unit IV.

In Unit I, velocity increases from 1500 m/s near the seafloor to 1550 m/s at 19 mbsf (Fig. [F27](#)). Velocities in Unit II average 1545 m/s. Lower velocities between 24 and 26 mbsf coincide with more dense lighter-colored sediment, which represent an increase in calcareous constituents in the radiolarian ooze. Unit III displays more variability in velocity than the other lithologic units, with split-core velocities ranging

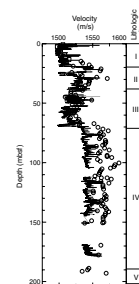
[T17](#). LAS-based mineralogy, p. 88.

[F26](#). LAS mineralogy determinations, p. 60.



[T18](#). Split-core velocity measurements, p. 90.

[F27](#). Compressional wave velocity, p. 61.



from 1509 to 1558 m/s. The general pattern is that more dense calcareous intervals are characterized by lower velocities than the less dense siliceous intervals. Velocities increase markedly at the top of Unit IV. The transverse velocity determined by the contact probe averages 1565 m/s for the radiolarian oozes of this unit; whereas, the PWL velocities are ~1540 m/s in the unit. The coarse grain size of the radiolarian ooze and possible dewatering between PWL and split-core measurements may result in higher contact probe velocities. Velocities in the nannofossil ooze of Unit V are lower than velocities in the overlying radiolarian ooze. The average velocity for Unit V is 1548 m/s, with a maximum velocity of 1570 m/s at 192.95 mbsf. Velocities measured for the three chert pieces that were sampled range from 3180 m/s for the cherts from Unit IV to 4893 m/s for the chert from Unit IV (Table T18).

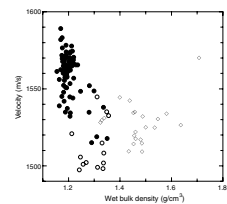
The crossplot of velocity and wet bulk density (Fig. F28) shows lithology-dependent differences in the relationship between velocity and the bulk-sediment properties. The clays of Unit I, the nannofossil oozes of Unit III, and the nannofossil chinks of Unit V are characterized by a general increase in velocity with increasing density. The radiolarian oozes of Units II and Unit IV display either no relationship between density and velocity or a weak increase in velocity with decreasing density. The lack of a relationship between density and velocity results from the stiff sediment framework created by the shape of radiolarians and their interlocking spines. This stiffness produces a higher shear modulus and velocities higher than expected for the high porosity of the sediment.

Velocity anisotropy was calculated from longitudinal (z-direction) and transverse (y-direction) measurements provided by the insertion probe system and the cut samples measured with the contact probe system (Table T18) in order to examine the burial transformation of sediment fabric. The clays of Unit I are essentially isotropic, with an average anisotropy of 1.0%. Velocity anisotropy was determined for the two chert pieces from Unit IV, which contain different colored laminae. Anisotropies of 5.2% and -1.6% were determined for Samples 199-1220B-15X-CC, 0-2 cm, and 17X-CC, 4-6 cm, respectively, suggesting residual presence of bedding in the chert.

## Thermal Conductivity and Temperature Measurements

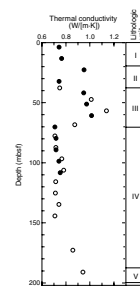
Thermal conductivity was measured on the third section of all cores from Hole 1220A and Cores 199-1220B-1H through 18X (Table T19). The conductivity is low in the clays of Unit I and the radiolarian oozes of Unit II (Fig. F29). Excluding an anomalous value of 0.95 W/(m·K) at 22.71 mbsf, the average thermal conductivity for Units I and II is 0.75 W/(m·K), which is typical for similar sediments at other Leg 199 sites. Conductivity is higher and more variable in the nannofossil ooze of Unit III. From the top of Unit III to 56.76 mbsf, it increases with depth, reaching a maximum of 1.14 W/(m·K). Below 56.76 mbsf, conductivity decreases with depth to 0.71 W/(m·K) at the top of Unit IV. Thermal conductivity is nearly constant in the Unit IV radiolarian ooze and clay, averaging 0.74 W/(m·K). The one conductivity measurement in the nannofossil chalk of Unit V has a value of 0.94 W/(m·K). The pattern of thermal conductivity dependence on porosity is similar to that at Sites 1218 and 1219 (Fig. F30). Conductivity increases with decreasing porosity for clay and nannofossil ooze sample, as a result of the decrease in the interstitial spacing. Thermal conductivity in the radiolarian oozes does not display a relationship with porosity because of the uniformly

F28. Compressional wave velocity with wet bulk density, p. 62.

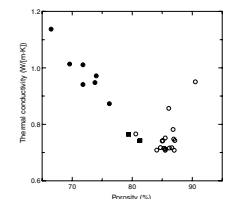


T19. Thermal conductivity, p. 91.

F29. Thermal conductivity, p. 63.



F30. Thermal conductivity with porosity, p. 64.



high porosity, ~85%, and the poor heat conduction in the biogenic silica that comprises the radiolarians.

In situ temperature measurements were taken using the Adara tool for three cores in Hole 1220B. Borehole temperatures range from 4.50°C at 49.50 mbsf to 7.15°C at 102.50 mbsf, with an average seafloor temperature of 1.45°C (Table T20; Fig. F31).

Heat flow at Site 1220 was determined according to the procedure of Pribnow et al. (2000). The laboratory-determined thermal conductivity was used to estimate in situ thermal conductivity (see “Heat Flow Calculation,” p. 28, in “Physical Properties” in the “Explanatory Notes” chapter). The thermal resistance was calculated assuming constant in situ conductivities in four layers, 0.72 W/(m·K) for Units I and II, 0.96 W/(m·K) for Unit III, 0.71 W/(m·K) for Unit IV, and 0.93 W/(m·K) for Unit V (Fig. F31). Thermal resistance was estimated for the depths of the temperature measurements, and the heat flow was obtained from the inverse of the linear fit for the cross plot of temperature and thermal resistance (Fig. F31). The heat flow estimate for Site 1220 is 46 mW/m<sup>2</sup>, which is significantly lower than the 66 mW/m<sup>2</sup> determined for only slightly younger crust at Site 1219. The value calculated for Site 1220 is consistent with the 44 mW/m<sup>2</sup> determined at the closest point (11°3.0'N, 142°28.0'W) from the global heat flow data set (Pollack et al., 1993).

### Natural Gamma Radiation

Natural gamma radiation was measured on all whole cores in Hole 1220A (Fig. F32). The highest natural gamma radiation values are present in the clay-rich lithologic Unit I and average 13.1 counts per second (cps). NGR maxima in Unit I at 8.3 mbsf (15.0 cps) and between 13.7 and 16.3 mbsf (18.0 cps) correlate with similar increases in GRA bulk density (Fig. F23). The higher values between 13.7 and 16.3 mbsf also correlate with a substantial increase in MS (Fig. F33) and high concentrations of phillipsite (K-Ca zeolite) (see “Unit I,” p. 6, in “Lithostratigraphy”). Below Unit I, NGR values decrease to near background levels. Values recorded in Units II, III, and IV average 2.0, 1.2, and 1.0 cps, respectively.

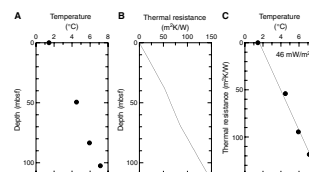
### MS

Whole-core MS measurements were made on all cores from Site 1220. MS in the clay-rich lithologic Unit I increases downhole from ~30 × 10<sup>-6</sup> SI to values as high as 145 × 10<sup>-6</sup> SI at 16 mbsf (Fig. F33). This susceptibility maximum correlates with a small increase in GRA bulk density, an increase in NGR, and increased concentrations of Al and Fe (see “Solid-Phase Geochemistry,” p. 22, in “Geochemistry”).

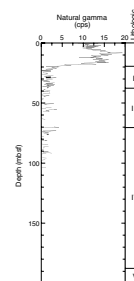
Below 19.5 mbsf, susceptibility does not reflect major changes in lithology as well as at other Leg 199 sites. MS in the radiolarian-rich Unit II averages 25 × 10<sup>-6</sup> SI, with the lowest values corresponding to a layer of nanofossil ooze at ~23 mbsf. The calcite-rich nanofossil ooze of Unit III displays a small decrease in susceptibility to an average of 15 × 10<sup>-6</sup> SI. The upper part of Unit III (38–58 mbsf) contains several peaks in susceptibility that correlate with higher concentrations of clay in this interval (see “Unit III,” p. 7, in “Lithostratigraphy”). Between 58 and 69 mbsf, the sediment contains a higher concentration of nanofossils and displays more uniformly low susceptibility (~10 × 10<sup>-6</sup> SI).

T20. In situ temperature, p. 92.

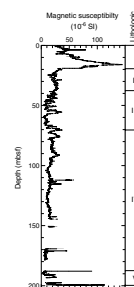
F31. Heat flow calculation, p. 65.



F32. Natural gamma radiation, p. 66.



F33. Magnetic susceptibility, p. 67.



The radiolarian-rich lithologic Unit IV has slightly higher MS values than the surrounding lithology (average =  $17 \times 10^{-6}$  SI). Low susceptibility ( $\sim 10 \times 10^{-6}$  SI) at 104 mbsf correlates with the lowest grain density values in the radiolarian ooze (Fig. F23) and a local maximum in LAS opal concentration (Fig. F26). Below 145 mbsf, the susceptibility data are limited by poor core recovery; however, the P/E boundary section, Section 199-1220B-20X-2, was well documented by the MS detector (Fig. F24). The transition from nannofossil chalk to the metal oxide-rich clay is marked by an increase from  $\sim 25$  to  $113 \times 10^{-6}$  SI at 199.38 mbsf. This difference is comparable to the change at the boundary between the clay of Unit I and the radiolarian ooze of Unit II but occurs over a much narrower interval. Below 199.38 mbsf, susceptibility decreases to a minimum of  $45 \times 10^{-6}$  SI, coinciding with the reddish layer. The small spike to a low MS value at 199.53 mbsf is suspected to be an anomalous point. A second, broad peak of  $88 \times 10^{-6}$  SI at 199.70 mbsf lies just above the P/E boundary (Fig. F24). The changes in susceptibility correlate well with zones of metal enrichment in the multicolored clay (see “P/E Boundary,” p. 23, in “Geochemistry”). Below the boundary, the susceptibility of the nannofossil chalk returns to  $25 \times 10^{-6}$  SI.

## REFERENCES

- Aubry, M.-P., 1996. Towards an upper Paleocene-lower Eocene high resolution stratigraphy based on calcareous nannofossil stratigraphy. *Israel J. Earth Sci.*, 44:239–253.
- Berggren, W.A., Kent, D.V., Swisher, C.C., III, and Aubry, M.-P., 1995. A revised Cenozoic geochronology and chronostratigraphy. In Berggren, W.A., Kent, D.V., Aubry, M.-P., and Hardenbol, J. (Eds.), *Geochronology, Time Scales and Global Stratigraphic Correlation*. Spec. Publ.—Soc. Econ. Paleontol. Mineral., 54:129–212.
- Bybell, L.M., and Self-Trail, J.M., 1995. Evolutionary, biostratigraphic, and taxonomic study of calcareous nannofossils from a continuous Paleocene/Eocene boundary section in New Jersey. *Geol. Surv. Prof. Pap. U.S.*, 1554.
- , 1997. Late Paleocene and early Eocene calcareous nannofossils from three boreholes in an onshore-offshore transect from New Jersey to the Atlantic continental rise. In Miller, K.G., and Snyder, S.W. (Eds.), *Proc. ODP, Sci. Results*, 150X: College Station, TX (Ocean Drilling Program), 91–110.
- Cande, S.C., LaBrecque, J.L., Larson, R.L., Pitmann, W.C., III, Golovchenko, X., and Haxby, W.F., 1989. *Magnetic Lineations of the World's Ocean Basins*. AAPG Map Ser., 13.
- Coxall, H. K., Huber, B.T., and Pearson, P.N., in press. Origin and morphology of the Eocene planktonic foraminifera *Hantkenina*. *J. Foraminiferal Res.*
- De Klasz I., and De Klasz, S., 1986. Description d'une nouvelle espèce de Foraminifère planctonique (*Clavatorella paleocenica* n.sp.) du Danien du Sénégal: des Seances de l'Academie des Sciences, Serie 2: Mecanique-Physique, Chimie. Sciences de l'Univers, *Sci. Terre*, 302:687–690.
- De Klasz, I., De Klasz, S., and Ausseil-Badie, J., 1988. Etude systématique des foraminifères du Danien de la Formation des Madeleines de Dakar (Sénégal). *Cah. Micropaleontol.*, 1987:29–112.
- Engelbreton, D.C., Cox, A., and Gordon, R.G., 1985. *Relative Motions Between Oceanic and Continental Plates in the Pacific Basin*. Spec. Pap.—Geol. Soc. Am., 206.
- Gripp, A.E., and Gordon, R.G., 1990. Current plate velocities relative to the hotspots incorporating the NUVEL-1 global plate motion model. *Geophys. Res. Lett.*, 17:1109–1112.
- Hagelberg, T., Shackleton, N., Pisias, N., and Shipboard Scientific Party, 1992. Development of composite depth sections for Sites 844 through 854. In Mayer, L., Pisias, N., Janecek, T., et al., *Proc. ODP, Init. Repts.*, 138 (Pt. 1): College Station, TX (Ocean Drilling Program), 79–85.
- Kelly, D.C., Bralower, T.J., and Zachos, J.C., 1998. Evolutionary consequences of the latest Paleocene thermal maximum for tropical planktonic foraminifera. *Palaeogeogr., Palaeoclimatol., Palaeoecol.*, 141:139–161.
- Kelly, D.C., Bralower, T.J., Zachos, J.C., Premoli Silva, I., and Thomas, E., 1996. Rapid diversification of planktonic foraminifera in the tropical Pacific (ODP Site 865) during the late Paleocene thermal maximum. *Geology*, 24:423–426.
- Lyle, M., 2000. Data submission to ODP Pollution Prevention and Safety Panel: proposed drill sites for ODP Leg 198—a Paleogene equatorial APC transect. *BSU-CGISS Tech Rept.*, 2000-03.
- Monechi, S., 1985. Campanian to Pleistocene calcareous nannofossil stratigraphy from the northwest Pacific Ocean, Deep Sea Drilling Project Leg 86. In Heath, G.R., Burckle, L.H., et al., *Init. Repts. DSDP*, 86: Washington (U.S. Govt. Printing Office), 301–336.
- Norris, R.D., and Röhl, U., 1999. Carbon cycling and chronology of climate warming during the Palaeocene/Eocene transition. *Nature*, 401:775–778.
- Perch-Nielsen, K., 1981. Nouvelles observations sur les nannofossiles calcaires à la limite Crétacé-Tertiaire près de El Kef (Tunisie). *Cah. Micropaleont.*, 3:25–36.

- Pollack, H.N., Hurtes, S.J., and Johnson, J.R., 1993. Heat flow from the earth's interior: analysis of the global data set. *Rev. Geophys.*, 31:267–281.
- Pribnow, D.F.C., Kinoshita, M., and Stein, C.A., 2000. Thermal data collection and heat flow recalculations for ODP Legs 101–180. Institute for Joint Geoscientific Research, GGA, Hanover, Germany, 0120432. Available from World Wide Web: <<http://www-odp.tamu.edu/publications/heatflow/>>. [Cited 2001-11-22]
- Romein, A.J.T., 1977. Calcareous nannofossils from the Cretaceous/Tertiary boundary interval in the Barranco del Gredero (Caravaca, Prov. Murcia, S. E. Spain), I and II. *Proc. K. Ned. Akad. Wet., Ser. B*, 80:256–279.
- Romein, A.J.T., 1979. Lineages in early Paleogene calcareous nannoplankton. *Utrecht Micropaleontol. Bull.*, 22:1–231.
- Thierstein, H.R., and Okada, H., 1979. The Cretaceous/Tertiary boundary event in the North Atlantic. In Tucholke, B.E., Vogt, P.R., et al., *Init. Repts. DSDP*, 43: Washington (U.S. Govt. Printing Office), 601–616.
- van Andel, T.H., Heath, G.R., and Moore, T.C., Jr., 1975. Cenozoic history and paleoceanography of the central equatorial Pacific Ocean: a regional synthesis of Deep Sea Drilling Project data. *Mem.—Geol. Soc. Am.*, 143.



**Figure F2.** Seismic reflection profile at Site 1220 (PAT-9D). The sedimentary section is marked by a weakly reflective unit ~37 ms two-way traveltime (TWT) below the seafloor, assumed to be clays. Deeper in the section, reflectors at approximately 53, 97, 193, and 283 ms TWT are interpreted as the P4, P3, P2 and basement seismic horizons, respectively (see [Lyle et al.](#), this volume).

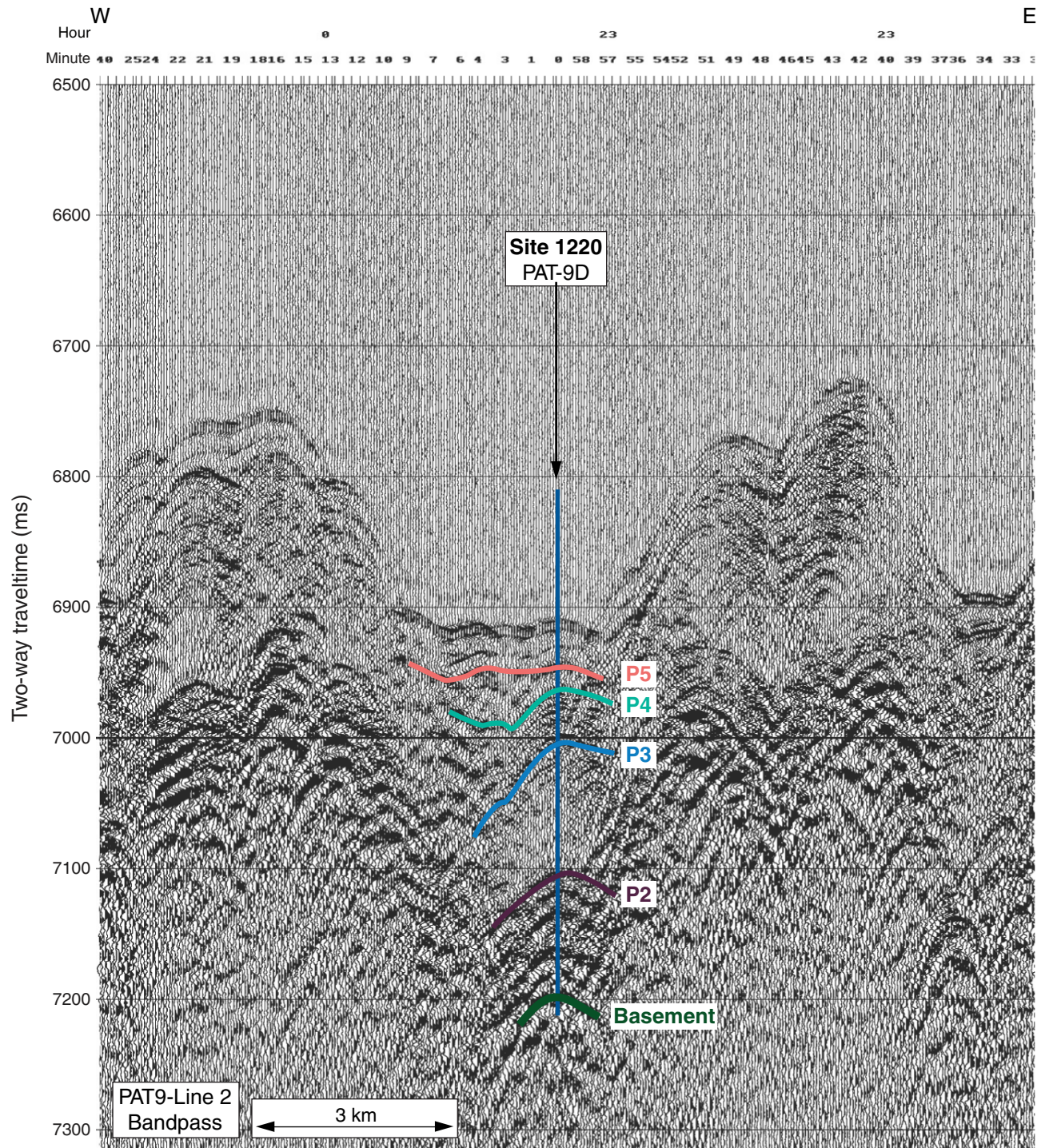
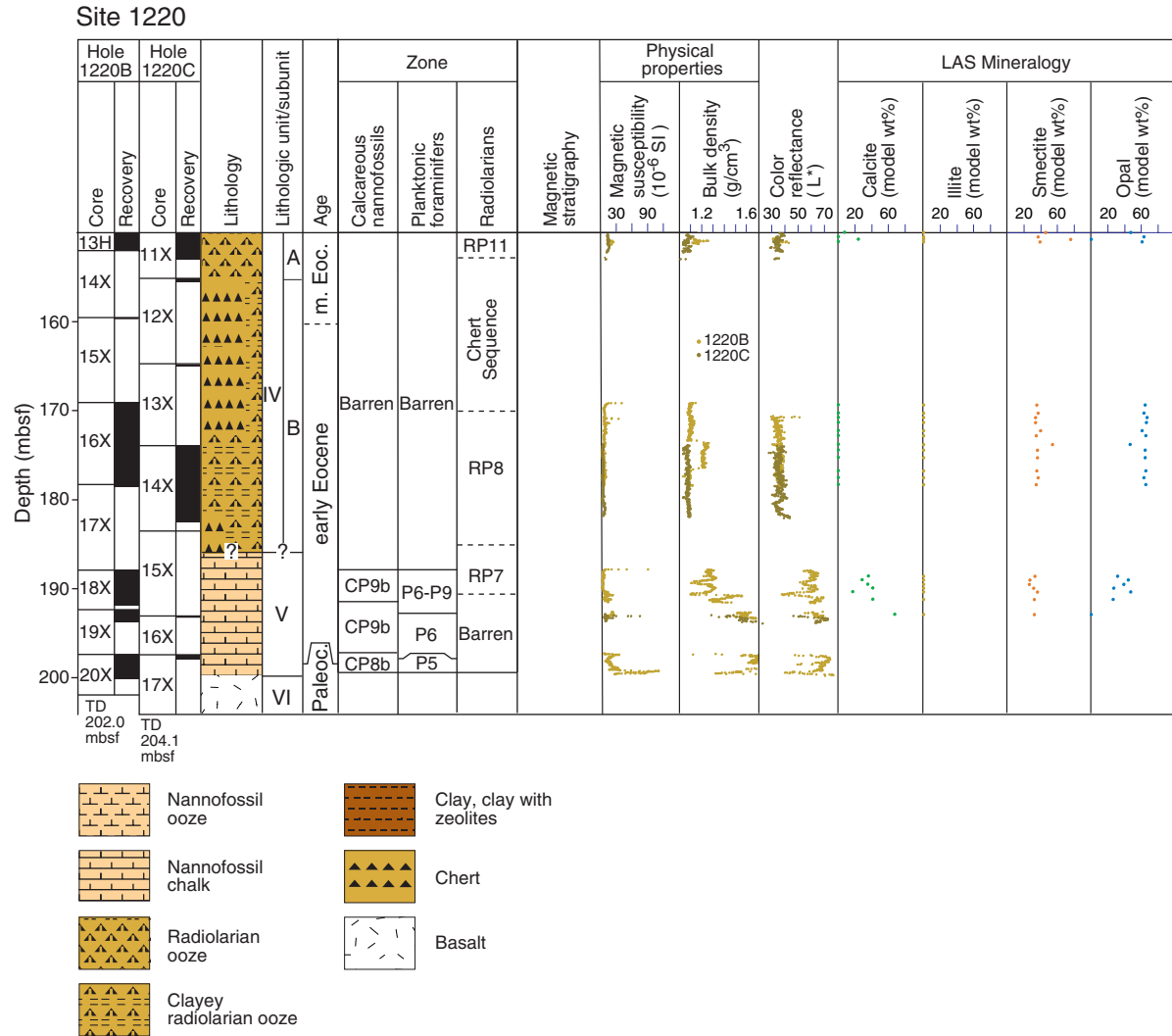




Figure F3 (continued).



**Figure F4.** Close-up composite digital photograph of interval 199-1220B-20X-2, 40–80 cm, showing the P/E boundary sequence. Photomicrographs of sediment at selected intervals shown on right. Lithologic and color variations are also noted. Cal. = calcareous.

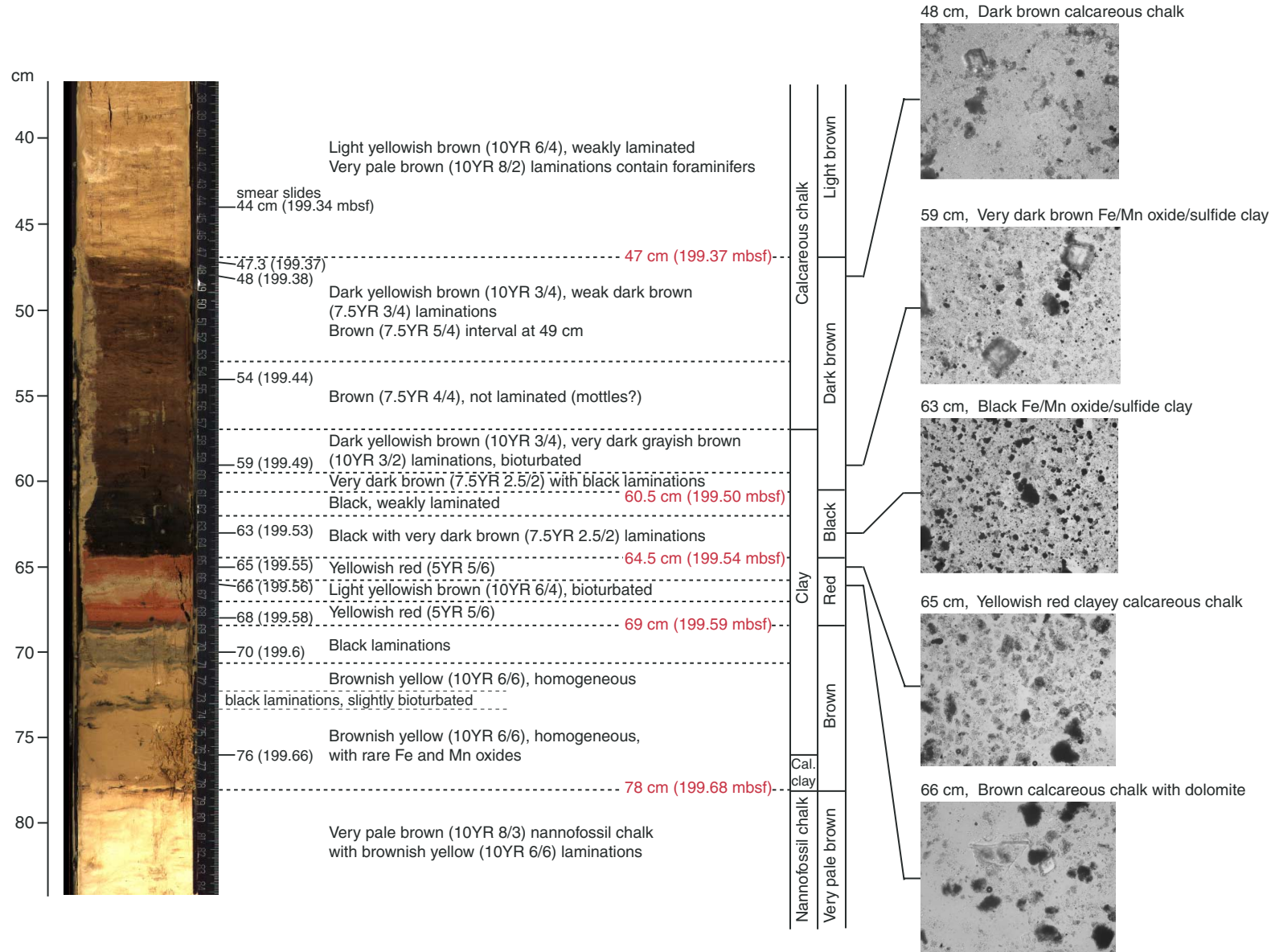


Figure F5. Close-up composite digital photograph of interval 199-1220B-20X-2, 0–91 cm, showing the P/E boundary sequence. Also shown are major and minor sediment components based on smear slide observations. Calc. = calcareous.

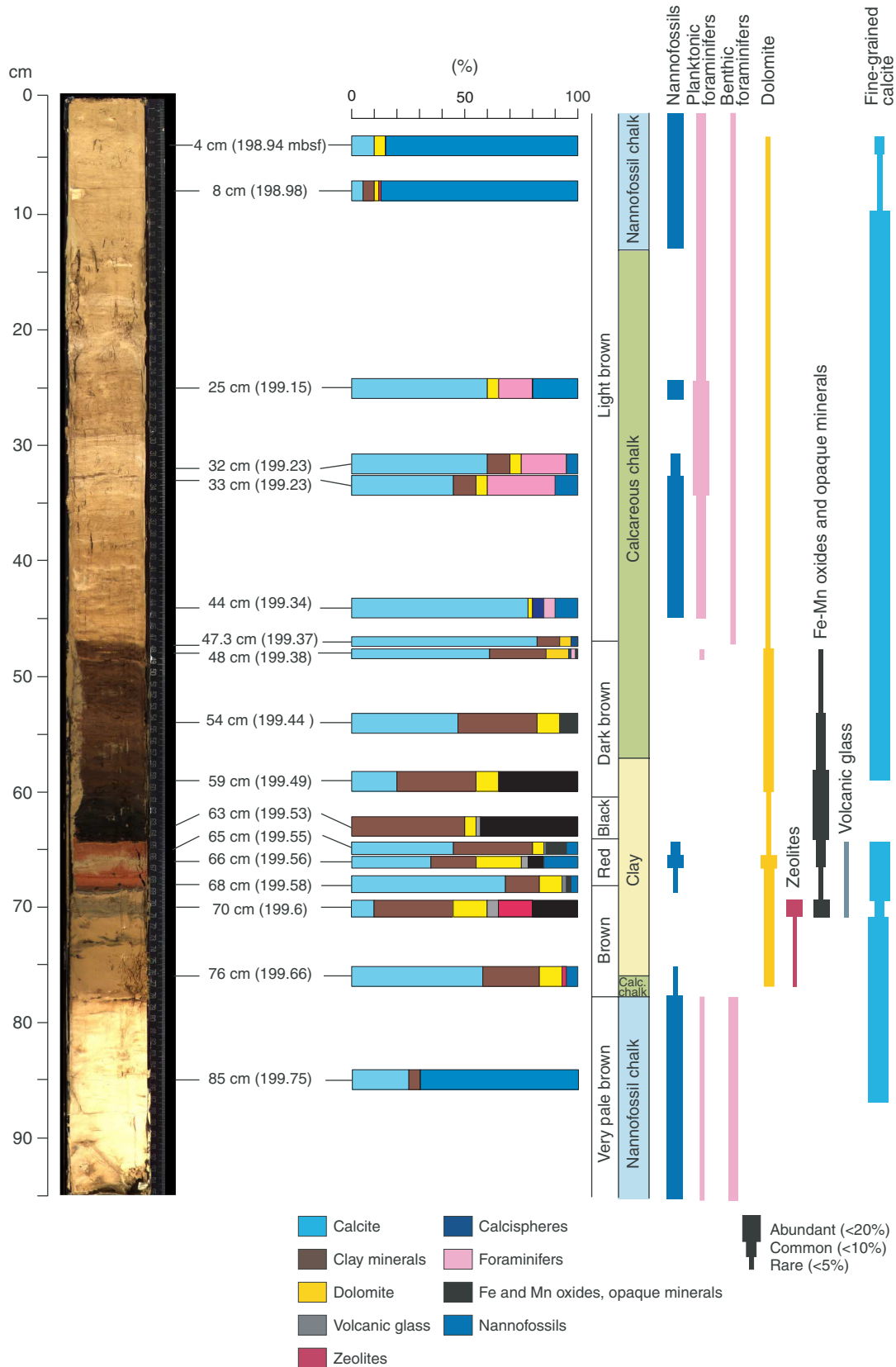
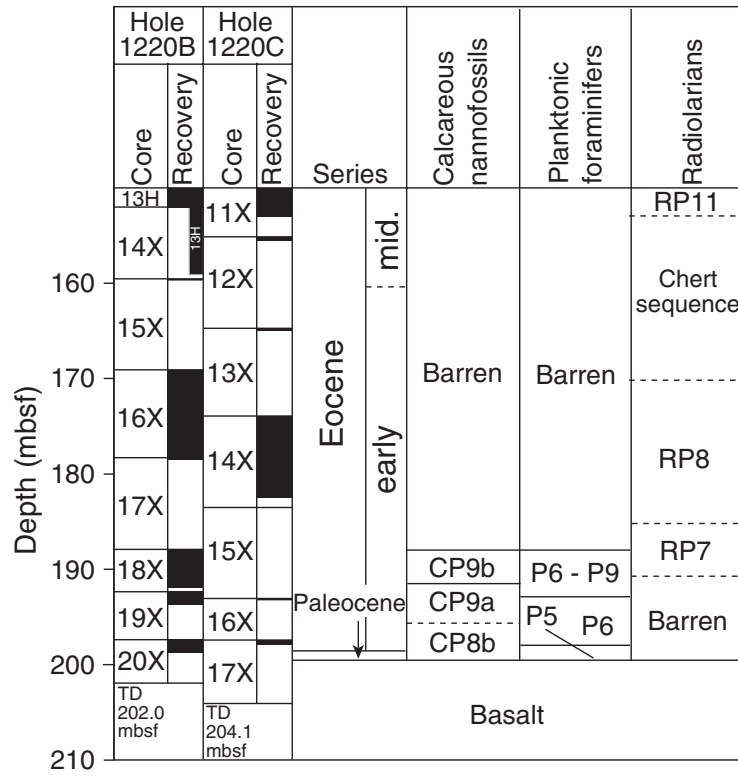




Figure F6 (continued).



**Figure F7.** Close-up composite digital photographs of the >63- $\mu\text{m}$  fraction of washed sample from across the P/E boundary. The following major grains are observed at each depth interval: planktonic foraminifers (intervals 199-1220B-20X-2, 13–20, 28–35, 35–43, and 42–50 cm; 198.90–199.40 mbsf), pink-brown grains and dolomite crystals (interval 199-1220B-20X-2, 50–57 cm; 199.40–199.47 mbsf), black grains and sediment lumps (interval 199-1220B-20X-2, 57–64.5 cm; 199.47–199.55 mbsf), large pinkish grains with many dolomite crystals (interval 199-1220B-20X-2, 65–72 cm; 199.55–199.62 mbsf), small pink-brown grains with rare planktonic foraminifers and dolomite grains (interval 199-1220B-20X-2, 74–78 cm; 199.64–199.68 mbsf), dolomite grains and rare benthic foraminifers (intervals 199-1220B-20X-2, 77.5–85 cm, and 85–95 cm; 199.68–199.85 mbsf).

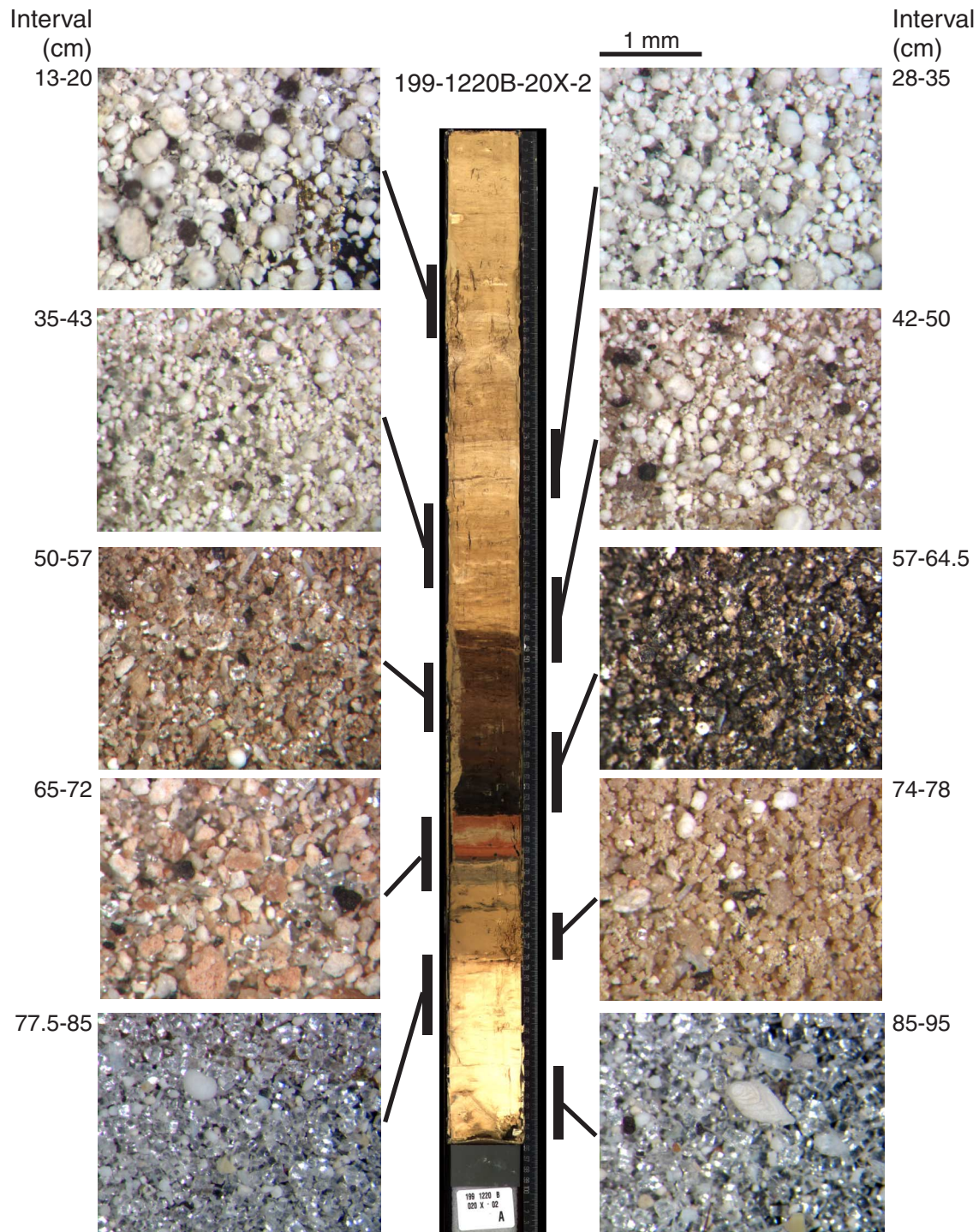


Figure F8. Stratigraphic distribution of benthic foraminifers in Section 199-1220B-20X-2 (198.90–199.85 mbsf). The P/E boundary as represented by the Benthic Extinction Event (BEE) is marked by two red triangles at 199.68 mbsf.

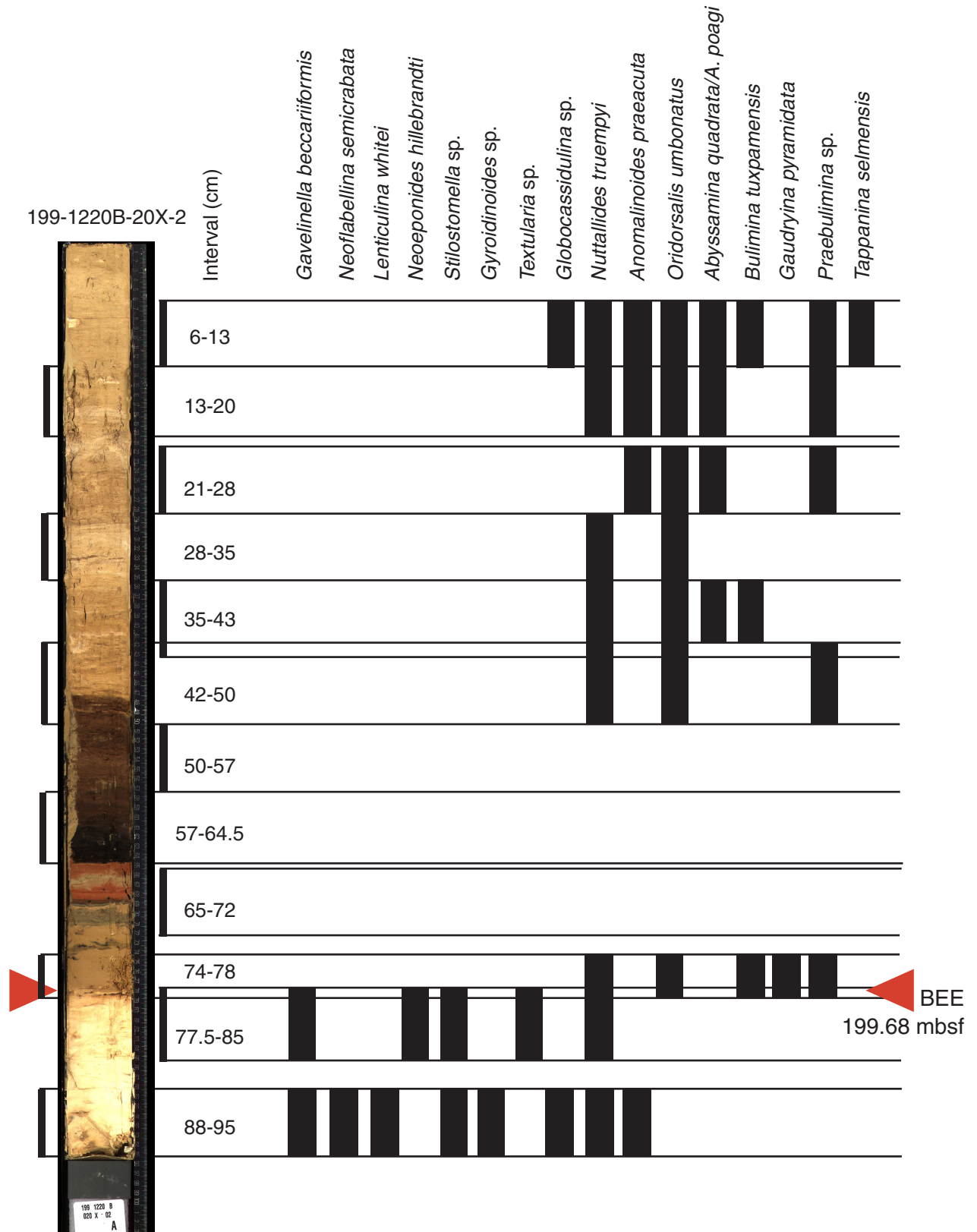


Figure F9. Archive-half magnetization intensities after AF demagnetization at a peak field of 20 mT from Holes 1220A, 1220B, and 1220C.

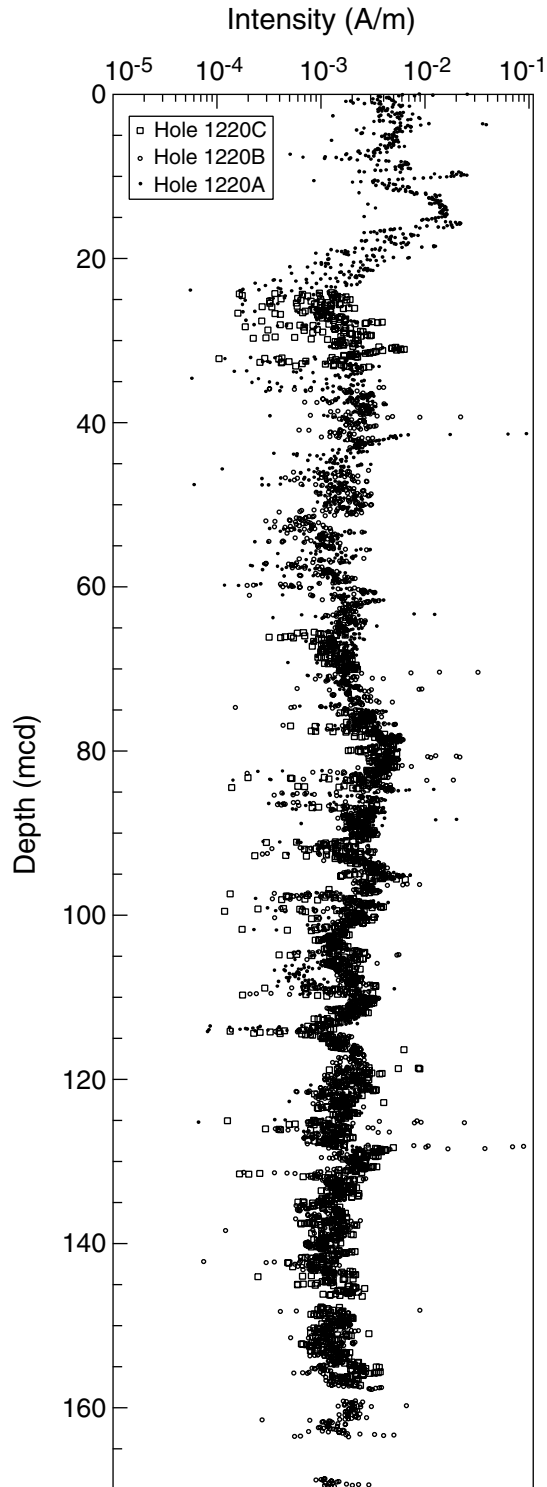


Figure F10. Composite magnetic stratigraphy at Site 1220. Virtual geomagnetic pole (VGP) latitudes were obtained after partial AF demagnetization of continuous measurements at a peak field of 20 mT. Polarity column shows interpreted zones of normal (black) and reversed (white) magnetization. A. Early Miocene–late middle Eocene, top 100 m. (Continued on next page.)

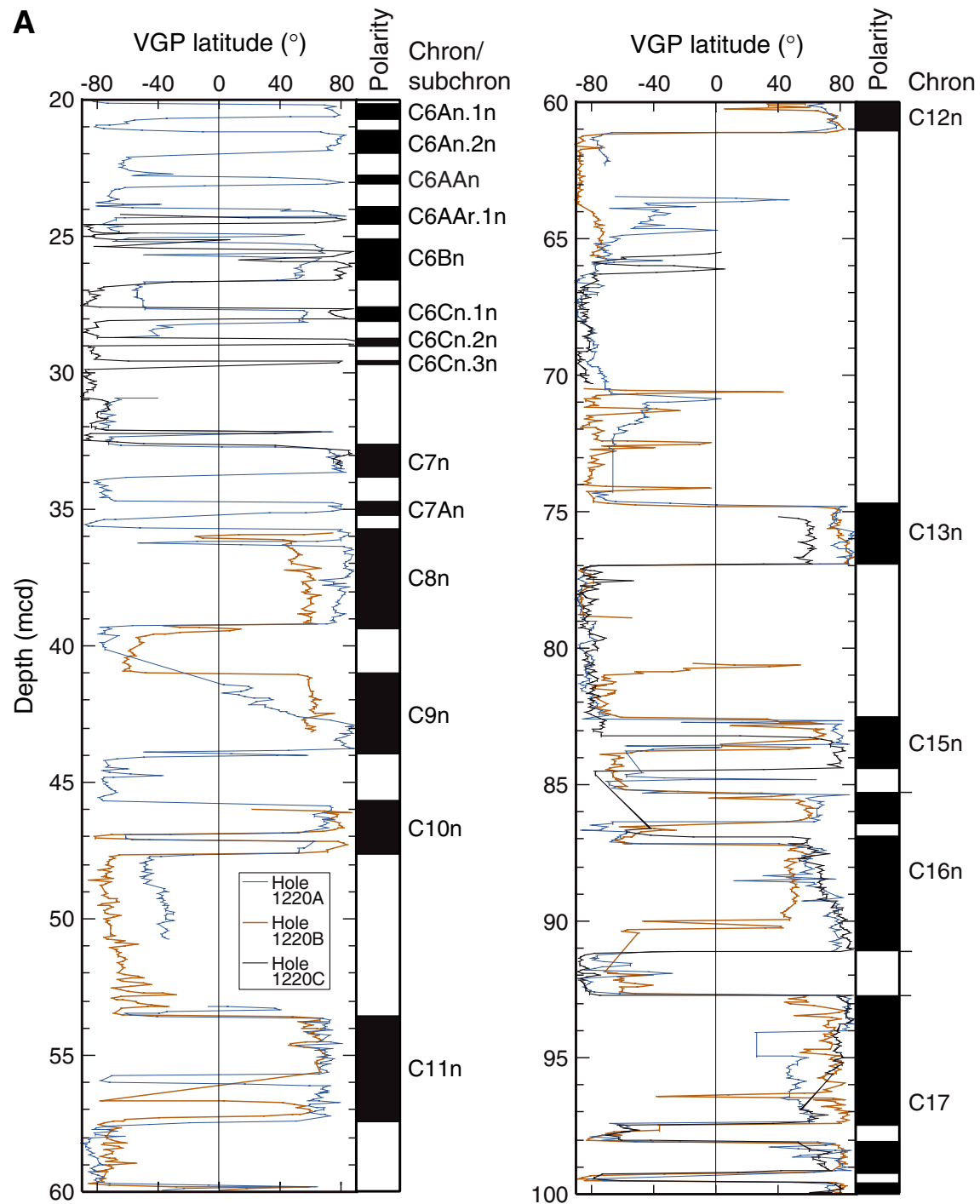
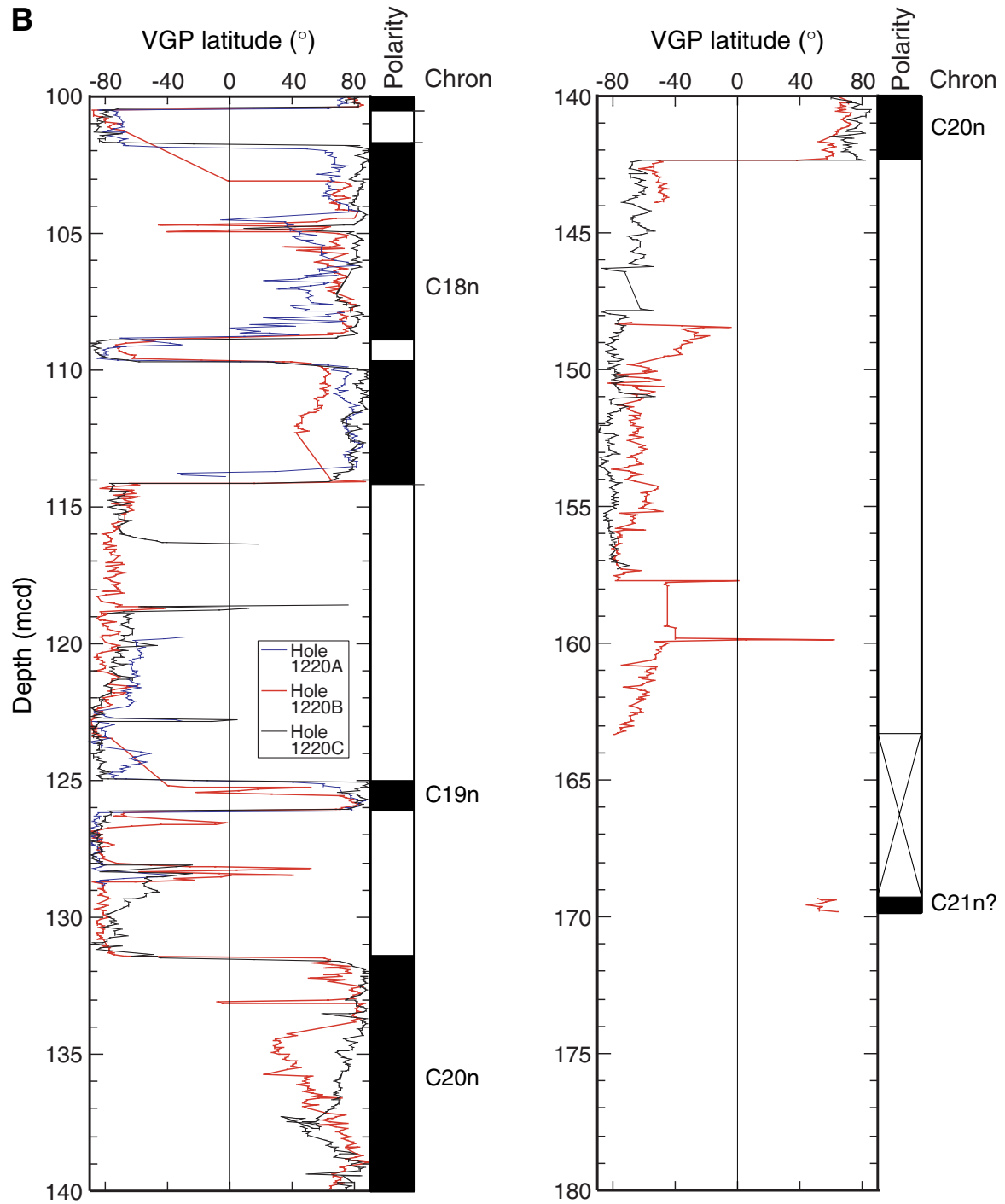


Figure F10 (continued). B. Early–middle Eocene, bottom 80 m.



**Figure F11.** Gamma ray attenuation (GRA) bulk density data for Holes 1220A (black curve), 1220B (blue curve), and 1220C (green curve) plotted vs. composite depth. The data from Holes 1220B and 1220C are offset from Hole 1220A by constants for illustration purposes. All data sets are smoothed with a nine-point Gaussian filter. Intervals with obvious flow-in or drilling disturbance are removed from the data sets (see Table T7, p. 76).

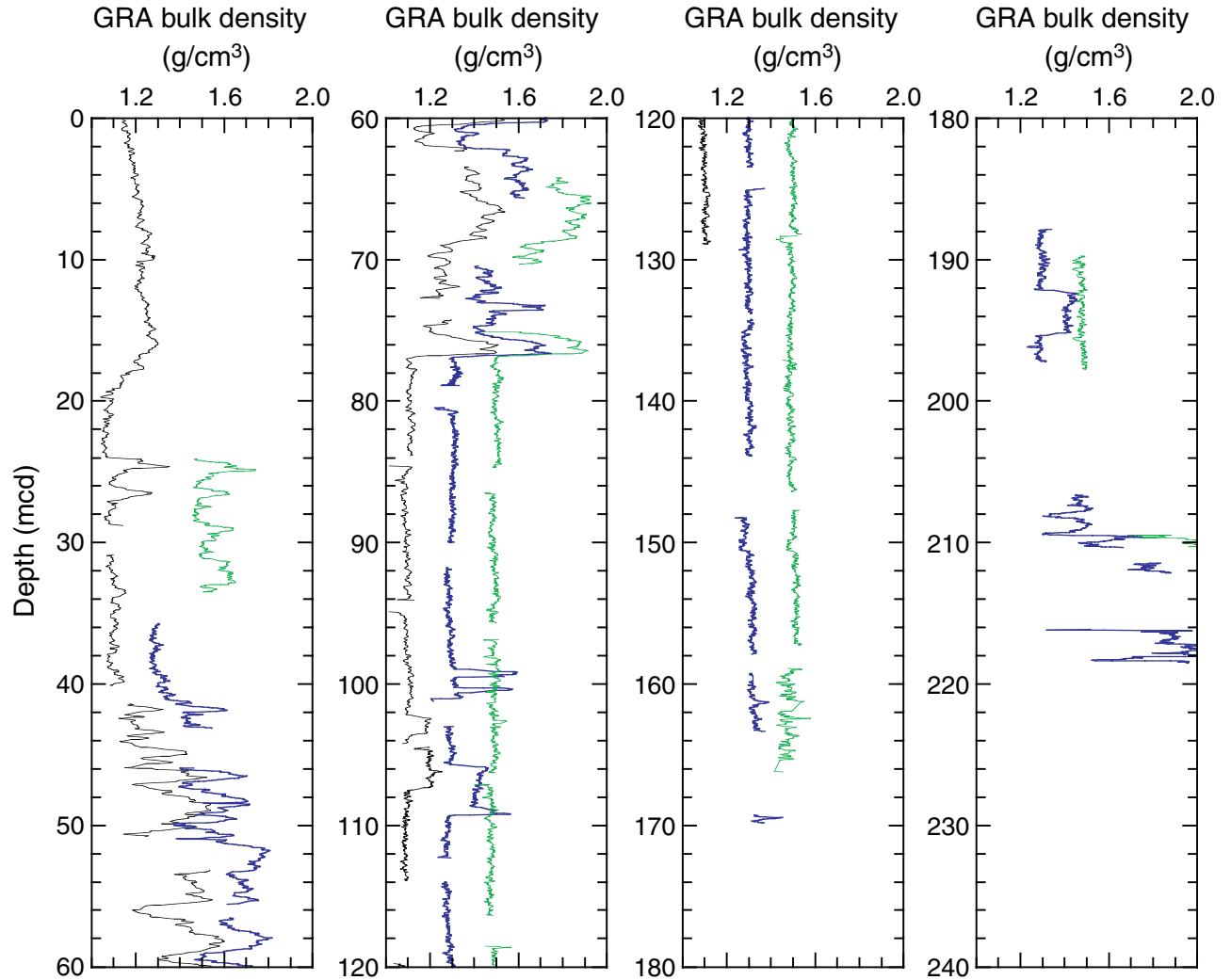


Figure F12. Magnetic susceptibility data for Holes 1220A (black curve), 1220B (blue curve), and 1220C (green curve) plotted vs. composite depth. The data from Holes 1220B and 1220C are offset from Hole 1220A by constants for illustration purposes. All data sets are smoothed with a nine-point Gaussian filter. Intervals with obvious flow-in or drilling disturbance are removed from the data sets (see Table T7, p. 76). Note scale change for the interval from 0–60 mcd.

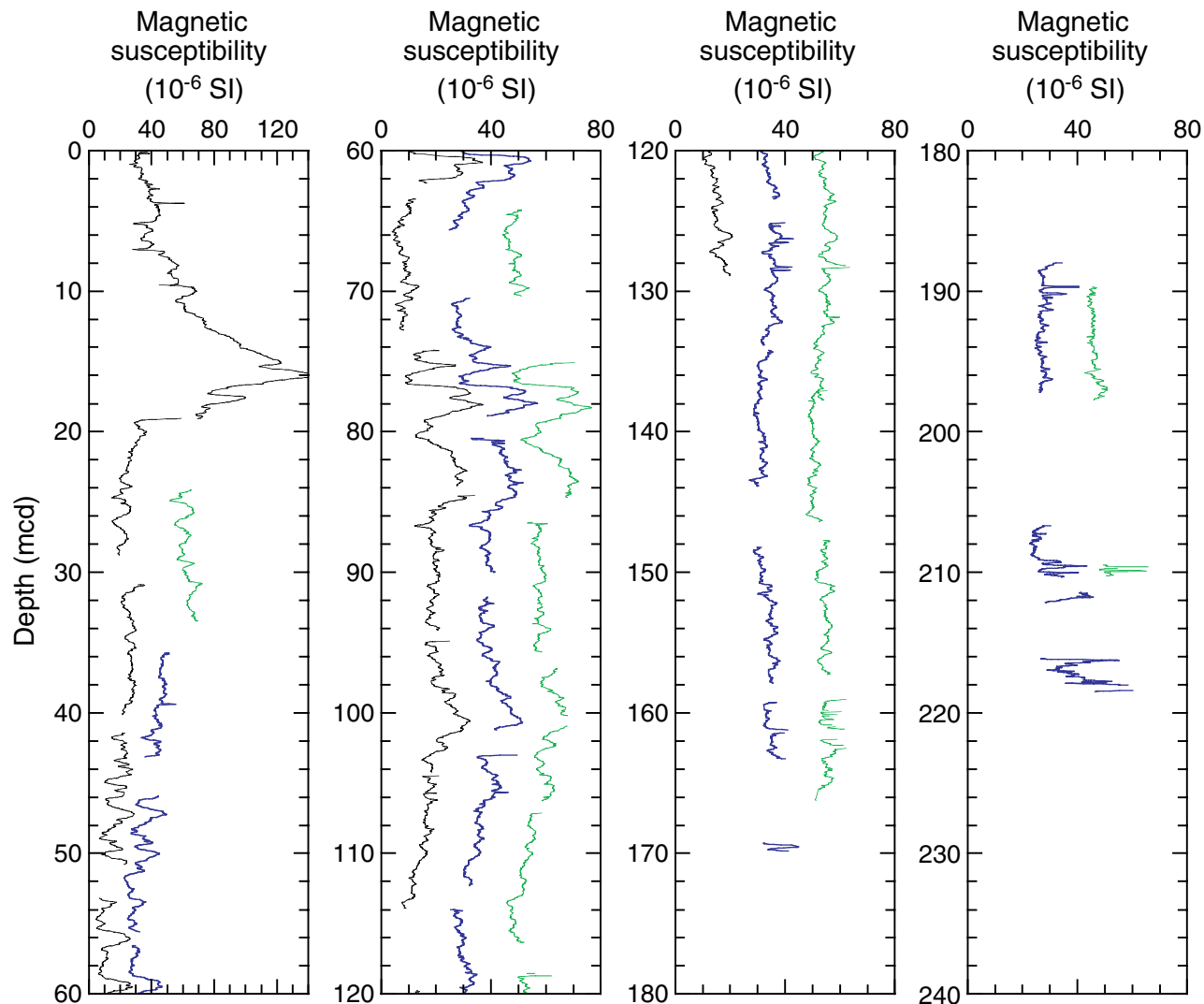


Figure F13. Spliced records of gamma ray attenuation (GRA) bulk density, magnetic susceptibility, and the color reflectance parameter ( $L^*$ ) shown for the composite section of Site 1220. Lithology changes are clearly visible. High GRA density values centered on 100, 110, and 195 mcd are instrumental artifacts.

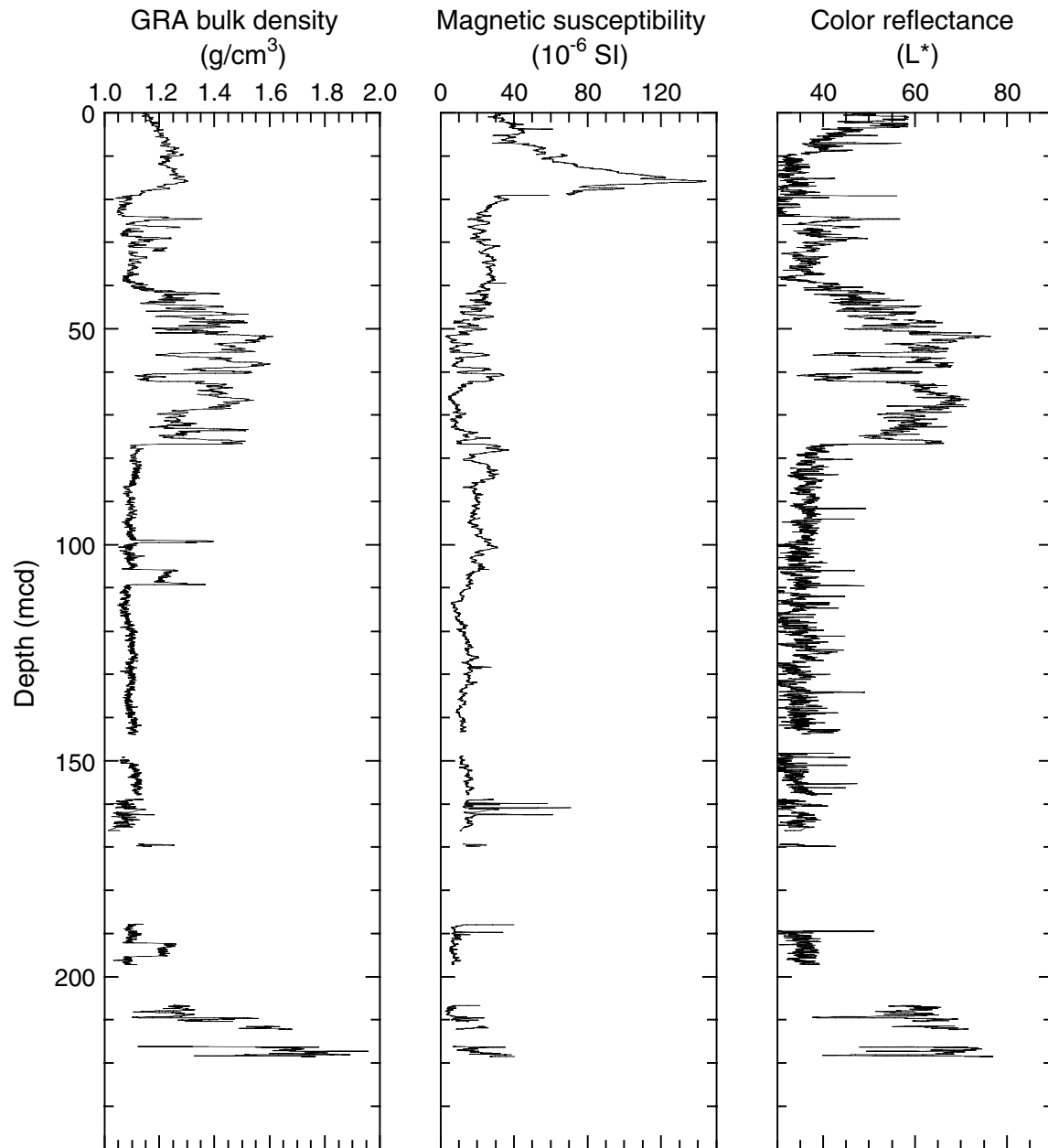


Figure F14. Spliced records of gamma ray attenuation (GRA) bulk density (blue curve in each panel) and magnetic susceptibility for Site 1220. Note variable GRA bulk density and magnetic susceptibility scales from panel to panel.

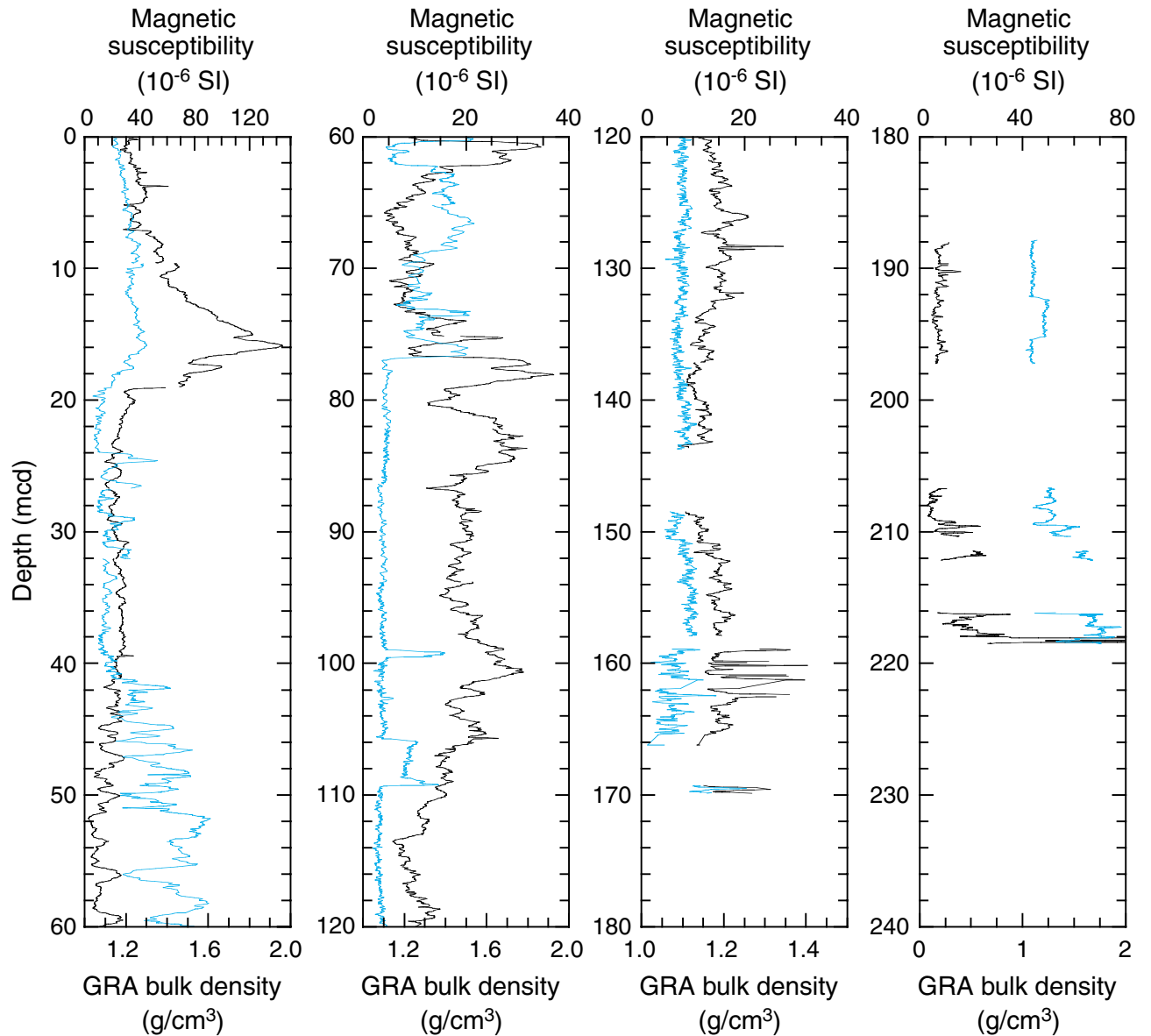


Figure F15. LSRs and chronostratigraphic markers for Site 1220.

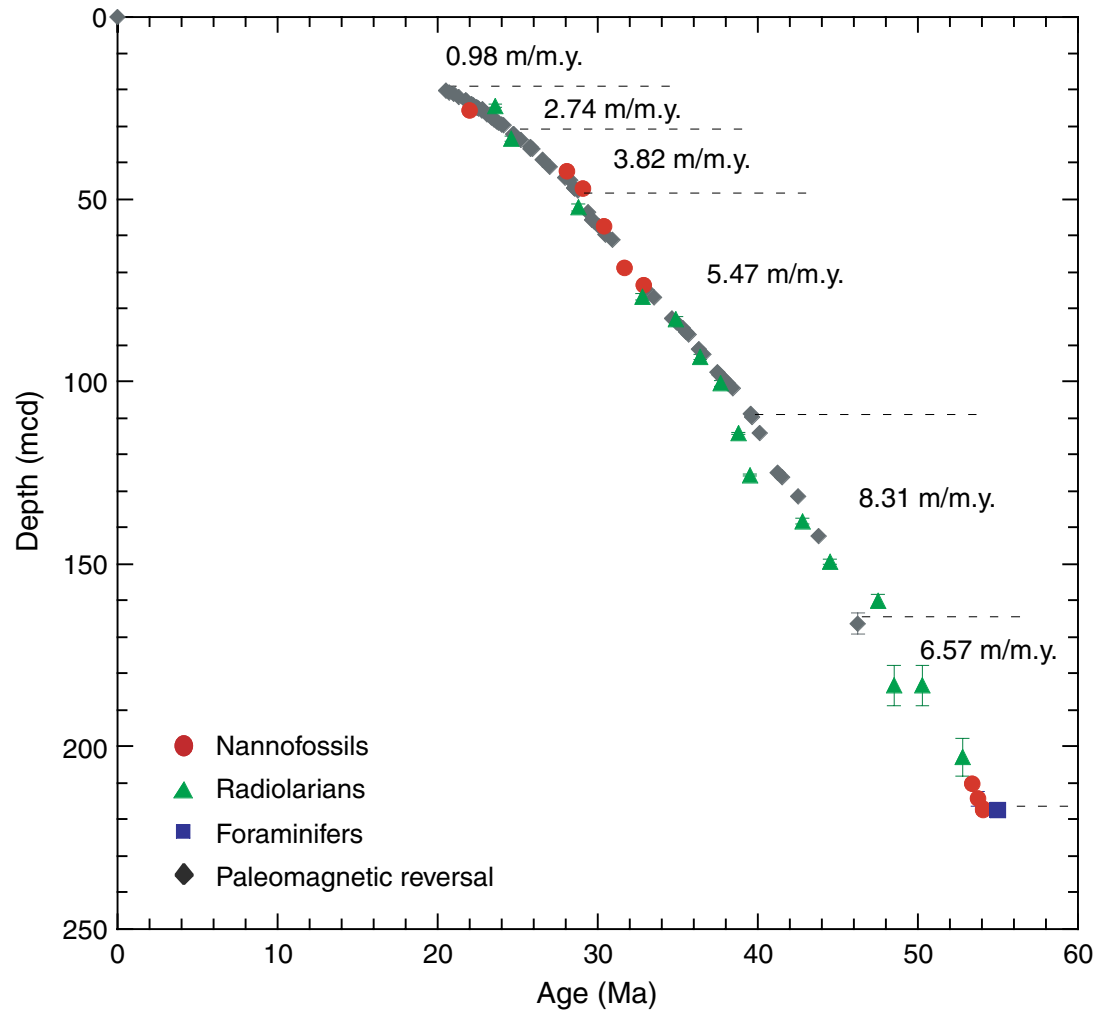


Figure F16. Density record of site survey piston Core EW9709-13P (Lyle, 2000) compared to density record of Hole 1220A. Shaded area = the portion of the record in which the piston core rates appear to be higher than those from Hole 1220A.

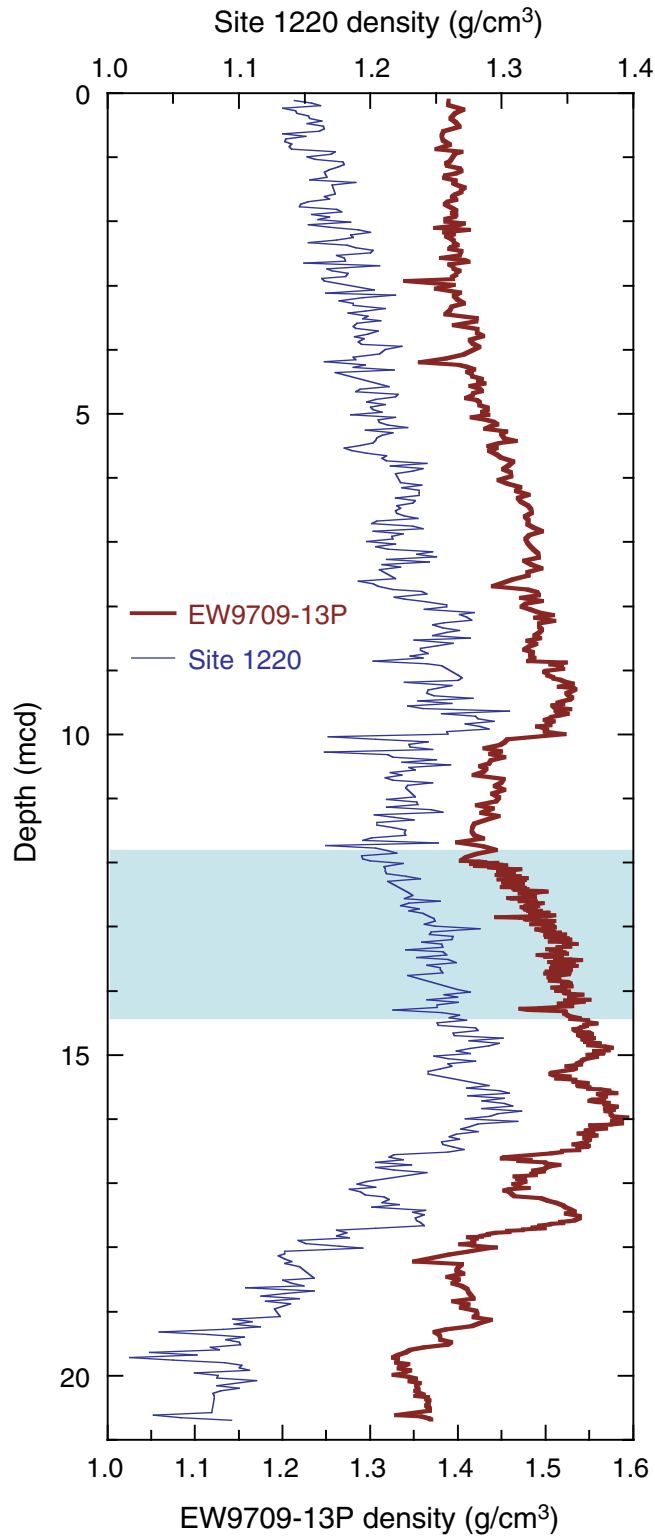


Figure F17. Age vs. depth plots for the upper part of Site 1220 and for site survey Core EW9709-13P (Lyle, 2000).

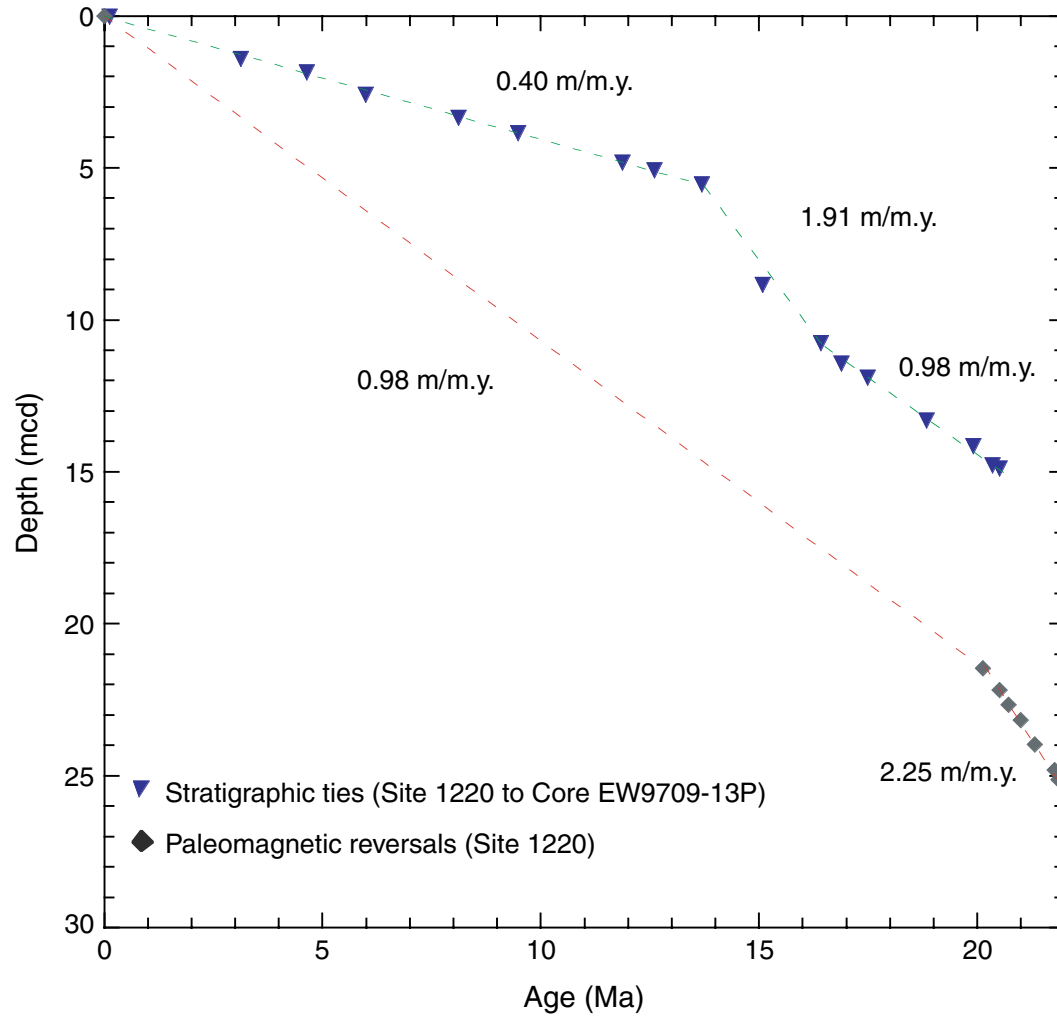


Figure F18. Mass accumulation rates (MARs) of sediments at Site 1220.

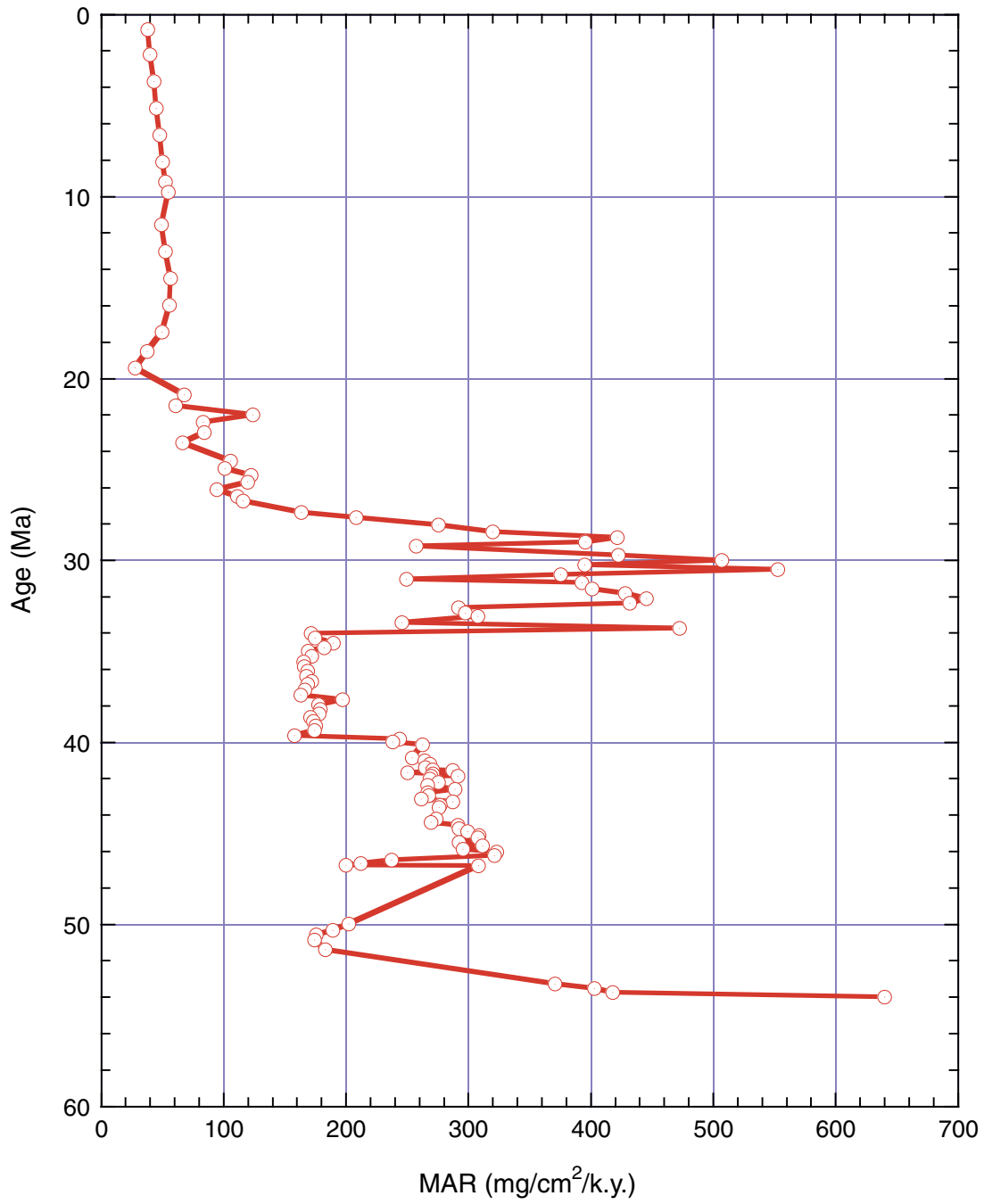


Figure F19. Interstitial water data from Site 1220. Solid circles = Ca, crosses = Mg.

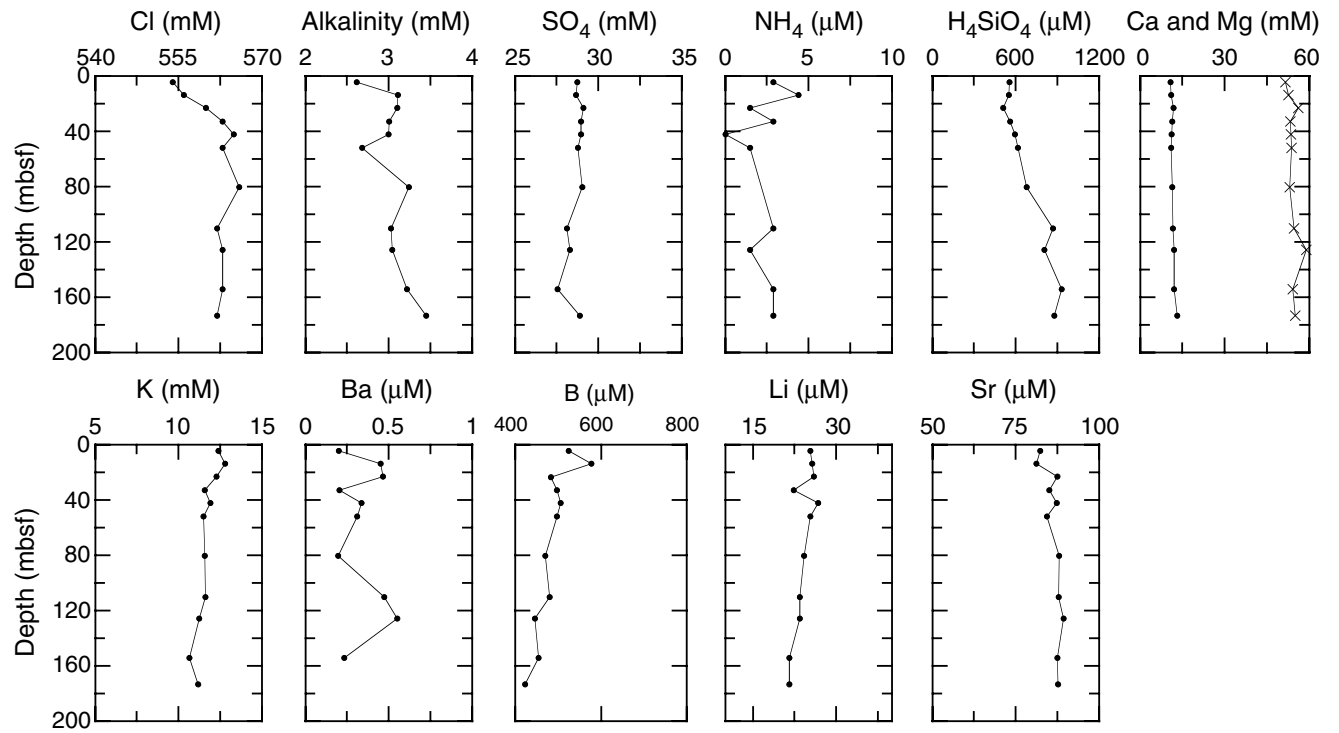


Figure F20. Bulk-sediment data from Site 1220. Ca values higher than 35.9 wt% are out of the range of the standards (see "Geochemistry," p. 20, in the "Explanatory Notes" chapter).

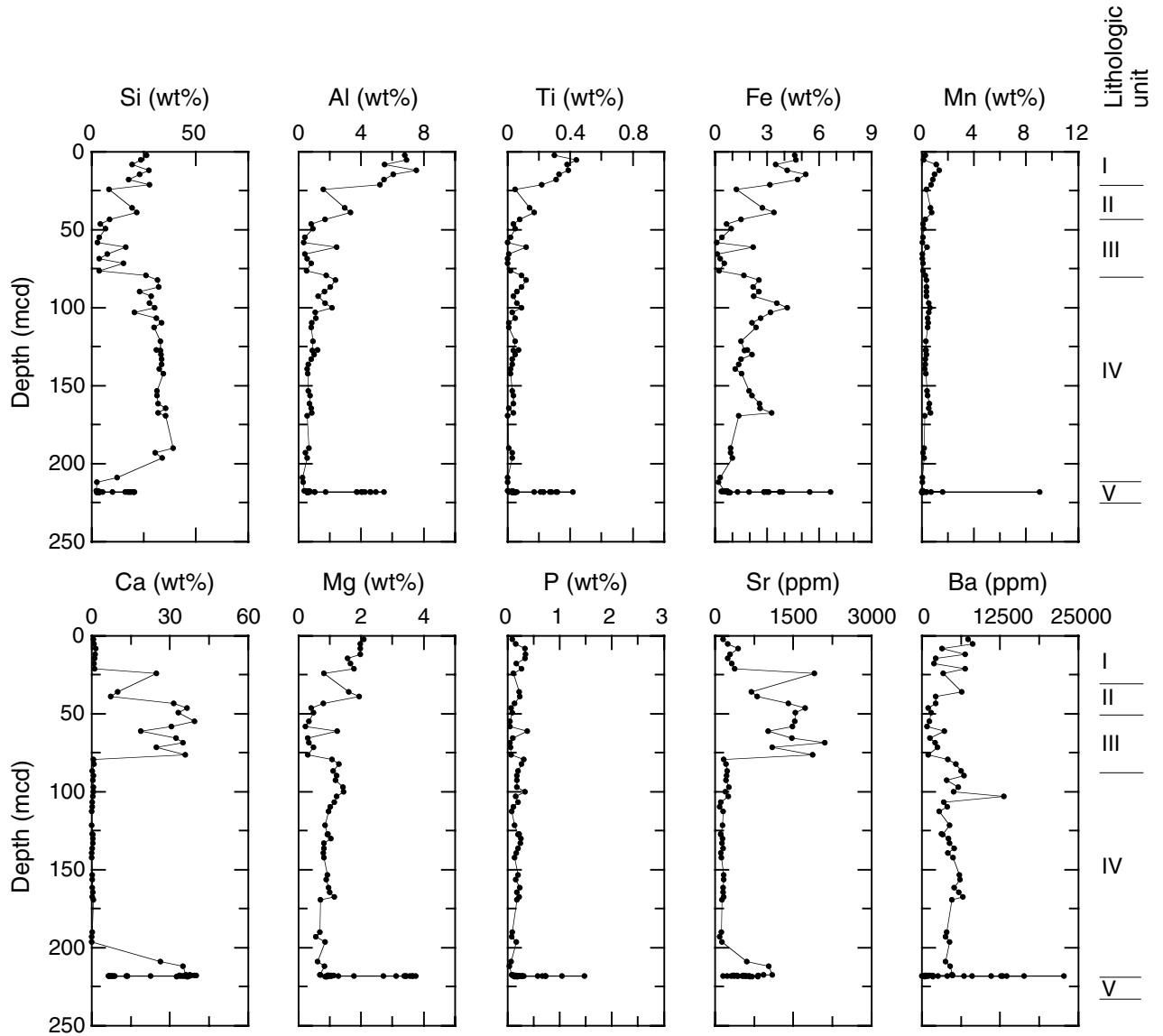


Figure F21.  $\text{CaCO}_3$  and Ca data from Site 1220.  $\text{CaCO}_3$  values higher than 90 wt% are calculated from Ca values out of the range of the standards (see "Geochemistry," p. 20, in the "Explanatory Notes" chapter).

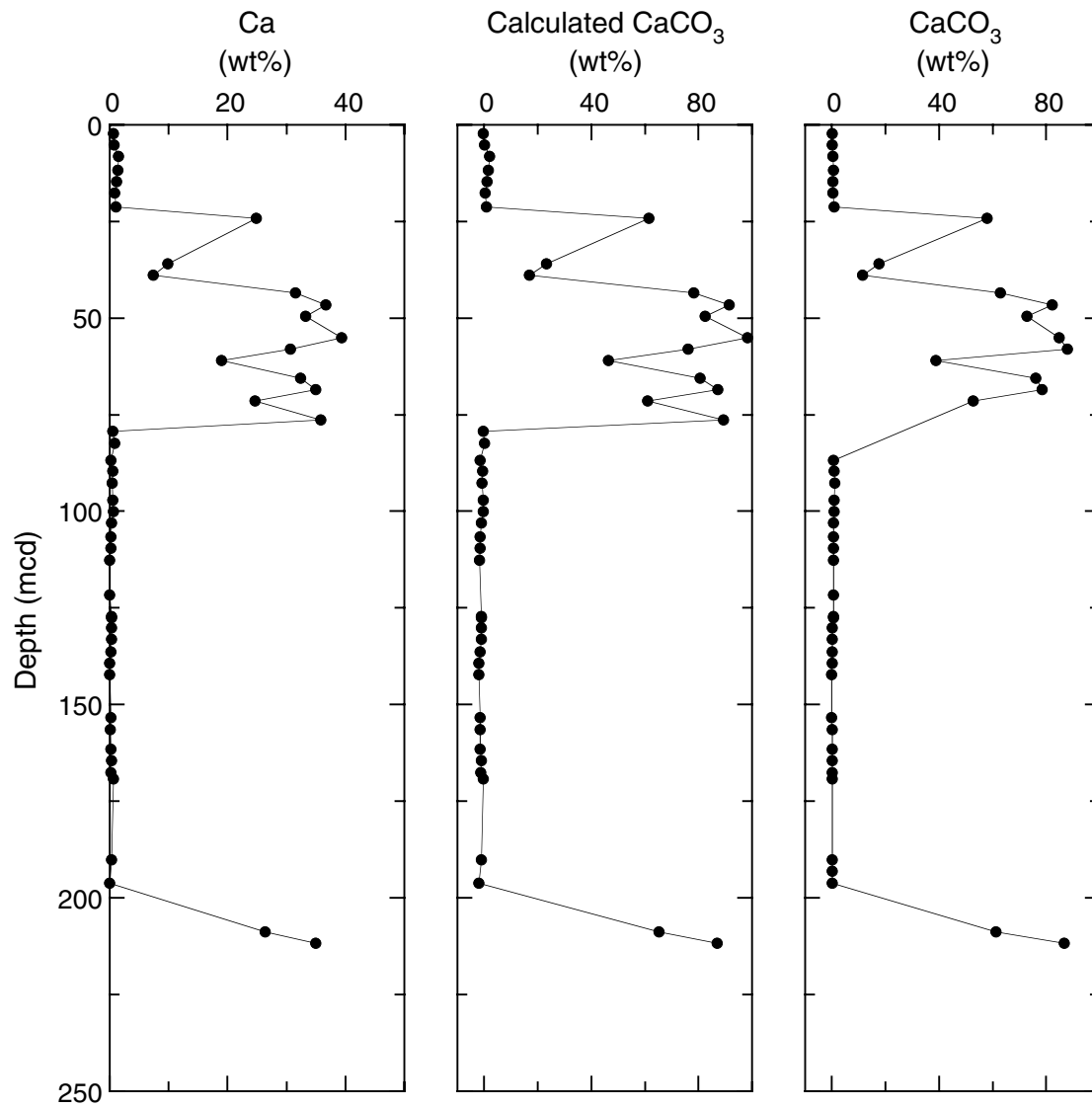


Figure F22. Bulk-sediment data for the P/E boundary from Site 1220. Data are plotted with depth as the top of the sample interval. Ca values higher than 35.9 wt% are out of the range of the standards (see "Geochemistry," p. 20, in the "Explanatory Notes" chapter).

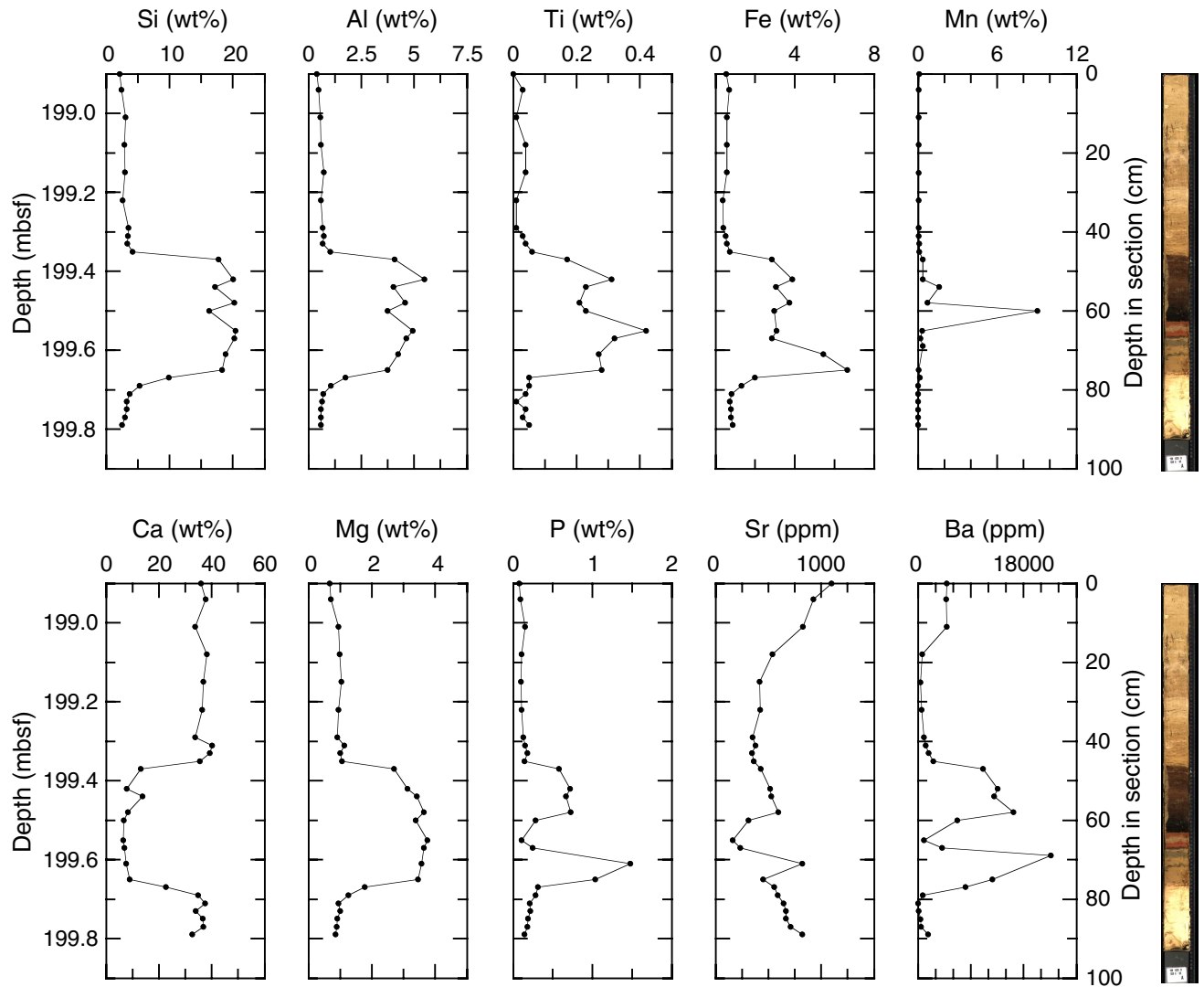


Figure F23. MAD measurements from Hole 1220A and Cores 199-1220B-9H through 20X. A. Porosity (solid symbols) and water content (open symbols). B. Discrete-sample wet bulk density (open symbols) and gamma ray attenuation (GRA) bulk density (line). C. Grain density. Lithologic Units I–V are noted on the right side of the figure.

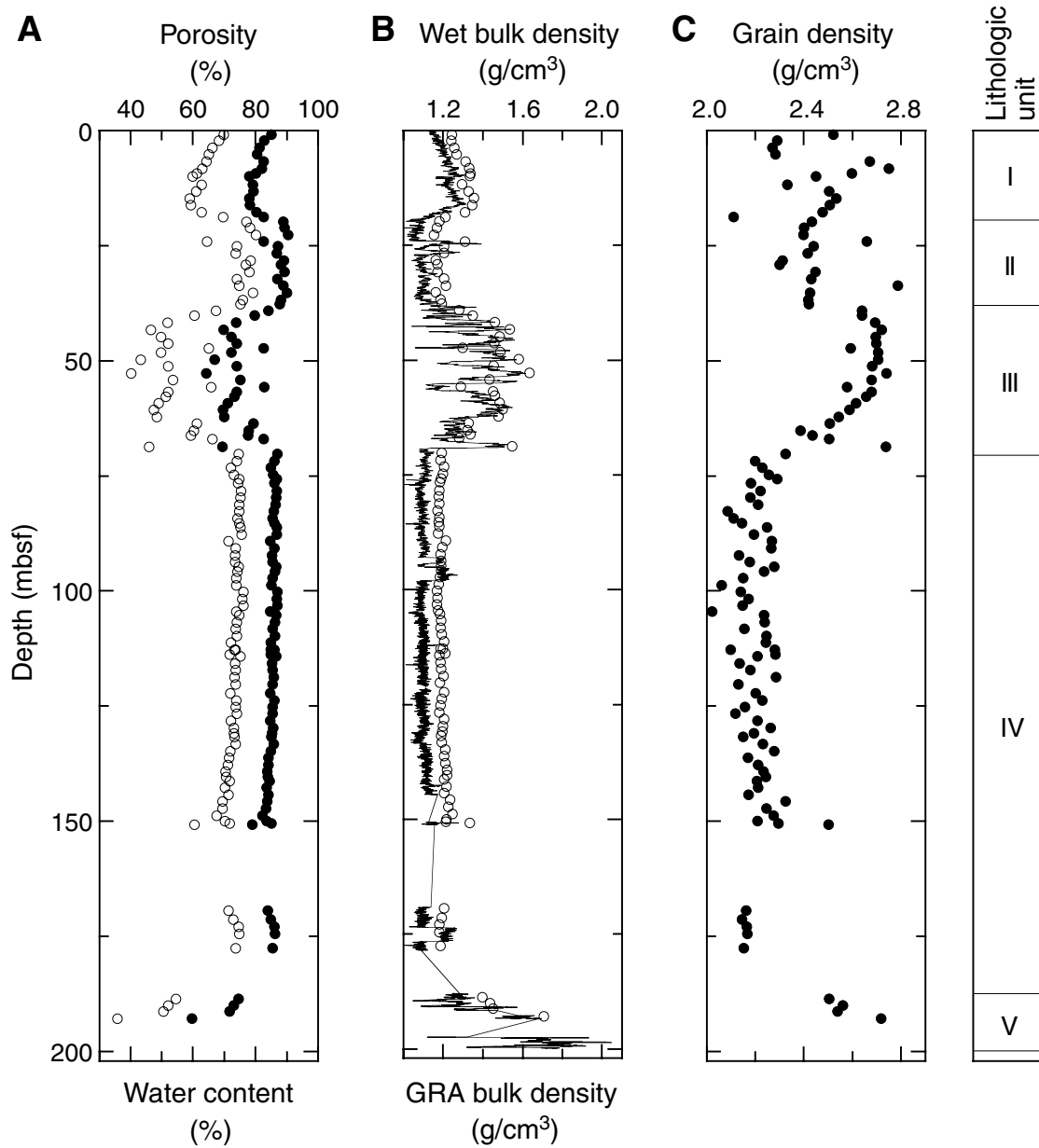


Figure F24. Comparison of magnetic susceptibility and gamma ray attenuation (GRA) bulk density with the digital core image from Section 199-1220B-20X-2. The red arrow denotes the Paleocene/Eocene (P/E) boundary.

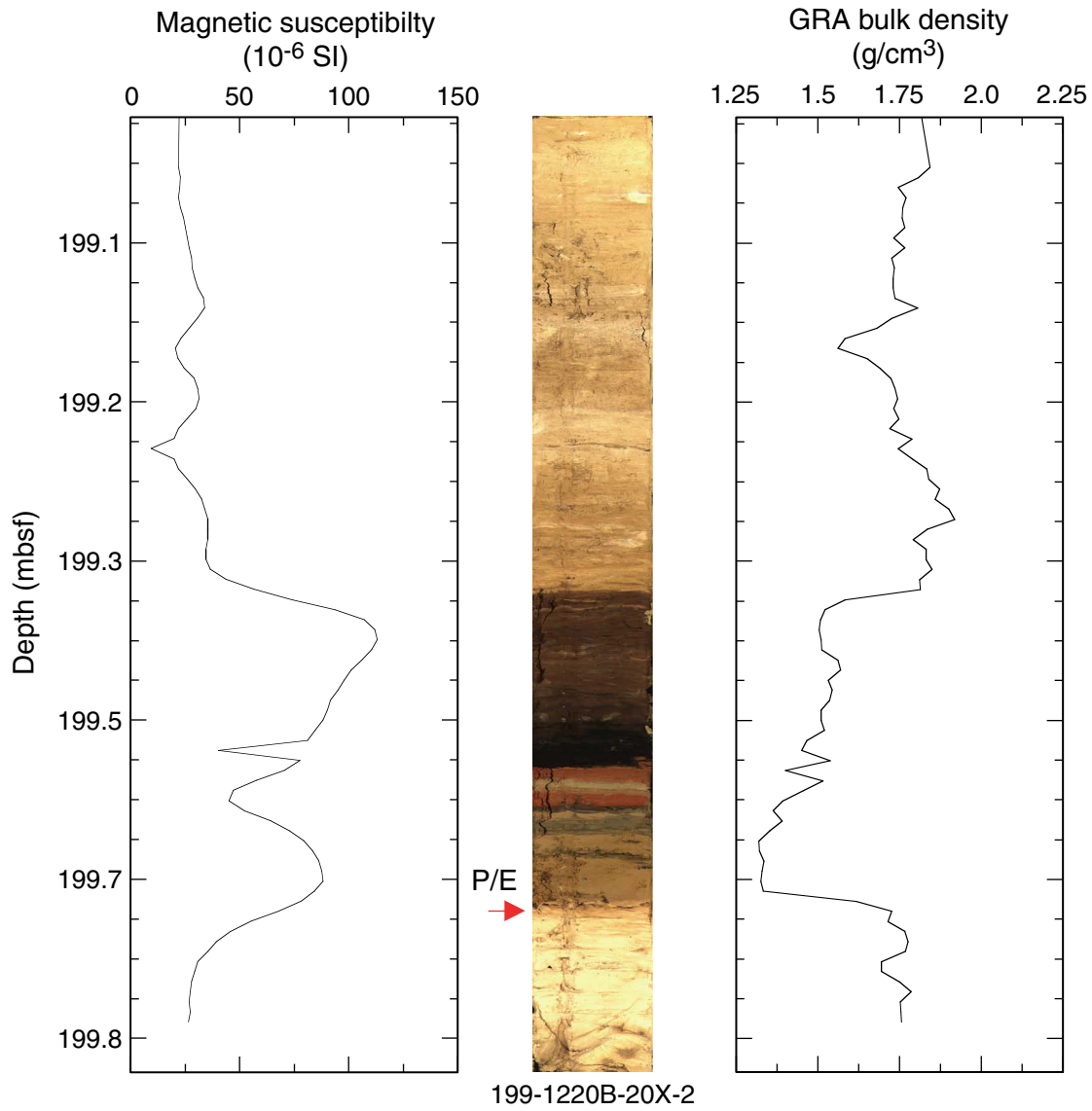


Figure F25. (A) Wet and (B) dry bulk density from discrete samples from Hole 1220A and Cores 199-1220B-9H through 20X plotted with gamma ray attenuation (GRA) bulk density interpolated with a 20-cm-wide Gaussian window. Samples from APC cores are indicated by solid symbols; XCB cores are represented by open symbols.

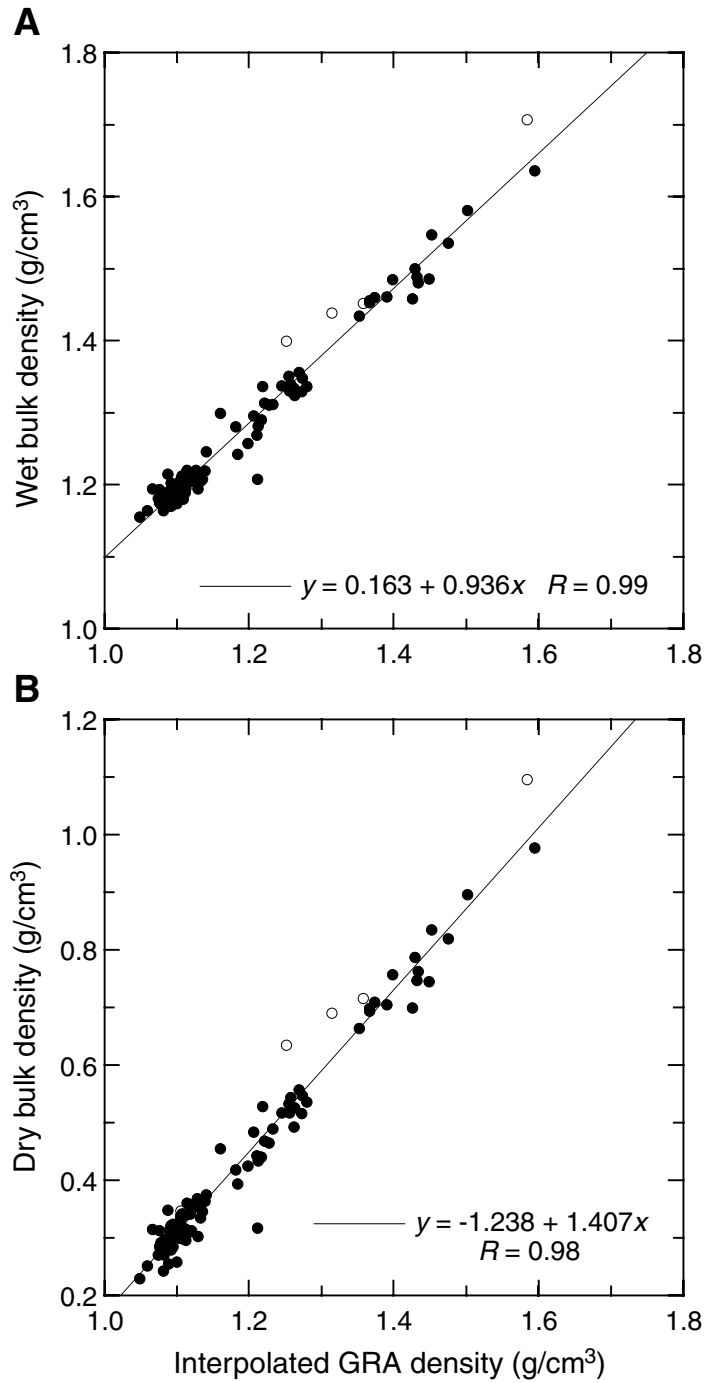


Figure F26. LAS mineralogy determinations for Hole 1220A and Cores 199-1220B-9H through 19X. Lithologic Units I-V and ages are noted to the left of the figure. rad = radiolarian.

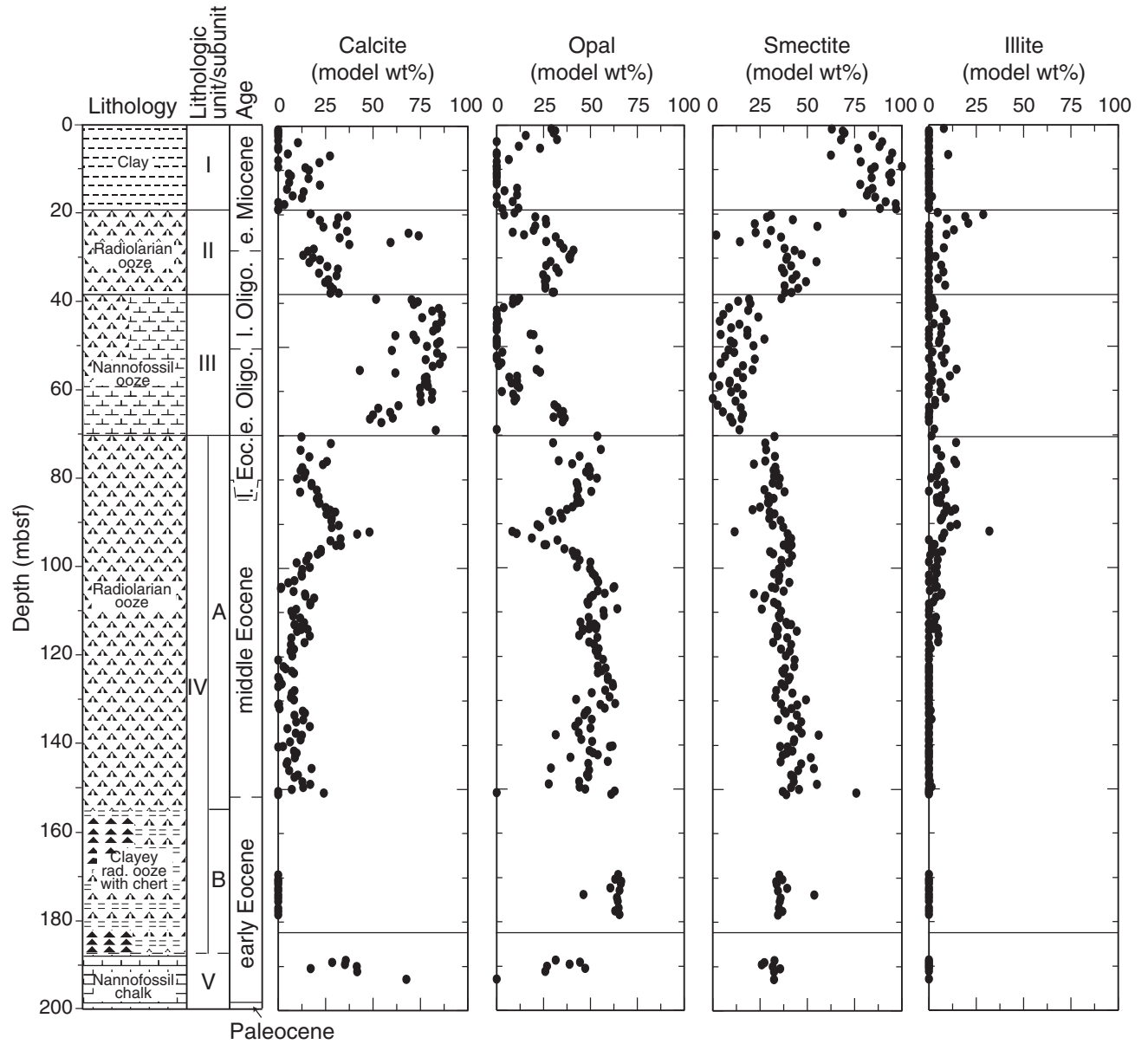


Figure F27. Compressional wave velocity from the PWL (line) and transverse velocity measurements of the insertion (squares) and contact probe (circles) systems for Hole 1220A and Cores 199-1220B-9H through 20X. Velocity measurements of chert samples from Cores 199-1220B-15X, 17X, and 20X, which range from 3179 to 4893 m/s, are not shown. Lithologic Units I-V are noted on the right side of the figure.

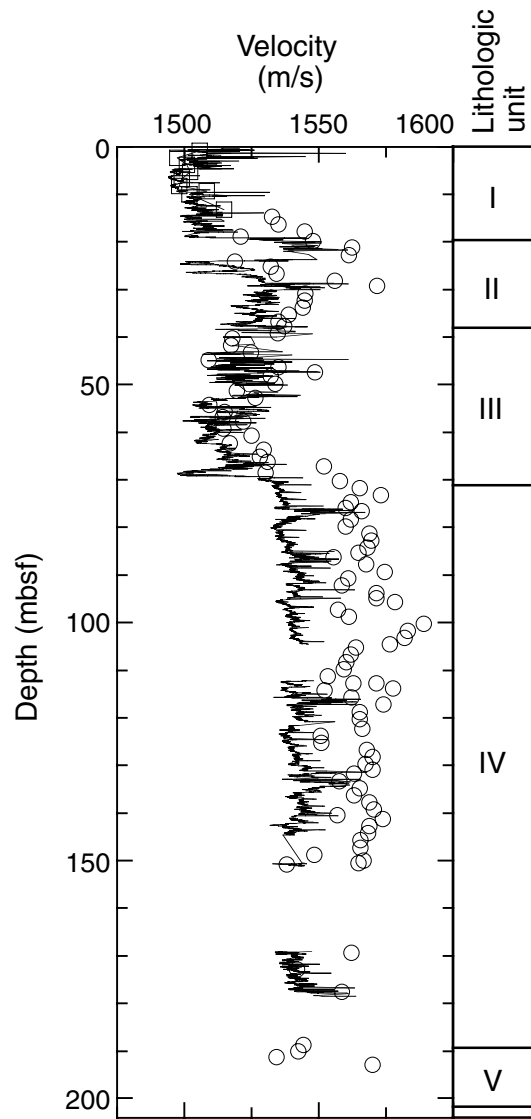


Figure F28. Compressional wave velocity (transverse) plotted with wet bulk density. Samples are distinguished by lithology: clay (open circles), nannofossil ooze and chalk (diamonds), and radiolarian clay and ooze (solid circles).

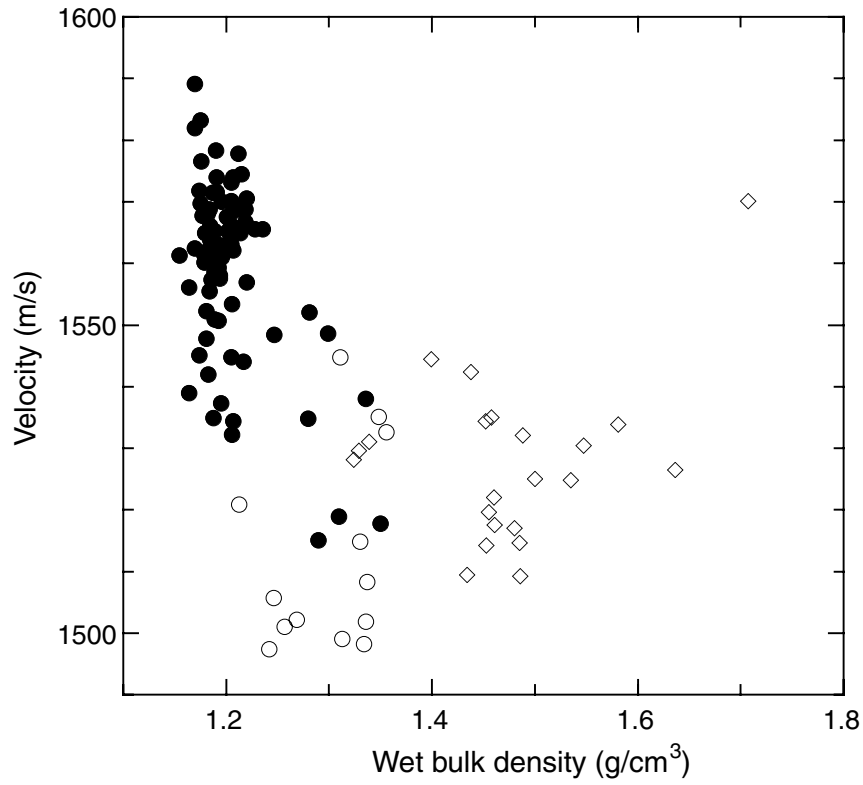


Figure F29. Thermal conductivity for Holes 1220A (solid symbols) and 1220B (open symbols). Lithologic Units I–V are noted on the right side of the figure.

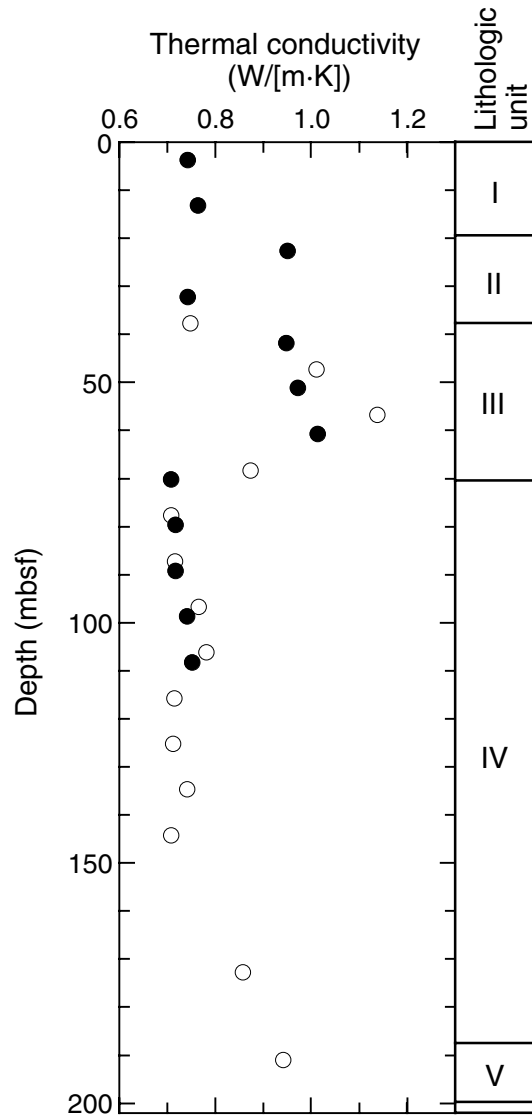


Figure F30. Thermal conductivity plotted with porosity for Holes 1220A and 1220B. An inverse relationship between thermal conductivity and porosity characterizes the clay (solid circles) and nannofossil ooze (squares) but is lacking in the radiolarian ooze and clay (open circles). Porosity values for Cores 199-1220B-2H through 8H were derived from the gamma ray attenuation (GRA) bulk density using the regression of porosity with GRA bulk density for sediments in Hole 1220A and Cores 199-1220B-9H through 20X. Porosity =  $136.8 - \text{GRA density} \times 46.0$ .  $R = 0.96$ .

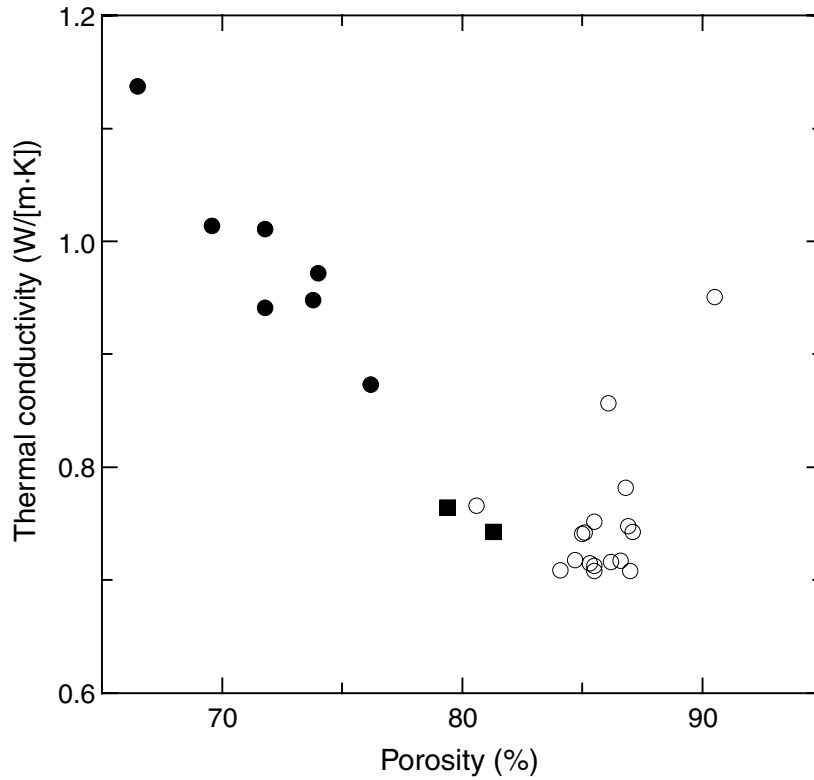


Figure F31. Heat flow calculation for Site 1220. A. Sediment temperatures from Hole 1220B. B. Thermal resistance calculated for four layers with constant in situ thermal conductivity: (1) 0–38 mbsf (Units I and II) = 0.72 W/(m·K); (2) 38–69 mbsf (Unit III) = 0.96 W/(m·K); (3) 69–188 mbsf (Unit IV) = 0.71 W/(m·K), and (4) 188–200 mbsf (Unit V) = 0.93 W/(m·K). C. Bullard plot, heat flow calculated from a linear regression of all data.

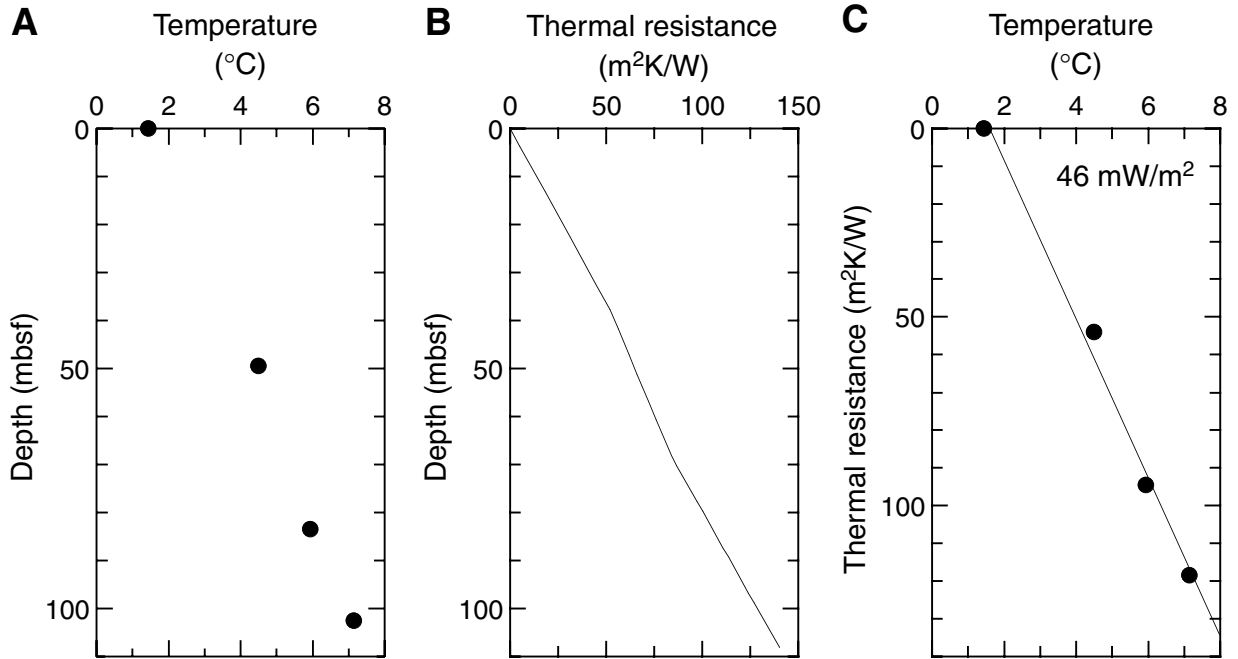


Figure F32. Natural gamma radiation for Hole 1220A. Most data below 25 mbsf are at or near background levels. Lithologic Units I-V are noted on the right side of the figure. cps = counts per second.

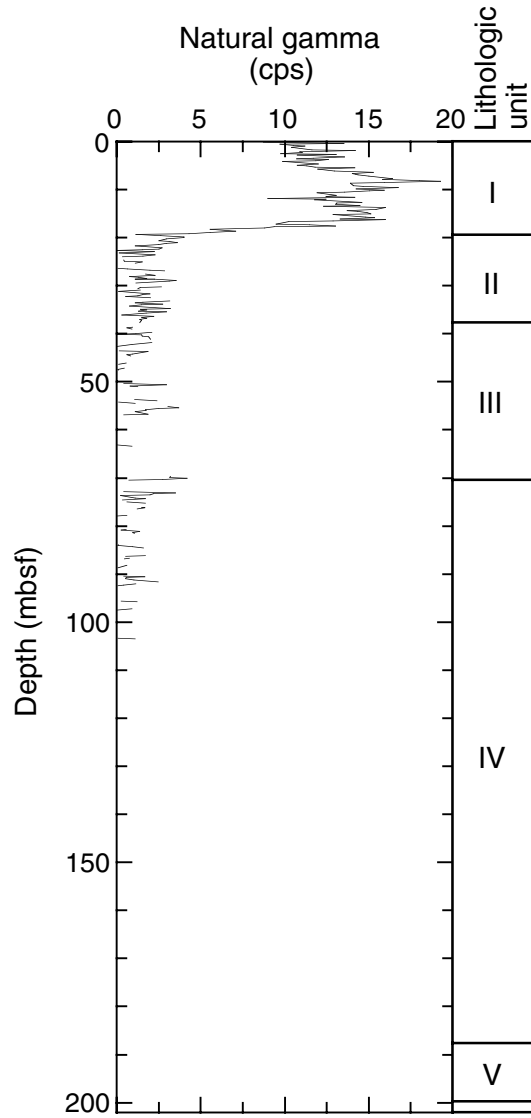
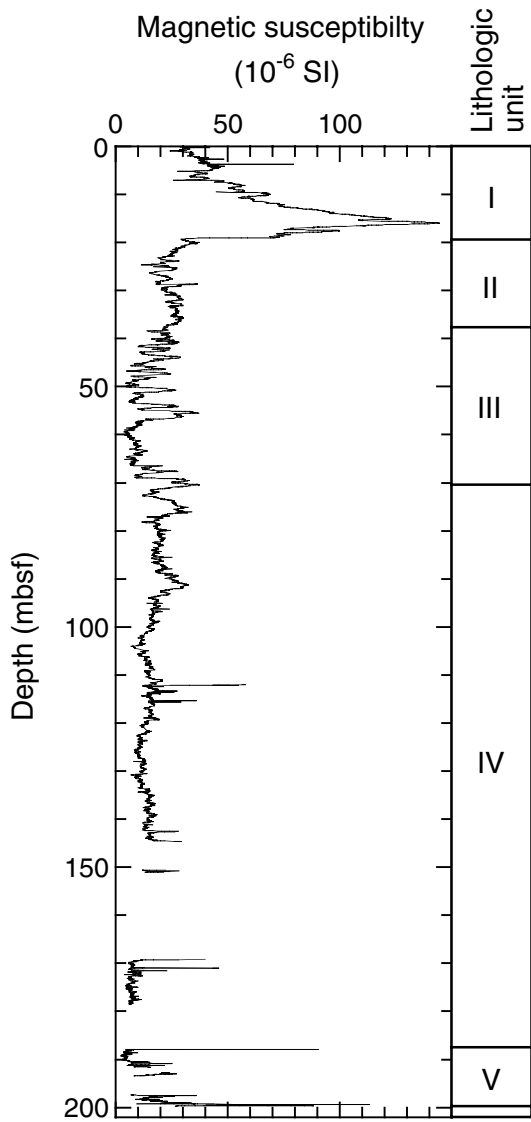


Figure F33. Magnetic susceptibility for Hole 1220A and Cores 199-1220B-9H through 20X. Lithologic Units I-V are noted on the right side of the figure.



**Table T1.** Coring summary, Site 1220. (See table note. Continued on next page.)

**Hole 1220A**

Latitude: 10°10.6008'N  
 Longitude: 142°45.4917'W  
 Time on site (hr): 134.25 (1915 hr, 28 Nov–0930 hr, 4 Dec 2001)  
 Time on hole (hr): 37.75 (1915 hr, 28 Nov–0900 hr, 30 Nov 2001)  
 Seafloor (drill pipe measurement from rig floor, mbrf): 5229.1  
 Distance between rig floor and sea level (m): 11.2  
 Water depth (drill pipe measurement from sea level, m): 5217.9  
 Total depth (drill pipe measurement from rig floor, mbrf): 5343.10  
 Total penetration (meters below seafloor, mbsf): 114.00  
 Total length of cored section (m): 114.0  
 Total core recovered (m): 118.68  
 Core recovery (%): 104.1  
 Total number of cores: 12  
 Total number of drilled intervals: 0

**Hole 1220B**

Latitude: 10°10.6001'N  
 Longitude: 142°45.5028'W  
 Time on hole (hr): 54.5 (0900 hr, 30 Nov–1530 hr, 2 Dec 2001)  
 Seafloor (drill pipe measurement from rig floor, mbrf): 5229.1  
 Distance between rig floor and sea level (m): 11.2  
 Water depth (drill pipe measurement from sea level, m): 5217.9  
 Total depth (drill pipe measurement from rig floor, mbrf): 5431.1  
 Total penetration (meters below seafloor, mbsf): 202.0  
 Total length of cored section (m): 166.0  
 Total length of drilled intervals (m): 36.0  
 Total core recovered (m): 144.65  
 Core recovery (%): 87.1  
 Total number of cores: 20  
 Total number of drilled intervals: 2

**Hole 1220C**

Latitude: 10°10.6002'N  
 Longitude: 142°45.5148' W  
 Time on hole: 42 (1530 hr, 2 Dec–0930 hr, 4 Dec 2001)  
 Seafloor (drill pipe measurement from rig floor, mbrf): 5229.1  
 Distance between rig floor and sea level (m): 11.2  
 Water depth (drill pipe measurement from sea level, m): 5217.9  
 Total depth (drill pipe measurement from rig floor, mbrf): 5433.2  
 Total penetration (meters below seafloor, mbsf): 204.1  
 Total length of cored section (m): 153.6  
 Total length of drilled intervals (m): 50.5  
 Total core recovered (m): 116.12  
 Core recovery (%): 75.6  
 Total number of cores: 17  
 Total number of drilled intervals: 2

Core	Date (2001)	Ship local time	Depth (mbsf)		Length (m)		Recovery (%)
			Top	Bottom	Cored	Recovered	
<b>199-1220A-</b>							
1H	Nov 29	0550	0.0	9.5	9.5	9.86	103.8
2H	Nov 29	0705	9.5	19.0	9.5	9.87	103.9
3H	Nov 29	0820	19.0	28.5	9.5	10.04	105.7
4H	Nov 29	0930	28.5	38.0	9.5	9.64	101.5
5H	Nov 29	1040	38.0	47.5	9.5	10.05	105.8
6H	Nov 29	1200	47.5	57.0	9.5	9.89	104.1
7H	Nov 29	1300	57.0	66.5	9.5	9.71	102.2
8H	Nov 29	1420	66.5	76.0	9.5	10.01	105.4
9H	Nov 29	1535	76.0	85.5	9.5	9.89	104.1
10H	Nov 29	1645	85.5	95.0	9.5	9.73	102.4
11H	Nov 29	1945	95.0	104.5	9.5	10.12	106.5
12H	Nov 30	1000	104.5	114.0	9.5	9.87	103.9
Cored totals:					114.0	118.68	104.1
<b>199-1220B-</b>							
*****Drilled from 0.0 to 34.0*****							
1H	Dec 1	0030	34.0	43.5	9.5	9.47	99.7
2H	Dec 1	0225	43.5	53.0	9.5	10.09	106.2
3H	Dec 1	0355	53.0	62.5	9.5	9.59	101.0

Table T1 (continued).

Core	Date (2001)	Ship local time	Depth (mbsf)		Length (m)		Recovery (%)
			Top	Bottom	Cored	Recovered	
*****Drilled from 62.5 to 64.5 mbsf*****							
4H	Dec 1	0525	64.5	74.0	9.5	9.23	97.2
5H	Dec 1	0700	74.0	83.5	9.5	10.06	105.9
6H	Dec 1	0830	83.5	93.0	9.5	9.82	103.4
7H	Dec 1	1005	93.0	102.5	9.5	9.96	104.8
8H	Dec 1	1135	102.5	112.0	9.5	9.89	104.1
9H	Dec 1	1245	112.0	121.5	9.5	9.23	97.2
10H	Dec 1	1400	121.5	131.0	9.5	10.15	106.8
11H	Dec 1	1520	131.0	140.5	9.5	10.09	106.2
12H	Dec 1	1640	140.5	150.0	9.5	10.06	105.9
13H	Dec 1	1805	150.0	152.0	2.0	9.19	459.5
14X	Dec 1	2115	152.0	159.5	7.5	0.03	0.4
15X	Dec 1	2345	159.5	169.1	9.6	0.05	0.5
16X	Dec 2	0145	169.1	178.3	9.2	9.68	105.2
17X	Dec 2	0350	178.3	187.9	9.6	0.11	1.2
18X	Dec 2	0625	187.9	192.4	4.5	3.99	88.7
19X	Dec 2	0905	192.4	197.4	5.0	1.33	26.6
20X	Dec 2	1200	197.4	202.0	4.6	2.63	57.2
Cored totals:					166.0	144.65	87.1
Drilled total:					36.0		
Total:					202.0		
199-1220C-							
*****Drilled from 0.0 to 25.0 mbsf*****							
1H	Dec 2	1755	25.0	34.5	9.5	10.05	105.8
*****Drilled from 34.5 to 60.0*****							
2H	Dec 2	2010	60.0	69.5	9.5	8.66	91.2
3H	Dec 2	2125	69.5	79.0	9.5	9.98	105.1
4H	Dec 2	2240	79.0	88.5	9.5	9.69	102.0
5H	Dec 3	0030	88.5	98.0	9.5	10.09	106.2
6H	Dec 3	0135	98.0	107.5	9.5	9.78	103.0
7H	Dec 3	0255	107.5	117.0	9.5	9.96	104.8
8H	Dec 3	0455	117.0	126.5	9.5	9.76	102.7
9H	Dec 3	0625	126.5	136.0	9.5	10.16	107.0
10H	Dec 3	0750	136.0	145.5	9.5	9.86	103.8
11X	Dec 3	1000	145.5	155.1	9.6	7.59	79.1
12X	Dec 3	1235	155.1	164.7	9.6	0.31	3.2
13X	Dec 3	1440	164.7	173.9	9.2	0.13	1.4
14X	Dec 3	1620	173.9	183.5	9.6	8.58	89.4
15X	Dec 3	1820	183.5	193.0	9.5	0.00	0.0
16X	Dec 3	2015	193.0	197.4	4.4	0.97	22.1
17X	Dec 3	2255	197.4	204.1	6.7	0.55	8.2
Cored totals:					153.6	116.12	75.6
Drilled total:					50.5		
Total:					204.1		

Note: The expanded coring summary table is available in ASCII (see the "Supplementary Material" contents list).

**Table T2.** Calcareous nannofossil datums, Holes 1220A and 1220B.

Core, section, interval (cm)		Marker species	Age (Ma)	Depth (mbsf)		Depth (mcd)	
Top	Bottom			Midpoint	±	Midpoint	±
199-1220A-	199-1220A-						
3H-5, 60	3H-6, 40	T <i>Triquetrorhabdulus carinatus acme</i>	22.9	25.70	0.65	25.70	0.65
5H-1, 60	5H-1, 140	B <i>Sphenolithus ciperoensis</i>	28.1	39.00	0.40	42.29	0.40
5H-4, 60	5H-5, 45	T <i>Sphenolithus pseudoradians</i>	29.1	43.78	0.68	47.07	0.68
6H-3, 100	6H-4, 80	B <i>Sphenolithus distentus</i>	30.4	52.15	0.65	57.49	0.65
7H-4, 70	7H-4, 140	T <i>Reticulofenestra umbilicus</i> ≥14 µm	31.7	62.51	0.35	68.82	0.35
199-1220B-	199-1220B-						
3H-1, 60	3H-1, 90	B <i>Sphenolithus distentus</i>	30.4	53.75	0.15	57.14	0.15
4H-3, 60	4H-3, 100	T <i>Ericsonia formosa</i>	32.9	68.30	0.20	73.69	0.20
18X-3, 120	18X-3, 145	X <i>Tribrachiatus contortus/T. orthostylus</i>	53.4	191.55	0.13	210.26	0.13
19X-CC	20X-1, 20	B <i>Tribrachiatus bramlettei</i>	53.9	195.67	1.94	214.38	1.94
20X-1, 90	20X-1, 115	T <i>Fasciculithus</i> spp.*	54.1	198.43	0.13	217.14	0.13
20X-1, 105	20X-1, 115	X <i>Fasciculithus/Rhombaster</i> *	54.1	198.50	0.05	217.21	0.05
20X-1, 125	20X-2, 1	B <i>Rhombaster</i> spp.*	54.1	198.78	0.13	217.49	0.13

Notes: T = top, B = bottom, X = abundance cross-over. \* = age estimates in need of revision; events occur 0.77–1.38 m above the Paleocene/Eocene boundary (199-1220B-20X-2, 78 cm). This table is also available in [ASCII](#). [N1]

Table T3. Distribution of late Paleocene–early Eocene planktonic foraminifers, Holes 1220B and 1220C.

Core, section, interval (cm)	Depth (mbsf)	Zone	Preservation	Group abundance	<i>Acarinina berggreni</i>	<i>Acarinina africana</i>	<i>Acarinina coalingsensis</i>	<i>Acarinina nitida</i>	<i>Acarinina quetra</i>	<i>Acarinina sibaiaensis</i>	<i>Acarinina soldadoensis</i>	<i>Acarinina wilcoxensis</i>	<i>Chiloguembelina</i> sp.	<i>Globanomalina ovalis</i>	<i>Globanomalina planoconica</i>	<i>Globanomalina pseudomitata</i>	<i>Igorina broedermanni</i>	<i>Morozovella acuta</i>	<i>Morozovella aequa</i>	<i>Morozovella allisonensis</i>	<i>Morozovella apantesma</i>	<i>Morozovella gracilis</i>	<i>Morozovella marginodentata</i>	<i>Morozovella subbotinae</i>	<i>Morozovella velascoensis</i>	<i>Parasubbotina paleocenica</i>	<i>Parasubbotina varianta</i>	<i>Pseudohastigerina</i> sp.	<i>Subbotina patagonica</i>	<i>Subbotina triangularis</i>	<i>Subbotina velascoensis</i>			
199-1220B-18X-1, 8–13	187.98	P6	P	R			R			R																								
18X-2, 58–63	189.98		P	T			R																											
18X-3, 119–124	191.41		P	R			P																											
18X-CC, 11–17	191.83																																	
19X-1, 77–79	193.17		P	R			F		R		F	A			P		P						P									F		
19X-CC, 14–19	193.68		M	C	P		A				A					P		R					R	A						P				
20X-1, 23–30	197.63		P	R			F				F										P			A										
20X-1, 44–52	197.84		P	R			R	F			R										P												P	
20X-1, 59–66	197.99		P	R			F	R			F			P										R										
20X-2, 1.5–3.5	198.90	P5	G	A			F	F		A	R			R		R	A				F	R	F									F		
20X-2, 6–13	198.96		M	F			F				F				P		R						P										P	
20X-2, 13–20	199.03		M	F			A	F			A			P	P	P		A					R			R								
20X-2, 13–21	199.03		M	F			R	A			A				P								F			R								
20X-2, 21–28	199.11		M	A			F	A			R	A	F	F				A	A		R	R				R		R	F	R	A			
20X-2, 28–35	199.18		M	C			F	A			R	A	P	F	R			R	F		R					R				P				
20X-2, 35–43	199.25		M	F			F	A			F	A		F				R	F									R						
20X-2, 50–57	199.40		M	R							P													A										
20X-2, 57–64.5	199.47		M	R			P				P			P				P		P				P										
20X-2, 65.5–73	199.56		P	F			F				A		A								P			F										F
20X-2, 68–75	199.58		P	R			P														P	R												
20X-2, 74–78	199.64		P	R	P/E						P				P									P										
20X-CC, 8–13	199.93		M	A			A	A	F		R	A		R	F	F	P		F	A	R			A			R	R	R					R
199-1220C-16X-CC, 0–3	193.91							F			P													F										P

Notes: Preservation: G = good, M = moderate, P = poor. Group abundance: A = abundant, C = common, F = few, R = rare, T = trace (a single specimen was found), P = present (presence of one or two individuals in a given sample). Heavy dashed line = position of the P/E boundary, as indicated by the benthic foraminifer extinction in the base of Hole 1220B. Planktonic foraminifers are extremely scarce in the Oligocene sequence and description of their occurrence is limited to the text (see “**Planktonic Foraminifers**,” p. 13, in “Biostratigraphy.”).





**Table T5.** Radiolarian first and last occurrences and zonal boundaries, Site 1220.

Zonal boundaries	Age (Ma)	Hole, core, section, interval (cm)		Depth (mbsf)		Depth (mcd)	
		Top	Bottom	Midpoint	±	Midpoint	±
		199-	199-				
RN1/RP22	23.62	1220A-3H-4, 45	1220A-3H-5, 45	24.40	0.50	24.40	0.50
RP22/21	24.60	1220A-4H-2, 45	1220A-4H-3, 45	31.20	0.75	33.45	0.75
RP21/20	28.80	1220A-5H-CC,	1220A-6H-1, 45	48.03	0.03	52.29	1.00
RP20/19	32.80	1220A-8H-2, 20	1220A-8H-3, 46	69.08	0.88	76.72	0.88
RP19/18	34.90	1220A-8H-6, 46	1220A-8H-7, 46	75.21	0.75	82.85	0.75
RP18/17	36.40	1220A-9H-6, 45	1220A-9H-7, 45	84.70	0.75	93.19	0.75
RP17/16	37.70	1220A-10H-4, 45	1220A-10H-5, 45	91.20	0.75	100.52	0.75
RP16/15	38.80	1220A-11H-7, 45	1220A-11H-CC	104.77	0.32	114.19	0.32
RP15/14	39.50	1220B-9H-1, 45	1220A-12H-5, 45	111.70	0.75	125.60	0.22
RP14/13	42.80	1220B-10H-3, 45	1220B-10H-4, 45	125.64	0.75	138.27	0.75
RP13/12	44.50	1220B-11H-1, 45	1220B-11H-2, 45	132.20	0.75	149.39	0.75
RP12/11	47.5	1220B-11H-CC	1220C-11H-3, 10	144.83	3.77	160.10	1.85
RP11/10	48.5	1220B-13H-CC	1220B-16X-1, 100	164.63	5.47	183.34	5.47
RP10/9	49	1220B-13H-CC	1220B-16X-1, 100	164.63	5.47	183.34	5.47
RP9/8	50.3	1220A-13H-CC	1220B-16X-1, 100	164.63	5.47	183.34	5.47
RP8/7	52.8	1220B-18X-2, 10	1220C-14X-6, 60	185.75	3.75	197.45	0.31

Notes: Derivation of ages is shown in Table T3, p. 71 (see “Radiolarian Zonal Scheme and Taxonomy” p. 11, in “Biostratigraphy” in the “Explanatory Notes” chapter). This table is also available in ASCII. [N1]

**Table T6.** Composite depths of identified geomagnetic reversals, Site 1220.

Chron/ Subchron	Age (Ma)	Depth (mcd)
T C6An.1n	20.518	20.16
B C6An.1n	20.725	20.73
T C6An.2n	20.996	21.15
B C6An.2n	21.320	22.00
T C6AAAn	21.768	22.85
B C6AAAn	21.859	23.13
T C6AAr.1n	22.151	23.98
B C6AAr.1n	22.248	24.26
T C6AAr.2n	22.459	24.89
B C6AAr.2n	22.493	25.00
T C6Bn.1n	22.588	25.25
B C6Bn.1n	22.750	25.70
T C6Bn.2n	22.804	25.75
B C6Bn.2n	23.069	26.67
T C6Cn.1n	23.353	27.68
B C6Cn.1n	23.535	28.06
T C6Cn.2n	23.677	28.71
B C6Cn.2n	23.800	28.98
T C6Cn.3n	23.999	29.56
B C6Cn.3n	24.118	29.73
T C7n.1n	24.730	32.11
B C7n.1n	24.781	32.20
T C7n.2n	24.835	32.64
B C7n.2n	25.183	33.78
T C8n.1n	25.823	35.72
B C8n.1n	25.951	36.20
T C8n.2n	25.992	36.28
B C8n.2n	26.554	39.23
T C9n	27.027	41.08
B C9n	27.972	44.05
T C10n.1n	28.283	44.75
B C10n.1n	28.512	46.88
T C10n.2n	28.578	47.16
B C10n.2n	28.745	47.66
T C11n.1n	29.401	53.60
B C11n.1n	29.662	55.72
T C11n.2n	29.765	56.00
B C11n.2n	30.098	57.48
T C12n	30.479	59.68
B C12n	30.939	61.09
T C13n	33.058	74.79
B C13n	33.545	76.97
T C15n	34.655	82.67
B C15n	34.940	83.70
T C16n.1n	35.343	85.30
B C16n.1n	35.526	86.42
T C16n.2n	35.685	87.15
B C16n.2n	36.341	91.15
T C17n.1n	36.618	92.61
B C17n.1n	37.473	97.45
T C17n.2n	37.604	98.18
B C17n.2n	37.848	99.27
T C17n.3n	37.920	99.64
B C17n.3n	38.113	100.36
T C18n.1n	38.426	101.94
B C18n.1n	39.552	108.85
T C18n.2n	39.631	109.70
B C18n.2n	40.130	114.06
T C19n	41.257	125.05
B C19n	41.521	126.16
T C20n	42.536	131.41
B C20n	43.789	142.32
T C21n	46.264	169.30

Notes: T = top, B = bottom. This table is also available in [ASCII](#).

Table T7. Core disturbance, Site 1220.

Core, section, interval (cm)	Depth (mbsf)		Comments	Core, section, interval (cm)	Depth (mbsf)		Comments
	Top	Bottom			Top	Bottom	
199-1220A-				12H-3, 117-150	144.67	145.00	Flow-in
1H-1, 0-2	0.00	0.02		12H-4, 0-150	145.00	146.50	Flow-in
3H-1, 110-112	20.10	20.12	Void	12H-5, 0-150	146.50	148.00	Flow-in
3H-1, 137-140	20.37	20.40	Crack	12H-6, 0-150	148.00	149.50	Flow-in
4H-1, 0-11	28.50	28.61	Flow-in	12H-7, 0-78	149.50	150.28	Flow-in
4H-1, 90-91	29.40	29.41	Crack	12H-CC, 0-28	150.28	150.56	Flow-in
4H-1, 142-144	29.92	29.94	Crack	13H-1, 115-150	151.15	151.50	Flow-in
4H-CC, 0-20	37.94	38.14	Disturbed	13H-2, 0-150	151.50	153.00	Flow-in
5H-1, 0-5	38.00	38.05	Flow-in	13H-3, 0-150	153.00	154.50	Flow-in
5H-1, 0-10	38.00	38.10	Flow-in	13H-4, 0-150	154.50	156.00	Flow-in
5H-1, 38-41	38.38	38.41	Crack	13H-5, 0-150	156.00	157.50	Flow-in
5H-1, 78-83	38.78	38.83	Void	13H-6, 0-151	157.50	159.01	Flow-in
6H-1, 0-30	47.50	47.80	Flow-in	13H-CC, 0-18	159.01	159.19	Flow-in
7H-1, 0-10	57.00	57.10	Weak flow-in	14X-CC, 0-3	152.00	152.03	Void
8H-1, 0-4	66.50	66.54	Downhole debris	15X-CC, 0-5	159.50	159.55	Void
11H-7, 14-25	104.14	104.25	Soupy	16X-1, 0-5	169.10	169.15	Disturbed
12H-1, 0-38	104.50	104.88	Downhole debris	16X-2, 88-92	171.48	171.52	Ash
12H-2, 0-3	106.00	106.03	Cutting disturbance	18X-1, 93-97	188.83	188.87	Void
12H-3, 0-1	107.50	107.51	Cutting disturbance	19X-1, 0-27	192.40	192.67	Chert
12H-4, 0-2	109.00	109.02	Cutting disturbance	199-1220C-			
12H-5, 0-1	110.50	110.51	Cutting disturbance	1H-1, 0-30	25.00	25.30	Flow-in
12H-6, 0-1	112.00	112.01	Cutting disturbance	2H-1, 0-150	60.00	61.50	Soupy
12H-CC, 13-26	114.23	114.36	Disturbed	2H-2, 0-53	61.50	62.03	Soupy
199-1220B-				2H-2, 53-150	62.03	63.00	Flow-in
1H-1, 0-150	34.00	35.50	Soupy	2H-3, 0-29	63.00	63.29	Flow-in
1H-2, 0-17	35.50	35.67	Soupy	2H-6, 70-75	68.20	68.25	Disturbed
2H-1, 0-3	43.50	43.53	Downhole debris	2H-7, 0-36	68.24	68.60	Disturbed
3H-1, 0-16	53.00	53.16	Soupy	3H-1, 27-29	69.77	69.79	Void
4H-1, 0-28	64.50	64.78	Soupy	3H-2, 52-54	71.52	71.54	Void
4H-1, 28-50	64.78	65.00	Void	6H-1, 0-28	98.00	98.28	Disturbed
5H-1, 0-3	74.00	74.03	Soupy	9H-1, 0-52	126.50	127.02	Soupy/disturbed
6H-2, 24-25	85.17	85.18	Crack	10H-1, 0-1	136.00	136.01	Soupy
7H-1, 0-20	93.00	93.20	Flow-in	10H-4, 0-3	140.50	140.53	Soupy
8H-1, 0-12	102.50	102.62	Soupy	11X-2, 94-150	147.94	148.50	Soupy
8H-2, 0-1	104.00	104.01	Disturbed	11X-3, 145-150	149.95	150.00	Weakly disturbed
8H-3, 0-1	105.50	105.51	Disturbed	11X-4, 37-44	150.37	150.44	Weakly disturbed
8H-4, 0-2	107.00	107.02	Disturbed	11X-5, 60-130	152.10	152.80	Weakly disturbed
8H-5, 0-2	108.50	108.52	Disturbed				
8H-6, 146-149	111.46	111.49	Disturbed				
10H-1, 0-10	121.50	121.60	Flow-in				
10H-1, 110-148	122.60	122.98	Cracked				
11H-1, 0-80	131.00	131.80	Disturbed				
11H-CC, 0-31	140.78	141.09	Disturbed				

Notes: Data from these intervals were removed from the GRA bulk density, MS, color reflectance, natural gamma, and P-wave velocity data sets prior to construction of the composite section. This table is also available in [ASCII](#). [N1]

Table T8. Composite depths, Site 1220.

Core	Length (m)	Depth (mbsf)	Offset (m)	Depth (mcd)
199-1220A-				
1H	9.5	0.00	0.00	0.00
2H	9.5	9.50	0.00	9.50
3H	9.5	19.00	0.00	19.00
4H	9.5	28.50	2.25	30.75
5H	9.5	38.00	3.29	41.29
6H	9.5	47.50	5.34	52.84
7H	9.5	57.00	6.31	63.31
8H	9.5	66.50	7.64	74.14
9H	9.5	76.00	8.49	84.49
10H	9.5	85.50	9.32	94.82
11H	9.5	95.00	9.42	104.42
12H	9.5	104.50	14.87	119.37
199-1220B-				
1H	9.5	34.00	0.05	34.05
2H	9.5	43.50	2.39	45.89
3H	9.5	53.00	3.39	56.39
4H	9.5	64.50	5.39	69.89
5H	9.5	74.00	6.44	80.44
6H	9.5	83.50	8.24	91.74
7H	9.5	93.00	9.82	102.82
8H	9.5	102.50	11.37	113.87
9H	9.5	112.00	12.93	124.93
10H	9.5	121.50	12.63	134.13
11H	9.5	131.00	17.19	148.19
12H	9.5	140.50	18.71	159.21
13H	2.0	150.00	18.71	168.71
16X	9.2	169.10	18.71	187.81
18X	4.5	187.90	18.71	206.61
19X	5.0	192.40	18.71	211.11
20X	4.6	197.40	18.71	216.11
199-1220C-				
1H	9.5	25.00	-1.25	23.75
2H	9.5	60.00	2.17	62.17
3H	9.5	69.50	5.54	75.04
4H	9.5	79.00	7.39	86.39
5H	9.5	88.50	8.30	96.80
6H	9.5	98.00	8.82	106.82
7H	9.5	107.50	10.97	118.47
8H	9.5	117.00	11.25	128.25
9H	9.5	126.50	10.07	136.57
10H	9.5	136.00	11.67	147.67
11X	9.6	145.50	13.35	158.85
14X	9.6	173.90	15.75	189.65
16X	4.4	193.00	16.41	209.41

Note: This table is also available in [ASCII](#).

Table T9. Splice tie points, Site 1220.

Hole, core, section, interval (cm)	Depth			Hole, core, section, interval (cm)	Depth	
	(mbsf)	(mcd)			(mbsf)	(mcd)
199-				199-		
1220A-1H-7, 60	9.60	9.60	Tie to	1220A-2H-1, 24	9.70	9.60
1220A-2H-CC, 18	19.33	19.23	Append to	1220A-3H-1, 0	19.00	19.00
1220A-3H-6, 75	26.70	26.70	Tie to	1220C-1H-2, 145	27.95	26.70
1220C-1H-6, 80	33.30	32.05	Tie to	1220A-4H-1, 130	29.80	32.05
1220A-4H-5, 84	35.34	37.59	Tie to	1220B-1H-3, 54	37.54	37.59
1220B-1H-7, 46	42.96	43.01	Tie to	1220A-5H-2, 22	39.72	43.01
1220A-5H-5, 64	44.64	47.93	Tie to	1220B-2H-2, 54	45.54	47.93
1220B-2H-6, 10	51.10	53.49	Tie to	1220A-6H-1, 64.5	48.15	53.49
1220A-6H-5, 70	54.20	59.54	Tie to	1220B-3H-3, 15	56.15	59.54
1220B-3H-7, 30	61.80	65.19	Tie to	1220A-7H-2, 37	58.88	65.19
1220A-7H-6, 120	65.66	71.97	Tie to	1220B-4H-2, 58	66.58	71.97
1220B-4H-5, 14	69.74	75.13	Tie to	1220A-8H-1, 98.5	67.49	75.13
1220A-8H-6, 56	74.56	82.20	Tie to	1220B-5H-2, 26	75.76	82.20
1220B-5H-4, 142	79.92	86.36	Tie to	1220A-9H-2, 36.5	77.87	86.36
1220A-9H-7, 32	85.32	93.81	Tie to	1220B-6H-2, 64	85.57	93.81
1220B-6H-6, 65	91.48	99.72	Tie to	1220C-5H-2, 150	91.42	99.72
1220C-5H-5, 120	95.62	103.92	Tie to	1220B-7H-1, 110	94.10	103.92
1220B-7H-6, 10	100.60	110.42	Tie to	1220C-6H-3, 60	101.60	110.42
1220C-6H-6, 105	106.55	115.37	Tie to	1220B-8H-1, 150	104.00	115.37
1220B-8H-6, 40	110.40	121.77	Tie to	1220A-12H-2, 90	106.90	121.77
1220A-12H-6, 10	112.10	126.97	Tie to	1220B-9H-2, 53.5	114.04	126.97
1220B-9H-4, 140	117.90	130.83	Tie to	1220C-8H-2, 108	119.58	130.83
1220C-8H-6, 140	125.90	137.15	Tie to	1220B-10H-3, 8	124.52	137.15
1220B-10H-7, 88	131.32	143.95	Append to	1220B-11H-1, 0	131.00	148.19
1220B-11H-7, 74	140.74	157.93	Append to	1220C-11X-1, 0	145.50	158.85
1220C-11X-5, 140	152.90	166.25	Append to	1220B-13H-1, 0	150.00	168.71
1220B-13H-1, 114	151.14	169.85	Append to	1220B-16X-1, 0	169.10	187.81
1220B-16X-7, 44	178.54	197.25	Append to	1220B-18X-1, 0	187.90	206.61
1220B-18X-3, 144	191.66	210.37	Append to	1220B-19X-1, 0	192.40	211.11
1220B-19X-1, 110	193.50	212.21	Append to	1220B-20X-1, 0	197.40	216.11
1220B-20X-2, 92	199.82	218.53				

Note: This table is also available in [ASCII](#).

Table T10. Paleomagnetic events, Site 1220.

Chron/ Subchron	Age (Ma)	Depth (mcd)
T C1n	0.000	0.00
T C6An.1n	20.518	20.16
B C6An.1n	20.725	20.73
T C6An.2n	20.996	21.15
B C6An.2n	21.320	22.00
T C6AAAn	21.768	22.85
B C6AAAn	21.859	23.13
T C6AAr.1n	22.151	23.98
B C6AAr.1n	22.248	24.26
T C6AAr.2n	22.459	24.89
B C6AAr.2n	22.493	25.00
T C6Bn.1n	22.588	25.25
B C6Bn.1n	22.750	25.70
T C6Bn.2n	22.804	25.75
B C6Bn.2n	23.069	26.67
T C6Cn.1n	23.353	27.68
B C6Cn.1n	23.535	28.06
T C6Cn.2n	23.677	28.71
B C6Cn.2n	23.800	28.98
T C6Cn.3n	23.999	29.56
B C6Cn.3n	24.118	29.73
T C7n.1n	24.730	32.11
B C7n.1n	24.781	32.20
T C7n.2n	24.835	32.64
B C7n.2n	25.183	33.78
T C8n.1n	25.823	35.72
B C8n.1n	25.951	36.20
T C8n.2n	25.992	36.28
B C8n.2n	26.554	39.23
T C9n	27.027	41.08
B C9n	27.972	44.05
T C10n.1n	28.283	44.75
B C10n.1n	28.512	46.88
T C10n.2n	28.578	47.16
B C10n.2n	28.745	47.66
T C11n.1n	29.401	53.60
B C11n.1n	29.662	55.72
T C11n.2n	29.765	56.00
B C11n.2n	30.098	57.48
T C12	30.479	59.68
B C12	30.939	61.09
T C13n	33.058	74.79
B C13n	33.545	76.97
T C15n	34.655	82.67
B C15n	34.940	83.70
T C16n.1n	35.343	85.30
B C16n.1n	35.526	86.42
T C16n.2n	35.685	87.15
B C16n.2n	36.341	91.15
T C17n.1n	36.618	92.61
B C17n.1n	37.473	97.45
T C17n.2n	37.604	98.18
B C17n.2n	37.848	99.27
T C17n.3n	37.920	99.64
B C17n.3n	38.113	100.36
T C18n.1n	38.426	101.94
B C18n.1n	39.552	108.85
T C18n.2n	39.631	109.70
B C18n.2n	40.130	114.06
T C19n	41.257	125.05
B C19n	41.521	126.16
T C20n	42.536	131.41
B C20n	43.789	142.32
T C21n	46.264	166.40

Notes: T = top, B = bottom. This table is also available in [ASCII](#).

**Table T11.** Nannofossil, foraminifer, and radiolarian events, Site 1220.

Marker species/ Zonal boundaries	Age (Ma)	Depth (mcd)	± (m)
Nannofossil events:			
T <i>Triquetrorhabdulus carinatus</i> acme*	22.00	25.75	0.65
B <i>Sphenolithus ciproensis</i>	28.10	42.29	0.40
T <i>Sphenolithus pseudoradians</i>	29.10	47.07	0.67
B <i>Sphenolithus distentus</i>	30.40	57.49	0.65
T <i>Reticulofenestra umbilicus</i> ≥14 μm	31.70	68.82	0.35
T <i>Ericsonia formosa</i>	32.90	73.69	0.20
X <i>Tribachiatus contortus</i> / <i>T. orthostylus</i>	53.40	210.26	0.13
B <i>Tribachiatus bramlettei</i>	53.80	214.38	1.94
T <i>Fasciculitius</i> spp.†	54.10	217.14	0.13
X <i>Fasciculitius/Rhomboaster</i> †		217.21	0.05
B <i>Rhomboaster</i> spp.†	54.10	217.49	0.13
Foraminifer events:			
Benthic extinction event	55.00	218.39	0.01
Radiolarian events:			
RN1/RP22	23.62	24.40	0.50
RP22/21	24.60	33.45	0.75
RP21/20	28.80	52.29	1.00
RP20/19	32.80	76.72	0.88
RP19/18	34.90	82.85	0.75
RP18/17	36.40	93.19	0.75
RP17/16	37.70	100.52	0.75
RP16/15	38.80	114.19	0.32
RP15/14	39.50	125.60	0.22
RP14/13	42.80	138.27	0.75
RP13/12	44.50	149.39	0.75
RP12/11	47.50	160.10	1.85
RP11/10	48.50	183.34	5.47
RP10/9	49.00		
RP9/8	50.30	183.34	5.47
RP8/7	52.80	202.98	5.23

Notes: \* = based on Cande and Kent (1995) time scale, 900 k.y. subtracted from age estimates for *T. carinatus* acme. T = top, B = bottom, X = abundance cross-over. † = age estimates in need of revision; events occur 0.77–1.38 m above the P/E boundary (199-1220B-20X-2, 78 cm). This table is also available in [ASCII](#).  
[\[N1\]](#)

**Table T12.** Depths, ages, rates, and fluxes of sediment, Site 1220. (See table notes. Continued on next page.)

Depth (mcd)	Age (Ma)	LSR (m/m.y.)	DBD (g/cm <sup>3</sup> )	MAR (mg/cm <sup>2</sup> /k.y.)	Comments
0.00	0.00				Age/depth control
0.85	0.84	1.02	0.375	38	
2.25	2.21	1.02	0.394	40	
3.75	3.68	1.02	0.425	43	
5.25	5.16	1.02	0.443	45	
6.75	6.63	1.02	0.468	48	
8.25	8.11	1.02	0.493	50	
9.37	9.21	1.02	0.517	53	
9.94	9.77	1.02	0.536	55	
11.75	11.54	1.02	0.483	49	
13.25	13.02	1.02	0.517	53	
14.75	14.49	1.02	0.557	57	
16.25	15.97	1.02	0.547	56	
17.75	17.44	1.02	0.489	50	
18.85	18.52	1.02	0.368	37	
19.79	19.44	1.02	0.270	27	
20.16	20.52				Age/depth control
21.20	20.91	2.66	0.255	68	
22.73	21.48	2.66	0.229	61	
24.14	22.02	2.66	0.465	124	
25.20	22.41	2.66	0.313	83	
26.70	22.98	2.66	0.317	84	
28.20	23.54	2.66	0.251	67	
29.73	24.12				Age/depth control
31.44	24.56	3.91	0.270	106	
33.00	24.95	3.91	0.258	101	
34.50	25.34	3.91	0.313	122	
36.00	25.72	3.91	0.306	120	
37.50	26.11	3.91	0.242	95	
39.00	26.49	3.91	0.285	111	
39.94	26.73	3.91	0.296	116	
42.38	27.35	3.91	0.418	163	
43.54	27.65	3.91	0.533	208	
45.04	28.04	3.91	0.705	276	
46.53	28.42	3.91	0.819	320	
47.16	28.58				Age/depth control
48.16	28.75	5.66	0.745	422	
49.54	29.00	5.66	0.699	396	
50.65	29.19	5.66	0.455	257	
53.59	29.71	5.66	0.747	423	
55.09	29.98	5.66	0.896	507	
56.59	30.24	5.66	0.698	395	
58.09	30.51	5.66	0.977	553	
59.59	30.77	5.66	0.664	376	
61.09	31.04	5.66	0.441	250	
62.12	31.22	5.66	0.694	393	
64.06	31.56	5.66	0.709	401	
65.56	31.83	5.66	0.757	428	
67.02	32.09	5.66	0.787	445	
68.52	32.35	5.66	0.763	432	
70.02	32.62	5.66	0.516	292	
71.52	32.88	5.66	0.526	298	
72.52	33.06	5.66	0.544	308	
74.63	33.43	5.66	0.434	246	
76.39	33.74	5.66	0.835	472	
77.89	34.01	5.66	0.303	171	
79.39	34.27	5.66	0.309	175	
80.89	34.54	5.66	0.335	190	
82.39	34.80	5.66	0.322	182	
83.39	34.98	5.66	0.299	169	
85.04	35.27	5.66	0.304	172	
86.84	35.59	5.66	0.292	165	
88.24	35.84	5.66	0.293	166	
89.74	36.10	5.66	0.298	169	
91.27	36.37	5.66	0.296	167	
92.74	36.63	5.66	0.304	172	
93.79	36.82	5.66	0.298	169	
95.57	37.13	5.66	0.294	166	

Table T12 (continued).

Depth (mcd)	Age (Ma)	LSR (m/m.y.)	DBD (g/cm <sup>3</sup> )	MAR (mg/cm <sup>2</sup> /k.y.)	Comments
97.07	37.40	5.66	0.288	163	
98.57	37.66	5.66	0.348	197	
100.07	37.93	5.66	0.314	178	
101.57	38.19	5.66	0.316	179	
103.07	38.46	5.66	0.315	178	
104.11	38.64	5.66	0.302	171	
105.17	38.83	5.66	0.306	173	
106.67	39.10	5.66	0.310	175	
108.14	39.36	5.66	0.308	174	
109.67	39.63	5.66	0.279	158	
109.70	39.63				Age/depth control
111.17	39.80	8.55	0.285	244	
112.67	39.98	8.55	0.279	238	
113.92	40.12	8.55	0.307	262	
120.12	40.85	8.55	0.297	254	
121.62	41.03	8.55	0.309	264	
123.12	41.20	8.55	0.314	268	
124.62	41.38	8.55	0.310	265	
125.68	41.50	8.55	0.317	271	
126.12	41.55	8.55	0.336	287	
127.18	41.68	8.55	0.293	250	
127.62	41.73	8.55	0.317	271	
128.66	41.85	8.55	0.341	291	
128.68	41.85	8.55	0.315	269	
130.18	42.03	8.55	0.314	268	
131.68	42.20	8.55	0.322	275	
133.18	42.38	8.55	0.312	267	
134.88	42.58	8.55	0.338	289	
136.38	42.75	8.55	0.312	267	
137.82	42.92	8.55	0.313	268	
139.32	43.10	8.55	0.306	262	
140.82	43.27	8.55	0.336	287	
142.32	43.45	8.55	0.324	277	
143.54	43.59	8.55	0.323	276	
148.94	44.22	8.55	0.320	274	
150.44	44.40	8.55	0.315	269	
151.94	44.57	8.55	0.341	291	
153.44	44.75	8.55	0.342	292	
154.94	44.92	8.55	0.350	299	
156.44	45.10	8.55	0.361	309	
157.59	45.23	8.55	0.360	308	
159.99	45.51	8.55	0.342	292	
161.49	45.69	8.55	0.364	311	
162.96	45.86	8.55	0.346	296	
164.46	46.04	8.55	0.378	323	
165.96	46.21	8.55	0.376	321	
166.40	46.26				Age/depth control
167.53	46.46	5.84	0.406	237	
168.71	46.66	5.84	0.363	212	
169.21	46.75	5.84	0.342	200	
169.46	46.79	5.84	0.528	308	
188.08	49.98	5.84	0.347	202	
190.12	50.33	5.84	0.324	189	
191.57	50.58	5.84	0.301	176	
193.20	50.85	5.84	0.298	174	
196.27	51.38	5.84	0.314	183	
207.37	53.28	5.84	0.635	371	
208.75	53.52	5.84	0.690	403	
209.96	53.73	5.84	0.716	418	
211.65	54.02	5.84	1.096	640	
217.40	55.00				Age/depth control

Notes: LSR = linear sedimentation rate, DBD = dry bulk density, MAR = mass accumulation rate. This table is also available in [ASCII](#).

**Table T13.** Interstitial water data, Holes 1220A and 1220B.

Core, section, interval (cm)	Depth (mbsf)	pH	Alkalinity (mM)	Salinity	Cl (mM)	Na (mM)	K (mM)	Ca (mM)	Mg (mM)	SO <sub>4</sub> (mM)	NH <sub>4</sub> (μM)	H <sub>4</sub> SiO <sub>4</sub> (μM)	Sr (μM)	Li (μM)	Mn (μM)	Ba (μM)	B (μM)
199-1220A-																	
1H-3, 145-150	4.45	7.14	2.62	35.0	554	477	12.4	10.7	51.5	28.7	2.9	556	82	27	27	0.20	525
2H-3, 145-150	13.95	7.14	3.11	35.0	556	477	12.8	10.9	52.6	28.7	4.4	550	81	28	BD	0.45	577
3H-3, 145-150	23.40	7.37	3.10	35.0	560	473	12.3	11.8	56.2	29.1	1.5	512	88	28	BD	0.47	482
4H-3, 145-150	32.95	7.36	3.01	35.0	563	483	11.6	11.4	53.3	29.0	2.9	558	85	27	BD	0.20	497
5H-3, 145-150	42.45	7.27	3.00	35.0	565	484	11.9	11.3	53.6	29.0	0.0	596	87	28	BD	0.34	505
6H-3, 145-150	51.95	7.25	2.69	35.0	563	482	11.5	10.9	53.8	28.8	1.5	616	84	27	BD	0.31	498
9H-3, 145-150	80.45	7.34	3.24	35.5	566	487	11.6	11.4	53.1	29.0		678	88	25	BD	0.20	471
12H-4, 145-150	110.45	7.23	3.03	35.5	562	477	11.6	11.7	54.7	28.1	2.9	868	88	25	BD	0.47	481
199-1220B-																	
10H-3, 145-150	125.89	7.30	3.04	35.5	563	469	11.3	12.2	59.0	28.3	1.5	810	89	24	BD	0.55	446
13H-3, 145-150	154.45	7.20	3.22	35.5	563	478	10.7	12.0	54.2	27.6	2.9	934	88	25	BD	0.23	455
16X-3, 145-150	173.55	7.39	3.45	35.5	562	476	11.2	13.1	55.0	28.9	2.9	880	88	21	BD	BD	423

Notes: BD = below detection level. This table is also available in [ASCII](#).

Table T14. Bulk sediment data, Holes 1220A and 1220B. (See table notes. Continued on next page.)

Core, section, interval (cm)	Depth		Si (wt%)	Al (wt%)	Ti (wt%)	Fe (wt%)	Mn (wt%)	Ca (wt%)	Mg (wt%)	P (wt%)	Sr (ppm)	Ba (ppm)
	(mbsf)	(mcd)										
199-1220A-												
1H-2, 74-75	2.24	2.24	26.45	6.80	0.30	4.59	0.29	0.69	2.10	0.09	160.75	7,404.83
1H-4, 74-75	5.24	5.24	23.52	6.91	0.44	4.67	0.15	0.84	1.98	0.16	246.87	8,170.25
1H-6, 74-75	8.24	8.24	19.44	5.50	0.38	3.49	1.14	1.58	1.97	0.34	450.28	3,242.23
2H-2, 73-74	11.73	11.73	27.45	7.54	0.39	4.18	1.34	1.43	1.98	0.35	286.24	6,947.68
2H-4, 73-74	14.73	14.73	23.04	6.06	0.33	5.21	0.97	1.18	1.57	0.33	241.60	2,233.18
2H-6, 73-74	17.73	17.73	17.66	5.47	0.31	4.76	0.87	0.91	1.67	0.17	323.66	1,991.94
3H-2, 73-74	21.18	21.18	27.84	5.22	0.22	3.17	0.72	1.16	1.78	0.27	374.06	6,969.11
3H-4, 73-74	24.18	24.18	8.38	1.58	0.05	1.24	0.35	24.91	0.81	0.11	1,909.16	3,478.26
4H-4, 73-74	33.73	35.98	19.56	2.97	0.14	2.72	0.69	9.93	1.60	0.22	705.76	6,430.08
4H-6, 73-74	36.73	38.98	21.69	3.32	0.17	3.40	0.74	7.42	1.95	0.24	812.18	2,280.11
5H-2, 73-74	40.23	43.52	8.67	1.71	0.08	1.52	0.26	31.51	0.80	0.14	1,413.15	2,208.94
5H-4, 78-79	43.28	46.57	4.23	0.80	0.04	0.68	0.10	36.66*	0.40	0.07	1,732.60	1,024.83
5H-6, 73-74	46.23	49.52	6.78	0.95	0.05	0.95	0.15	33.23	0.48	0.09	1,547.45	1,501.07
6H-2, 73-74	49.73	55.07	3.79	0.40	0.02	0.41	0.09	39.37*	0.33	0.05	1,526.54	1,266.38
6H-4, 73-74	52.73	58.07	2.94	0.36	BD	0.11	0.07	30.67	0.23	0.05	1,489.84	843.28
6H-6, 73-74	55.73	61.07	16.52	2.46	0.12	2.19	0.40	18.98	1.24	0.38	1,024.10	3,643.34
7H-2, 74-75	59.24	65.55	7.57	0.40	0.01	0.15	0.06	32.41	0.30	0.10	1,470.41	1,335.65
7H-4, 74-75	62.20	68.51	3.79	0.56	BD	0.31	0.07	35.02	0.33	0.05	2,113.56	2,132.76
7H-6, 74-75	65.20	71.51	15.31	0.80	BD	0.55	0.11	24.75	0.49	0.06	1,104.05	2,507.04
8H-2, 75-77	68.75	76.39	3.54	0.53	0.02	0.25	0.10	35.84	0.30	0.07	1,869.88	1,037.18
8H-4, 75-77	71.75	79.39	26.17	1.78	0.09	1.67	0.27	0.63	1.08	0.31	172.92	4,198.70
8H-6, 75-77	74.75	82.39	31.66	2.36	0.12	2.54	0.35	0.88	1.30	0.27	213.31	5,463.71
9H-2, 84-85	78.34	86.83	32.25	2.06	0.09	2.21	0.36	0.23	1.12	0.20	232.24	6,321.09
9H-4, 73-74	81.23	89.72	23.16	1.67	0.06	2.54	0.36	0.61	1.22	0.18	224.80	6,806.39
9H-6, 73-74	84.23	92.72	28.57	1.26	0.04	2.23	0.37	0.50	1.18	0.18	212.29	3,949.70
10H-2, 74-75	87.74	97.06	27.74	1.72	0.06	3.57	0.54	0.64	1.43	0.18	273.35	5,813.85
10H-4, 74-75	90.74	100.06	30.30	2.16	0.09	4.18	0.61	0.67	1.45	0.33	200.51	5,089.47
10H-6, 74-75	93.74	103.06	20.63	1.07	0.03	3.19	0.52	0.37	1.22	0.16	254.09	13,102.58
11H-2, 74-75	97.24	106.66	31.11	1.10	0.05	2.65	0.46	0.25	1.14	0.20	115.81	3,558.76
11H-4, 74-75	100.24	109.66	33.51	0.86	0.01	2.15	0.49	0.22	1.03	0.12	96.52	4,076.52
11H-6, 74-75	103.24	112.66	30.08	0.80	0.01	2.37	0.47	0.08	0.96	0.08	154.49	2,781.93
12H-2, 73-74	106.73	121.60	33.07	0.94	0.05	1.52	0.31	BD	0.86	0.13	142.72	4,412.35
12H-6, 73-74	112.73	127.60	32.91	0.88	0.04	1.71	0.33	0.38	0.93	0.20	118.31	3,338.35
199-1220B-												
9H-2, 73-74	114.23	127.16	31.18	1.23	0.07	1.87	0.31	0.35	0.95	0.23	119.70	3,172.58
9H-4, 73-74	117.23	130.16	33.31	1.00	0.05	2.13	0.38	0.40	1.04	0.26	147.74	4,261.21
9H-6, 73-74	120.23	133.16	33.59	0.82	0.03	1.50	0.26	0.39	0.82	0.25	132.85	4,433.53
10H-2, 73-74	123.73	136.36	33.52	0.64	0.03	1.36	0.28	0.24	0.81	0.20	152.78	5,223.47
10H-4, 73-74	126.67	139.30	32.36	0.57	0.02	1.19	0.22	0.03	0.80	0.17	115.44	4,181.60
10H-6, 73-74	129.67	142.30	34.38	0.59	0.02	1.53	0.32	0.05	0.81	0.13	127.99	5,048.51
11H-4, 74-75	136.24	153.43	31.44	0.62	0.03	1.96	0.41	0.21	0.92	0.20	171.38	6,041.41
11H-6, 74-75	139.24	156.43	31.31	0.74	0.04	2.14	0.46	0.19	0.90	0.16	172.36	6,135.70
12H-2, 77-78	142.77	161.48	31.96	0.71	0.04	2.56	0.60	0.21	0.97	0.24	152.75	5,184.99
12H-4, 73-74	145.73	164.44	35.53	0.80	0.01	2.60	0.53	0.44	1.01	0.18	161.93	5,948.36
12H-6, 81-82	148.81	167.52	31.99	0.87	0.04	3.25	0.69	0.32	1.15	0.23	171.50	6,555.40
13H-1, 49-50	150.49	169.20	35.42	0.57	BD	1.37	0.22	0.65	0.71	0.18	130.00	4,840.22
16X-2, 80-81	171.40	190.11	39.10	0.69	0.01	0.92	0.19	0.35	0.68	0.09	120.43	3,975.64
16X-4, 87-88	174.47	193.18	30.58	0.45	0.03	0.91	0.12	BD	0.55	0.08	92.52	3,803.49
16X-6, 94-95	177.54	196.25	33.83	0.55	0.03	1.00	0.19	0.03	0.85	0.17	131.40	4,488.98
18X-2, 73-74	190.13	208.84	12.12	0.27	BD	0.30	0.05	26.41	0.62	0.07	611.31	3,792.24
19X-1, 74-75	193.14	211.85	2.44	0.30	BD	0.21	0.06	34.95	0.84	0.04	1,031.44	4,511.35
20X-2, 0-4	198.90	217.61	2.14	0.39	BD	0.55	0.09	36.07*	0.68	0.08	1,097.59	4,926.41
20X-2, 4-11	198.94	217.65	2.44	0.48	0.03	0.70	0.07	37.78*	0.71	0.09	929.11	4,852.99
20X-2, 11-18	199.01	217.72	3.06	0.57	0.01	0.59	0.08	33.73	0.95	0.15	829.87	4,933.68
20X-2, 18-25	199.08	217.79	2.92	0.60	0.04	0.59	0.07	38.11*	0.99	0.11	541.64	716.09
20X-2, 25-32	199.15	217.86	3.01	0.73	0.04	0.59	0.06	36.81*	1.05	0.10	418.18	451.02
20X-2, 32-39	199.22	217.93	2.64	0.58	0.01	0.37	0.07	36.50*	0.95	0.11	424.68	665.37
20X-2, 39-41	199.29	218.00	3.54	0.67	0.01	0.40	0.06	33.78	0.92	0.13	352.24	1,042.40
20X-2, 41-43	199.31	218.02	3.43	0.74	0.03	0.50	0.08	40.22*	1.13	0.15	377.44	1,355.41
20X-2, 43-45	199.33	218.04	3.31	0.69	0.04	0.56	0.10	39.40*	1.01	0.18	342.77	1,791.47
20X-2, 45-47	199.35	218.06	4.23	1.03	0.06	0.72	0.09	35.45	1.06	0.14	363.03	2,621.80
20X-2, 47-54	199.37	218.08	17.77	4.08	0.17	2.84	0.36	13.25	2.71	0.58	427.11	1,1063.46
20X-2, 52-54	199.42	218.13	20.02	5.49	0.31	3.88	0.38	7.91	3.12	0.72	516.99	1,3633.33
20X-2, 54-61	199.44	218.15	17.17	4.02	0.23	3.07	1.59	13.85	3.42	0.67	526.37	1,2970.81
20X-2, 58-60	199.48	218.19	20.30	4.57	0.21	3.74	0.71	8.27	3.64	0.73	596.54	1,6334.15
20X-2, 60-63	199.50	218.21	16.25	3.74	0.23	2.96	9.05	6.78	3.39	0.28	314.03	6745.25

**Table T14 (continued).**

Core, section, interval (cm)	Depth		Si (wt%)	Al (wt%)	Ti (wt%)	Fe (wt%)	Mn (wt%)	Ca (wt%)	Mg (wt%)	P (wt%)	Sr (ppm)	Ba (ppm)
	(mbsf)	(mcd)										
20X-2, 65-67	199.55	218.26	20.46	4.94	0.42	3.09	0.32	6.47	3.75	0.11	163.66	1032.89
20X-2, 67-69	199.57	218.28	20.22	4.63	0.32	2.84	0.21	6.93	3.65	0.25	237.22	4072.30
20X-2, 69-71	199.59	218.30	18.86	4.24	0.27	5.46	0.36	7.64	3.57	1.48	824.50	22,711.96
20X-2, 75-77	199.65	218.36	18.31	3.74	0.28	6.67	0.04	8.89	3.46	1.04	449.33	12,708.96
20X-2, 77-79	199.67	218.38	9.96	1.75	0.05	1.98	0.13	22.69	1.78	0.31	557.20	8,092.87
20X-2, 79-81	199.69	218.40	5.32	1.06	0.05	1.30	0.02	34.92	1.27	0.28	589.95	872.96
20X-2, 81-83	199.71	218.42	3.72	0.71	0.04	0.80	0.02	37.52*	0.95	0.21	641.60	55.07
20X-2, 83-85	199.73	218.44	3.25	0.65	0.01	0.71	0.03	34.01	1.01	0.22	667.01	158.21
20X-2, 85-87	199.75	218.46	3.24	0.58	0.04	0.79	0.03	36.66*	0.91	0.19	668.54	464.71
20X-2, 87-89	199.77	218.48	3.02	0.59	0.03	0.77	0.02	36.78*	0.90	0.18	711.88	530.48
20X-2, 89-91	199.79	218.50	2.56	0.60	0.05	0.87	0.02	32.64	0.85	0.14	820.17	1,755.87

Notes: BD = below detection level. \* = Ca values higher than 35.9 wt% are out of the range of the standards (see "Geochemistry," p. 20, in the "Explanatory Notes" chapter). This table is also available in ASCII. [N1]

**Table T15.** CaCO<sub>3</sub> and C<sub>org</sub> data, Holes 1220A and 1220B.

Core, section, interval (cm)	Depth (mbsf)	Depth (mcd)	CaCO <sub>3</sub> (wt%)	Organic C (wt%)	CaCO <sub>3</sub> (wt%)*
199-1220A-					
1H-2, 74-75	2.24	2.24	0.29		-0.17
1H-4, 74-75	5.24	5.24	0.29	0.11	0.22
1H-6, 74-75	8.24	8.24	0.55		2.11
2H-2, 73-74	11.73	11.73	0.64		1.73
2H-4, 73-74	14.73	14.73	0.39	0.03	1.09
2H-6, 73-74	17.73	17.73	0.39		0.41
3H-2, 73-74	21.18	21.18	0.90		0.97
3H-4, 73-74	24.18	24.18	57.91	-0.32	61.45
4H-4, 73-74	33.73	35.98	17.61	-0.15	23.30
4H-6, 73-74	36.73	38.98	11.52		16.90
5H-2, 73-74	40.23	43.52	63.01		78.24
5H-4, 78-79	43.28	46.57	82.17	-0.26	91.36 <sup>†</sup>
5H-6, 73-74	46.23	49.52	72.79		82.64
6H-2, 73-74	49.73	55.07	84.84		98.26 <sup>†</sup>
6H-4, 73-74	52.73	58.07	87.98	-0.19	76.14
6H-6, 73-74	55.73	61.07	38.99		46.36
7H-2, 74-75	59.24	65.55	76.16		80.55
7H-4, 74-75	62.20	68.51	78.40	-0.13	87.19
7H-6, 74-75	65.20	71.51	52.86		61.04
8H-2, 75-77	68.75	76.39			89.28
8H-4, 75-77	71.75	79.39			-0.34
8H-6, 75-77	74.75	82.39			0.30
9H-2, 84-85	78.34	86.83	0.78		-1.38
9H-4, 73-74	81.23	89.72	0.84	-0.06	-0.39
9H-6, 73-74	84.23	92.72	1.08		-0.67
10H-2, 74-75	87.74	97.06	0.91		-0.32
10H-4, 74-75	90.74	100.06	0.81	-0.05	-0.24
10H-6, 74-75	93.74	103.06	0.72		-1.00
11H-2, 74-75	97.24	106.66	0.69		-1.32
11H-4, 74-75	100.24	109.66	0.80	-0.08	-1.41
11H-6, 74-75	103.24	112.66	0.66		-1.76
12H-2, 73-74	106.73	121.60	0.67		
12H-6, 73-74	112.73	127.60	0.74		-0.99
199-1220B-					
9H-2, 73-74	114.23	127.16	0.67		-1.06
9H-4, 73-74	117.23	130.16	0.24	0.05	-0.94
9H-6, 73-74	120.23	133.16	0.24		-0.96
10H-2, 73-74	123.73	136.36	0.20		-1.35
10H-4, 73-74	126.67	139.30	0.21	-0.02	-1.88
10H-6, 73-74	129.67	142.30	0.17		-1.82
11H-4, 74-75	136.24	153.43	0.15	0.00	-1.41
11H-6, 74-75	139.24	156.43	0.20		-1.46
12H-2, 77-78	142.77	161.48	0.20		-1.41
12H-4, 73-74	145.73	164.44	0.22	-0.02	-0.81
12H-6, 81-82	148.81	167.52	0.18		-1.12
13H-1, 49-50	150.49	169.20	0.23	-0.01	-0.30
16X-2, 80-81	171.40	190.11	0.19		-1.05
16X-4, 87-88	174.47	193.18	0.22	-0.01	
16X-6, 94-95	177.54	196.25	0.23		-1.87
18X-2, 73-74	190.13	208.84	61.37	-0.14	65.28
19X-1, 74-75	193.14	211.85	86.86	-0.24	87.03

Notes: \* = calculated from Ca (wt%). † = CaCO<sub>3</sub> values higher than 90 wt% are calculated from Ca values out of the range of the standards (see "Geochemistry," p. 20, in the "Explanatory Notes" chapter). This table is also available in [ASCII](#).

**Table T16. Moisture and density measurements, Hole 1220A.**

Core, section, interval (cm)	Depth (mbsf)	Water content (%)	Density (g/cm <sup>3</sup> )				Porosity (%)	Core, section, interval (cm)	Depth (mbsf)	Water content (%)	Density (g/cm <sup>3</sup> )			Porosity (%)
			Wet bulk	Dry bulk	Grain	Wet bulk					Dry bulk	Grain		
199-1220A-							10H-2, 75-77	87.75	75.6	1.18	0.29	2.20	86.9	
1H-1, 85-87	0.85	69.9	1.25	0.38	2.52	85.1	10H-3, 75-77	89.25	71.4	1.22	0.35	2.27	84.7	
1H-2, 75-77	2.25	68.3	1.24	0.39	2.29	82.8	10H-4, 75-77	90.75	73.7	1.20	0.31	2.27	86.1	
1H-3, 75-77	3.75	66.2	1.26	0.43	2.27	81.3	10H-5, 75-77	92.25	73.4	1.19	0.32	2.14	85.2	
1H-4, 75-77	5.25	65.1	1.27	0.44	2.28	80.6	10H-6, 75-77	93.75	73.5	1.19	0.32	2.18	85.5	
1H-5, 75-77	6.75	64.3	1.31	0.47	2.67	82.5	10H-7, 29-31	94.79	74.6	1.19	0.30	2.28	86.7	
1H-6, 75-77	8.25	63.0	1.33	0.49	2.75	82.1	11H-1, 75-77	95.75	74.3	1.19	0.31	2.24	86.3	
1H-7, 37-39	9.37	61.3	1.34	0.52	2.60	80.1	11H-2, 75-77	97.25	73.9	1.19	0.31	2.15	85.6	
2H-1, 44-46	9.94	59.9	1.34	0.54	2.45	78.1	11H-3, 72-74	98.72	73.9	1.18	0.31	2.06	85.1	
2H-2, 75-77	11.75	62.7	1.30	0.48	2.33	79.3	11H-4, 75-77	100.25	76.1	1.17	0.28	2.14	87.0	
2H-3, 75-77	13.25	61.1	1.33	0.52	2.51	79.4	11H-5, 75-77	101.75	75.7	1.18	0.29	2.17	86.9	
2H-4, 75-77	14.75	58.9	1.36	0.56	2.54	78.0	11H-6, 75-77	103.25	76.1	1.17	0.28	2.15	87.0	
2H-5, 75-77	16.25	59.4	1.35	0.55	2.51	78.2	11H-7, 50-52	104.50	73.9	1.18	0.31	2.03	84.8	
2H-6, 75-77	17.75	62.7	1.31	0.49	2.48	80.3	12H-1, 75-77	105.25	74.9	1.19	0.30	2.24	86.7	
2H-7, 35-37	18.85	69.7	1.21	0.37	2.11	82.6	12H-2, 75-77	106.75	74.1	1.19	0.31	2.24	86.2	
3H-1, 79-81	19.79	77.1	1.18	0.27	2.43	88.9	12H-3, 75-77	108.25	73.6	1.19	0.31	2.16	85.5	
3H-2, 75-77	21.20	78.2	1.17	0.26	2.40	89.4	12H-4, 75-77	109.75	74.0	1.19	0.31	2.25	86.2	
3H-3, 78-80	22.73	80.2	1.16	0.23	2.40	90.5	12H-5, 75-77	111.25	72.2	1.21	0.34	2.24	85.0	
3H-4, 69-71	24.14	64.5	1.31	0.47	2.66	82.5	12H-6, 75-77	112.75	73.6	1.20	0.32	2.28	86.1	
3H-5, 75-77	25.20	74.0	1.21	0.31	2.44	87.2	12H-7, 29-30	113.79	71.8	1.21	0.34	2.28	85.0	
3H-6, 75-77	26.70	73.7	1.21	0.32	2.42	86.9	199-1220B-							
3H-7, 75-77	28.20	78.4	1.16	0.25	2.31	89.1	9H-1, 75-77	112.75	73.3	1.19	0.32	2.10	84.9	
4H-1, 69-71	29.19	77.0	1.17	0.27	2.30	88.2	9H-2, 75-77	114.25	75.2	1.18	0.29	2.21	86.7	
4H-2, 75-77	30.75	78.0	1.17	0.26	2.45	89.4	9H-3, 75-77	115.75	73.5	1.19	0.32	2.14	85.3	
4H-3, 75-77	32.25	74.0	1.21	0.31	2.43	87.1	9H-4, 75-77	117.25	73.6	1.19	0.31	2.18	85.6	
4H-4, 75-77	33.75	74.9	1.22	0.31	2.79	89.0	9H-5, 75-77	118.75	73.2	1.20	0.32	2.29	85.9	
4H-5, 75-77	35.25	79.2	1.16	0.24	2.43	90.0	9H-6, 75-77	120.25	73.7	1.19	0.31	2.13	85.4	
4H-6, 75-77	36.75	76.0	1.19	0.29	2.42	88.2	10H-1, 75-77	122.25	72.0	1.21	0.34	2.20	84.7	
4H-7, 19-21	37.69	75.2	1.20	0.30	2.42	87.8	10H-2, 75-77	123.75	73.8	1.19	0.31	2.23	86.0	
5H-1, 109-111	39.09	67.3	1.28	0.42	2.64	84.2	10H-3, 75-77	125.19	73.7	1.19	0.31	2.16	85.5	
5H-2, 75-77	40.25	60.5	1.35	0.53	2.64	79.8	10H-4, 75-77	126.69	74.1	1.18	0.31	2.12	85.6	
5H-3, 75-77	41.75	51.8	1.46	0.71	2.69	73.8	10H-5, 75-77	128.19	72.1	1.21	0.34	2.21	84.8	
5H-4, 74-76	43.24	46.6	1.54	0.82	2.72	69.9	10H-6, 75-77	129.69	73.1	1.20	0.32	2.27	85.7	
5H-5, 87-89	44.87	49.8	1.49	0.75	2.70	72.4	10H-7, 47-49	130.91	73.0	1.20	0.32	2.20	85.3	
5H-6, 75-77	46.25	52.0	1.46	0.70	2.70	74.1	11H-1, 75-77	131.75	73.2	1.19	0.32	2.15	85.1	
5H-7, 36-38	47.36	65.0	1.30	0.46	2.59	82.5	11H-2, 75-77	133.25	73.6	1.19	0.32	2.23	85.9	
6H-1, 75-77	48.25	49.8	1.49	0.75	2.71	72.4	11H-3, 75-77	134.75	71.9	1.21	0.34	2.28	85.0	
6H-2, 75-77	49.75	43.3	1.58	0.90	2.71	66.9	11H-4, 75-77	136.25	71.6	1.21	0.34	2.17	84.2	
6H-3, 75-77	51.25	52.1	1.46	0.70	2.68	74.0	11H-5, 75-77	137.75	71.1	1.21	0.35	2.21	84.2	
6H-4, 75-77	52.75	40.3	1.64	0.98	2.74	64.3	11H-6, 75-77	139.25	70.4	1.22	0.36	2.23	83.8	
6H-5, 75-77	54.25	53.7	1.43	0.66	2.68	75.2	11H-7, 40-42	140.40	70.5	1.22	0.36	2.25	84.0	
6H-6, 75-77	55.75	65.8	1.29	0.44	2.58	82.9	12H-1, 78-80	141.28	71.7	1.21	0.34	2.21	84.5	
6H-7, 28-30	56.78	52.2	1.45	0.69	2.68	74.1	12H-2, 78-80	142.78	70.2	1.22	0.36	2.21	83.6	
7H-1, 75-77	57.75	51.4	1.46	0.71	2.66	73.3	12H-3, 75-77	144.25	71.4	1.21	0.35	2.17	84.1	
7H-2, 75-77	59.25	49.0	1.49	0.76	2.62	71.1	12H-4, 75-77	145.75	69.4	1.24	0.38	2.33	83.7	
7H-3, 75-77	60.71	47.5	1.50	0.79	2.59	69.6	12H-5, 75-77	147.25	69.4	1.23	0.38	2.25	83.3	
7H-4, 75-77	62.21	48.5	1.48	0.76	2.55	70.0	12H-6, 82-84	148.82	67.5	1.25	0.41	2.28	82.2	
7H-5, 75-77	63.71	61.2	1.33	0.52	2.51	79.4	12H-7, 50-52	150.00	70.2	1.22	0.36	2.21	83.6	
7H-6, 75-77	65.21	60.3	1.32	0.53	2.39	77.9	13H-1, 50-52	150.50	71.8	1.21	0.34	2.30	85.1	
7H-7, 25-27	66.21	59.4	1.34	0.54	2.44	77.7	13H-1, 75-77	150.75	60.5	1.34	0.53	2.50	78.9	
8H-1, 49-51	66.99	66.1	1.28	0.43	2.51	82.7	15X-CC, 0-2	159.50	7.9	2.12	1.95	2.33	16.4	
8H-2, 75-77	68.75	46.0	1.55	0.84	2.74	69.5	16X-1, 27-29	169.37	71.3	1.21	0.35	2.16	84.0	
8H-3, 75-77	70.25	74.6	1.19	0.30	2.33	87.0	16X-2, 81-83	171.41	72.9	1.19	0.32	2.15	84.9	
8H-4, 75-77	71.75	74.0	1.19	0.31	2.20	86.0	16X-3, 76-78	172.86	74.6	1.18	0.30	2.17	86.1	
8H-5, 75-77	73.25	72.2	1.21	0.34	2.23	85.0	16X-4, 89-91	174.49	74.7	1.18	0.30	2.17	86.2	
8H-6, 75-77	74.75	73.1	1.20	0.32	2.26	85.7	16X-6, 96-98	177.56	73.6	1.19	0.31	2.16	85.4	
8H-7, 25-27	75.75	74.8	1.19	0.30	2.29	86.9	17X-CC, 4-6	178.34	8.5	2.10	1.92	2.33	17.4	
9H-1, 55-57	76.55	74.4	1.19	0.30	2.18	86.1	18X-1, 76-78	188.66	54.6	1.40	0.64	2.50	74.6	
9H-2, 85-87	78.35	75.3	1.18	0.29	2.22	86.9	18X-2, 64-66	190.04	52.0	1.44	0.69	2.56	73.0	
9H-3, 75-77	79.75	75.2	1.18	0.29	2.18	86.6	18X-3, 103-105	191.25	50.6	1.45	0.72	2.54	71.8	
9H-4, 75-77	81.25	74.8	1.18	0.30	2.21	86.5	19X-1, 0-2	192.40	2.3	2.52	2.46	2.61	5.7	
9H-5, 78-80	82.78	74.8	1.18	0.30	2.09	85.8	19X-1, 54-56	192.94	35.8	1.71	1.10	2.72	59.7	
9H-6, 75-77	84.25	74.2	1.18	0.30	2.11	85.6								
9H-7, 30-32	85.30	74.7	1.18	0.30	2.15	86.1								
10H-1, 75-77	86.25	75.2	1.18	0.29	2.25	86.9								

Note: This table is also available in [ASCII](#).

Table T17. LAS-based mineralogy, Holes 1220A and 1220B. (See table notes. Continued on next page.)

Core, section, interval (cm)	Depth (mbsf)	Calcite (model wt%)	Opal (model wt%)	Smectite (model wt%)	Illite (model wt%)	Core, section, interval (cm)	Depth (mbsf)	Calcite (model wt%)	Opal (model wt%)	Smectite (model wt%)	Illite (model wt%)
199-1220A-						5H-6, 75-77	46.26	81.72	0.00	18.28	0.00
1H-1, 85-87	0.86	0.00	29.19	62.86	7.95	5H-7, 23-25	47.24	71.41	17.94	4.25	6.40
1H-1, 123-125	1.24	0.00	31.23	68.77	0.00	5H-7, 36-38	47.37	61.88	19.79	18.32	0.00
1H-2, 23-25	1.74	0.00	30.36	69.64	0.00	6H-1, 75-77	48.26	72.79	0.00	27.21	0.00
1H-2, 75-77	2.26	0.00	15.39	84.61	0.00	6H-1, 123-125	48.74	85.08	0.00	9.43	5.49
1H-3, 23-25	3.24	0.00	32.14	67.86	0.00	6H-2, 23-25	49.24	83.76	0.00	11.03	5.21
1H-3, 75-77	3.76	10.42	0.00	89.57	0.01	6H-2, 75-77	49.76	78.47	0.00	21.53	0.00
1H-4, 23-25	4.74	0.00	11.75	88.25	0.00	6H-3, 23-25	50.74	59.96	22.63	8.28	9.12
1H-4, 75-77	5.26	0.00	23.06	76.94	0.00	6H-3, 75-77	51.26	83.69	3.08	11.39	1.85
1H-5, 23-25	6.24	5.11	0.00	94.89	0.00	6H-4, 23-25	52.24	86.70	0.00	6.57	6.73
1H-5, 75-77	6.76	27.27	0.00	62.52	10.21	6H-4, 75-77	52.76	77.88	0.00	22.12	0.00
1H-6, 23-25	7.74	0.00	6.42	93.58	0.00	6H-5, 23-25	53.74	85.09	2.44	4.26	8.20
1H-6, 75-77	8.26	21.73	0.00	78.27	0.00	6H-5, 75-77	54.26	81.40	1.25	16.05	1.29
1H-7, 23-25	9.24	0.00	0.00	100.00	0.00	6H-6, 23-25	55.24	42.98	21.41	21.01	14.59
1H-7, 37-39	9.38	14.38	0.00	85.62	0.00	6H-6, 75-77	55.76	61.73	23.11	12.98	2.18
2H-1, 44-46	9.95	16.14	0.00	83.86	0.00	6H-7, 23-25	56.74	78.17	10.84	0.00	11.00
2H-1, 123-125	10.74	5.56	0.00	94.44	0.00	6H-7, 28-30	56.89	77.30	6.80	15.91	0.00
2H-2, 23-25	11.24	6.60	0.00	93.40	0.00	7H-1, 75-77	57.76	78.46	10.95	9.00	1.59
2H-2, 75-77	11.76	16.05	0.00	83.95	0.00	7H-1, 123-125	58.24	77.39	7.86	8.70	6.05
2H-3, 23-25	12.74	5.78	0.00	94.22	0.00	7H-2, 23-25	58.74	79.00	10.89	3.48	6.63
2H-3, 75-77	13.26	21.89	0.00	78.11	0.00	7H-2, 75-77	59.26	74.88	12.02	13.06	0.04
2H-4, 23-25	14.24	4.59	10.96	84.45	0.00	7H-3, 23-25	60.20	81.34	2.88	9.77	6.01
2H-4, 75-77	14.76	13.40	4.26	82.35	0.00	7H-3, 75-77	60.72	75.11	8.83	16.07	0.00
2H-5, 23-25	15.74	7.61	10.95	81.44	0.00	7H-4, 23-25	61.70	80.95	10.31	0.00	8.74
2H-5, 75-77	16.26	12.51	0.00	85.94	1.56	7H-4, 75-77	62.22	75.20	9.47	12.11	3.23
2H-6, 23-25	17.24	0.00	8.52	91.48	0.00	7H-5, 23-25	63.20	63.41	30.76	2.50	3.34
2H-6, 75-77	17.76	3.34	0.00	96.66	0.00	7H-5, 75-77	63.72	52.75	32.36	14.89	0.00
2H-7, 23-25	18.74	0.00	11.51	88.49	0.00	7H-6, 23-25	64.70	59.02	35.38	5.39	0.21
2H-7, 35-37	18.86	0.00	2.96	97.04	0.00	7H-6, 75-77	65.22	50.07	34.08	15.86	0.00
3H-1, 79-81	19.80	17.03	9.50	68.74	4.73	7H-7, 2-4	65.99	60.35	30.37	9.28	0.00
3H-1, 123-125	20.24	36.41	4.01	30.76	28.82	7H-7, 25-27	66.22	48.44	36.23	15.32	0.00
3H-2, 23-25	20.68	31.61	20.55	28.63	19.22	8H-1, 49-51	67.00	54.37	35.24	10.38	0.00
3H-2, 75-77	21.20	21.89	26.07	42.47	9.58	8H-2, 75-77	68.76	83.20	0.00	14.09	2.71
3H-3, 23-25	22.18	30.68	26.35	22.23	20.74	8H-3, 75-77	70.26	12.20	53.73	32.61	1.46
3H-3, 78-80	22.73	23.80	20.61	55.32	0.28	8H-4, 75-77	71.76	27.82	30.16	27.78	14.24
3H-4, 23-25	23.68	36.29	19.68	30.87	13.16	8H-5, 75-77	73.26	11.91	55.58	28.33	4.18
3H-4, 69-71	24.14	68.67	8.60	22.72	0.00	8H-6, 75-77	74.76	16.54	44.15	32.79	6.52
3H-5, 23-25	24.68	74.09	14.69	1.91	9.31	8H-7, 25-27	75.76	25.81	33.01	27.69	13.49
3H-5, 75-77	25.20	32.41	31.46	36.13	0.00	9H-1, 55-57	76.56	23.59	40.30	21.70	14.40
3H-6, 23-25	26.18	59.31	26.34	14.35	0.00	9H-1, 123-125	77.24	12.67	48.97	33.11	5.25
3H-6, 75-77	26.70	37.59	33.75	28.66	0.00	9H-2, 35-37	77.86	11.71	49.85	32.08	6.36
3H-7, 23-25	27.68	18.70	35.57	37.90	7.84	9H-2, 85-87	78.36	14.47	47.75	33.67	4.11
3H-7, 75-77	28.20	15.83	40.90	43.27	0.00	9H-3, 23-25	79.24	13.67	49.82	32.39	4.13
4H-1, 69-71	29.20	13.20	39.64	47.00	0.16	9H-3, 75-77	79.76	9.94	53.50	35.45	1.11
4H-1, 123-125	29.74	18.31	38.69	39.44	3.56	9H-4, 23-25	80.74	17.59	42.55	31.65	8.21
4H-2, 23-25	30.24	21.95	39.13	38.93	0.00	9H-4, 75-77	81.26	17.61	42.94	35.03	4.42
4H-2, 75-77	30.76	16.53	28.65	54.82	0.00	9H-5, 23-25	82.24	20.38	43.42	27.33	8.88
4H-3, 23-25	31.74	25.84	26.30	41.34	6.52	9H-5, 78-80	82.78	11.60	50.47	37.94	0.00
4H-3, 75-77	32.26	31.59	31.75	36.66	0.00	9H-6, 23-25	83.74	21.38	42.81	29.38	6.43
4H-4, 23-25	33.24	21.56	33.21	37.65	7.58	9H-6, 75-77	84.26	20.44	43.23	32.24	4.09
4H-4, 75-77	33.76	30.88	24.86	44.27	0.00	9H-7, 23-25	85.24	21.68	44.61	29.25	4.46
4H-5, 23-25	34.74	26.38	26.65	42.10	4.86	9H-7, 30-32	85.31	21.42	42.77	29.74	6.07
4H-5, 75-77	35.26	24.85	25.73	49.42	0.00	10H-1, 75-77	86.26	24.93	40.59	25.10	9.37
4H-6, 23-25	36.24	27.49	26.03	37.88	8.60	10H-1, 124-126	86.75	27.32	37.61	21.14	13.93
4H-6, 75-77	36.76	29.00	25.96	45.04	0.00	10H-2, 23-24	87.24	30.08	28.03	30.03	11.86
4H-7, 19-21	37.70	27.62	30.65	41.73	0.00	10H-2, 75-77	87.76	25.37	33.97	32.67	7.99
4H-7, 23-25	37.74	32.01	29.81	38.18	0.00	10H-3, 23-24	88.74	28.30	35.06	29.79	6.85
5H-1, 109-111	39.10	51.63	11.93	36.44	0.00	10H-3, 75-77	89.26	28.04	29.78	35.91	6.28
5H-1, 123-125	39.24	70.47	8.69	19.26	1.59	10H-4, 23-24	90.24	31.85	21.68	31.77	14.70
5H-2, 23-25	39.74	73.57	10.99	13.54	1.90	10H-4, 75-77	90.76	28.16	23.07	37.35	11.41
5H-2, 75-77	40.26	71.46	8.57	19.97	0.00	10H-5, 23-24	91.74	48.08	8.39	11.68	31.85
5H-3, 23-25	41.24	84.69	3.59	8.61	3.11	10H-5, 75-77	92.26	41.73	10.65	39.57	8.06
5H-3, 75-77	41.76	81.15	0.00	18.85	0.00	10H-6, 23-24	93.24	32.92	18.67	41.49	6.91
5H-4, 23-25	42.74	86.38	0.00	5.67	7.95	10H-6, 75-77	93.76	27.64	32.38	39.97	0.00
5H-4, 74-76	43.25	76.04	0.00	23.96	0.00	10H-7, 23-24	94.74	30.63	25.35	41.77	2.25
5H-5, 23-25	44.24	86.17	0.83	3.81	9.19	10H-7, 29-31	94.80	33.08	26.50	37.45	2.97
5H-5, 87-89	44.88	83.23	0.00	14.22	2.55	11H-1, 75-77	95.76	22.37	36.10	39.95	1.58
5H-6, 23-25	45.74	83.86	0.00	9.76	6.37	11H-1, 123-125	96.24	22.44	40.44	30.21	6.90

Table T17 (continued).

Core, section, interval (cm)	Depth (mbsf)	Calcite (model wt%)	Opal (model wt%)	Smectite (model wt%)	Illite (model wt%)	Core, section, interval (cm)	Depth (mbsf)	Calcite (model wt%)	Opal (model wt%)	Smectite (model wt%)	Illite (model wt%)
11H-2, 23-25	96.74	20.76	42.80	32.05	4.39	10H-7, 47-49	130.92	0.00	55.27	44.73	0.00
11H-2, 75-77	97.26	15.93	41.44	42.00	0.64	11H-1, 75-77	131.76	0.72	57.71	41.57	0.00
11H-3, 23-25	98.24	14.76	44.13	36.39	4.72	11H-1, 123-125	132.24	13.01	48.32	37.81	0.86
11H-3, 72-74	98.73	9.75	49.89	40.36	0.00	11H-2, 23-25	132.74	14.14	47.18	38.68	0.00
11H-4, 23-25	99.74	16.65	42.83	36.28	4.24	11H-2, 75-77	133.26	8.61	46.87	44.51	0.00
11H-4, 75-77	100.26	12.62	49.70	35.02	2.66	11H-3, 23-25	134.24	13.30	50.68	34.59	1.43
11H-5, 23-25	101.24	12.30	51.17	32.46	4.07	11H-3, 75-77	134.76	9.51	43.85	46.65	0.00
11H-5, 75-77	101.76	12.61	52.30	35.10	0.00	11H-4, 23-25	135.74	16.57	41.89	41.55	0.00
11H-6, 23-25	102.74	8.49	53.63	34.84	3.04	11H-4, 75-77	136.26	4.96	49.97	45.07	0.00
11H-6, 75-77	103.26	5.38	54.11	40.52	0.00	11H-5, 23-25	137.24	9.29	43.81	46.90	0.00
11H-7, 23-25	104.24	1.66	62.83	31.31	4.20	11H-5, 75-77	137.76	12.47	31.42	56.12	0.00
11H-7, 50-52	104.51	1.31	62.16	33.19	3.34	11H-6, 23-25	138.74	11.88	45.11	43.01	0.00
12H-1, 75-77	105.26	8.21	53.89	37.44	0.45	11H-6, 75-77	139.26	6.36	50.83	42.82	0.00
12H-1, 124-126	105.75	14.10	57.57	21.72	6.61	11H-7, 23-25	140.24	2.54	61.74	35.72	0.00
12H-2, 23-25	106.24	14.42	51.46	27.81	6.30	11H-7, 40-42	140.41	0.00	60.47	39.53	0.00
12H-2, 75-77	106.76	19.08	49.95	27.29	3.68	12H-1, 78-80	141.29	8.44	49.51	42.05	0.00
12H-3, 23-25	107.74	16.90	48.32	32.50	2.27	12H-1, 124-126	141.75	9.62	51.27	39.11	0.00
12H-3, 75-77	108.26	16.91	48.90	34.15	0.03	12H-2, 23-25	142.24	9.13	53.87	36.99	0.00
12H-4, 23-25	109.24	9.38	64.24	26.04	0.34	12H-2, 78-80	142.79	8.83	39.27	51.90	0.00
12H-4, 75-77	109.76	7.05	56.88	36.07	0.00	12H-3, 23-25	143.74	4.80	59.28	35.92	0.00
12H-5, 23-25	110.74	7.94	57.19	34.86	0.00	12H-3, 75-77	144.26	4.30	48.85	46.85	0.00
12H-5, 75-77	111.26	11.65	49.14	35.52	3.69	12H-4, 23-25	145.24	17.55	29.01	53.44	0.00
12H-6, 23-25	112.24	13.75	44.59	38.93	2.73	12H-4, 75-77	145.76	5.72	49.20	45.08	0.00
12H-6, 75-77	112.76	8.48	51.98	39.55	0.00	12H-5, 23-25	146.74	10.36	48.19	41.45	0.00
12H-7, 23-25	113.74	12.31	49.21	33.87	4.61	12H-5, 75-77	147.26	8.58	48.82	42.60	0.00
12H-7, 29-30	113.80	11.25	52.91	33.10	2.74	12H-6, 23-25	148.24	12.62	44.01	42.85	0.52
199-1220B-						12H-6, 82-84	148.83	16.99	27.88	55.13	0.00
9H-1, 75-77	112.76	8.87	49.77	41.36	0.00	12H-7, 5-7	149.56	13.18	44.12	41.38	1.32
9H-1, 123-125	113.24	12.13	53.18	33.54	1.15	12H-7, 50-52	150.01	7.09	47.32	45.59	0.00
9H-2, 23-25	113.74	15.50	45.76	34.38	4.36	13H-1, 50-52	150.51	0.00	63.03	36.97	0.00
9H-2, 75-77	114.26	9.93	45.72	44.35	0.00	13H-1, 75-77	150.76	24.10	0.00	75.90	0.00
9H-3, 23-25	115.24	16.66	44.09	34.14	5.11	13H-1, 110-112	151.11	0.00	61.02	38.98	0.00
9H-3, 75-77	115.76	6.97	53.76	39.27	0.00	16X-1, 27-29	169.38	0.00	64.83	35.17	0.00
9H-4, 23-25	116.74	13.95	49.37	31.89	4.79	16X-1, 123-125	170.34	0.00	63.10	36.90	0.00
9H-4, 75-77	117.26	6.68	51.88	41.44	0.00	16X-2, 23-25	170.84	0.00	66.43	33.57	0.00
9H-5, 23-25	118.24	8.32	54.48	36.16	1.03	16X-2, 81-83	171.42	0.00	66.13	33.87	0.00
9H-5, 75-77	118.76	6.55	52.79	40.66	0.00	16X-3, 23-25	172.34	0.00	60.68	39.32	0.00
9H-6, 23-25	119.74	7.32	53.98	38.71	0.00	16X-3, 76-78	172.87	0.00	65.49	34.51	0.00
9H-6, 75-77	120.25	0.02	56.77	43.21	0.00	16X-4, 23-25	173.84	0.00	46.39	53.61	0.00
10H-1, 75-77	122.26	2.88	53.96	43.16	0.00	16X-4, 89-91	174.50	0.00	64.05	35.95	0.00
10H-1, 123-125	122.74	3.82	58.05	38.13	0.00	16X-5, 25-27	175.36	0.00	64.55	35.45	0.00
10H-2, 23-25	123.24	7.22	55.97	36.81	0.00	16X-6, 23-25	176.84	0.00	65.12	34.88	0.00
10H-2, 75-77	123.76	8.44	53.96	37.61	0.00	16X-6, 96-98	177.57	0.00	63.16	36.84	0.00
10H-3, 23-25	124.68	0.00	59.22	40.78	0.00	16X-7, 23-25	178.34	0.00	65.43	34.57	0.00
10H-3, 75-77	125.20	0.79	59.18	40.03	0.00	18X-1, 76-78	188.67	35.75	31.56	32.68	0.00
10H-4, 23-25	126.18	1.87	61.73	36.40	0.00	18X-1, 123-125	189.14	28.39	44.34	27.28	0.00
10H-4, 75-77	126.70	0.00	62.09	37.91	0.00	18X-2, 22-24	189.63	35.07	38.91	26.03	0.00
10H-5, 23-25	127.68	8.56	57.81	33.63	0.00	18X-2, 64-66	190.05	41.34	26.90	31.75	0.00
10H-5, 75-77	128.20	7.27	50.64	42.10	0.00	18X-3, 23-25	190.46	17.15	47.19	35.66	0.00
10H-6, 23-25	129.18	6.73	60.26	33.02	0.00	18X-3, 103-105	191.26	41.58	25.98	32.43	0.00
10H-6, 75-77	129.70	8.33	42.34	49.33	0.00	19X-1, 54-56	192.95	67.64	0.00	32.36	0.00
10H-7, 23-25	130.68	0.55	63.24	36.22	0.00						

Note: This table is also available in [ASCII](#). [N1]

Table T18. Split-core velocity measurements, Holes 1220A and 1220B.

Core, section, interval (cm)	Depth (mbsf)	Velocity (m/s)			Anisotropy (%)	Core, section, interval (cm)	Depth (mbsf)	Velocity (m/s)			Anisotropy (%)
		z*	y*	x†				z*	y*	x†	
199-1220A-						9H-7, 31	85.31			1565	
1H-1, 85	0.85	1485	1506		1.4	10H-1, 76	86.26			1555	
1H-2, 76	2.26	1486	1497		0.8	10H-2, 76	87.76			1568	
1H-3, 76	3.76	1486	1501		1.0	10H-3, 76	89.26			1575	
1H-4, 76	5.26	1486	1502		1.1	10H-4, 76	90.76			1561	
1H-5, 76	6.76	1488	1499		0.8	10H-5, 76	92.26			1559	
1H-6, 76	8.26	1490	1498		0.6	10H-6, 76	93.76			1572	
1H-7, 38	9.38	1488	1508		1.3	10H-7, 30	94.80			1572	
2H-1, 45	9.95	1490	1502		0.8	11H-1, 75	95.75			1578	
2H-2, 76	11.76	1488				11H-2, 76	97.26			1557	
2H-3, 76	13.26	1491	1515		1.6	11H-3, 73	98.73			1561	
2H-4, 76	14.76	1491				11H-4, 76	100.26			1589	
2H-5, 76	16.26	1490				11H-5, 76	101.76			1583	
2H-4, 76	14.76			1533		11H-6, 76	103.26			1582	
2H-5, 76	16.26			1535		11H-7, 51	104.51			1577	
2H-6, 76	17.76			1545		12H-1, 76	105.26			1564	
2H-7, 36	18.86			1521		12H-2, 76	106.76			1562	
3H-1, 80	19.80			1548		12H-3, 76	108.26			1560	
3H-2, 76	21.21			1562		12H-4, 76	109.76			1559	
3H-3, 79	22.74			1561		12H-5, 76	111.26			1553	
3H-4, 70	24.15			1519		12H-6, 76	112.76			1563	
3H-5, 76	25.21			1532		12H-7, 30	113.80			1578	
3H-6, 76	26.71			1534		199-1220B-					
3H-7, 76	28.21			1556		9H-1, 76	112.76			1572	
4H-1, 70	29.20			1572		9H-2, 76	114.26			1552	
4H-2, 76	30.76			1545		9H-3, 76	115.76			1562	
4H-3, 76	32.26			1545		9H-4, 76	117.26			1574	
4H-4, 76	33.76			1544		9H-5, 76	118.76			1565	
4H-5, 76	35.26			1539		9H-6, 76	120.26			1565	
4H-6, 76	36.76			1535		10H-1, 76	122.26			1566	
4H-7, 20	37.70			1537		10H-2, 76	123.76			1551	
5H-1, 110	39.10			1535		10H-3, 76	125.20			1551	
5H-2, 76	40.26			1518		10H-4, 76	126.70			1568	
5H-3, 76	41.76			1518		10H-5, 76	128.20			1570	
5H-4, 75	43.25			1525		10H-6, 76	129.70			1568	
5H-5, 88	44.88			1509		10H-7, 48	130.92			1570	
5H-6, 76	46.26			1535		11H-1, 76	131.76			1563	
5H-7, 37	47.37			1549		11H-2, 76	133.26			1558	
6H-1, 76	48.26			1532		11H-3, 76	134.76			1565	
6H-2, 76	49.76			1534		11H-4, 76	136.26			1563	
6H-3, 76	51.26			1520		11H-5, 76	137.76			1569	
6H-4, 76	52.76			1527		11H-6, 76	139.26			1571	
6H-5, 76	54.26			1509		11H-7, 41	140.41			1557	
6H-6, 76	55.76			1515		12H-1, 79	141.29			1574	
6H-7, 29	56.79			1514		12H-2, 79	142.79			1569	
7H-1, 76	57.76			1522		12H-3, 76	144.26			1569	
7H-2, 76	59.26			1515		12H-4, 76	145.76			1566	
7H-3, 76	60.72			1525		12H-5, 76	147.26			1566	
7H-4, 76	62.22			1517		12H-6, 83	148.83			1548	
7H-5, 76	63.72			1530		12H-7, 51	150.01			1567	
7H-6, 76	65.22			1528		13H-1, 51	150.51			1565	
7H-7, 26	66.22			1531		13H-1, 76	150.76			1538	
8H-1, 72	67.22			1552		15X-CC, 1	159.51	3019		3179	5.2
8H-2, 46	68.46			1530		16X-1, 28	169.38			1562	
8H-3, 72	70.22			1558		16X-3, 77	172.87			1542	
8H-4, 72	71.72			1565		16X-6, 97	177.57			1559	
8H-5, 72	73.22			1573		17X-CC, 5	178.35	3236		3186	-1.6
8H-6, 72	74.72			1562		18X-1, 77	188.67			1544	
8H-7, 31	75.81			1560		18X-2, 65	190.05			1542	
9H-1, 56	76.56			1566		18X-3, 104	191.26			1534	
9H-2, 86	78.36			1562		19X-1, 1	192.41			4893	
9H-3, 76	79.76			1560		19X-1, 55	192.95			1570	
9H-4, 76	81.26			1569							
9H-5, 79	82.79			1570							
9H-6, 76	84.26			1568							

Notes: \* = determined by insertion probe, † = determined by contact probe. This table is also available in [ASCII](#).

**Table T19.** Thermal conductivity, Holes 1220A and 1220B.

Core, section, interval (cm)	Depth (mbsf)	Thermal conductivity (W/[m·K])
199-1220A-		
1H-3, 76	3.76	0.74
2H-3, 76	13.26	0.76
3H-3, 76	22.71	0.95
4H-3, 76	32.26	0.74
5H-3, 76	41.76	0.95
6H-3, 76	51.26	0.97
7H-3, 76	60.72	1.01
8H-3, 76	70.26	0.71
9H-3, 76	79.76	0.72
10H-3, 76	89.26	0.72
11H-3, 78	98.78	0.74
12H-3, 76	108.26	0.75
199-1220B-		
1H-3, 76	37.76	0.75
2H-3, 76	47.26	1.01
3H-3, 76	56.76	1.14
4H-3, 76	68.26	0.87
5H-3, 76	77.76	0.71
6H-3, 100	87.33	0.72
7H-3, 60	96.60	0.77
8H-3, 76	106.26	0.78
9H-3, 76	115.76	0.72
10H-3, 76	125.20	0.71
11H-3, 76	134.76	0.74
12H-3, 76	144.26	0.71
16X-3, 76	172.86	0.86
18X-3, 76	190.98	0.94

Note: This table is also available in [ASCII](#).

**Table T20.** In situ temperature, Hole 1220B.

Hole, core	Depth (mbsf)	In situ temperature* (°C)
199-1220B-		
	0.00	1.45
2H	49.50	4.50
5H	83.50	5.95
7H	102.50	7.15

Notes: \* = seafloor temperature is the average of the determinations accompanying the three cores. This table is also available in [ASCII](#).

## **CHAPTER NOTE**

- N1.** 13 December 2002—After the CD-ROM version of this volume was published, errors were noted in the ASCII versions of Tables T2, T5, T7, T11, T14, and T17. This version contains the corrected ASCII files.